

MÖSSBAUER STUDIES OF LOCAL ENVIRONMENTS IN PYRITES,
MARCASITES AND RELATED COMPOUNDS

by

PETER S. WHITE B.Sc.

Submitted in partial fulfilment of the
requirements for the Degree of Doctor
of Philosophy at Dalhousie University,

October 1972.

Approved by the supervising committee:



Peter S. White 1974

TABLE OF CONTENTS

List of Tables	iii
List of Figures	iv
Abstract	vi
List of Symbols	viii
Acknowledgements	ix
Chapter 1 Introduction	1
Chapter 2 Experimental	5
1. Preparation of Samples	5
2. X-ray Diffraction	9
3. Mössbauer Spectroscopy	11
Chapter 3 Mössbauer Theory	15
1. Introduction	15
2. Isomer Shift	16
3. Magnetic and Quadrupole Effects	17
4. Quadrupole Splitting With no Magnetic Field	18
5. Antimony Quadrupole Spectra	21
6. Quadrupole Splitting in the Presence of a Magnetic Field	25
7. Sources of Isomer Shifts and Electric Field Gradients	27
Chapter 4 Structure and Bonding in Compounds Investigated	31
1. Pyrites	31

	2. Marcasites	34
	3. Bonding Theories	38
Chapter 5	Metal Environments	43
	1. Introduction	43
	2. Experimental and Results	44
	3. Discussion	50
	4. Transferred Hyperfine Field at ^{57}Fe in $\text{Co}_{0.98}\text{Fe}_{0.02}\text{S}_2$	58
	5. Simulation of Spectra	61
Chapter 6	Non-metal Environments	67
	1. Introduction	67
	2. Interpretation of ^{121}Sb Spectra	68
	3. Experimental and Results	72
	4. Discussion	78
Chapter 7	Conclusions	86
Chapter 8	Computation of the Number of Distinct Isomers Obtainable by Monodentate Substitution of Polyhedra	91
	1. Introduction	91
	2. Polyhedra	92
	3. Formulation of the Problem	101
	4. Computational Considerations	105
	5. Computational Method	107
	6. Uses of the Tables	111
References		114
Appendix	Structure of the Sulpho-antimonides MSbS	119

LIST OF TABLES

2.1	Sources and purities of materials used in sample preparation	6
3.1	Transition intensities for iron-57 and tin-119 Mössbauer spectra	21
3.2	Approximate expressions for antimony-121 energy levels	22
3.3	Energies of the ^{121}Sb Mössbauer absorptions relative to the isomer shift assuming $\eta = 0$	23
5.1	Mössbauer ^{57}Fe parameters for some pyrites, marcasites and arsenopyrites at room temperature	45
5.2	Structural and physical properties of some pyrites, marcasites and arsenopyrites	46
5.3	Results of ^{57}Fe Mössbauer experiments	48
6.1	^{121}Sb Mössbauer results (source and absorber at 77°K)	75
6.2	^{121}Sb Mössbauer results of Donaldson <i>et al.</i> (69)	76
6.3	Mössbauer results for the series $\text{PtSb}_{2-x}\text{Sn}_x$	77
8.1	List of polyhedra	93
8.2	Expansions of the generating functions for a trigonal bipyramid	112

LIST OF FIGURES

3.1	Energy level diagram for a quadrupole split ^{57}Fe or ^{119}Sn Mössbauer spectrum	20
3.2	Energy level diagram for a quadrupole split ^{121}Sb Mössbauer spectrum	24
4.1	The structure of pyrite	32
4.2	The structure of ullmanite (NiSbS)	33
4.3	The structure of marcasite	35
4.4	The arsenopyrite (CoSb_2) structure	37
4.5	Effect of site symmetry on metal d -orbital energies	39
4.6	Proposed bonding scheme for MX_2 compounds	41
5.1	Mössbauer spectra of ^{57}Fe doped NiS_2	49
5.2	Plot of ^{57}Fe isomer shift against metal - non-metal bond length	52
5.3	Plot of ^{57}Fe isomer shift against X-X bond length for some disulphides and diselenides	54
5.4	Plot of ^{57}Fe quadrupole splitting against j	57
5.5	Mössbauer spectra of ^{57}Fe doped CoS_2	59
5.6	Relative orientations of the four body diagonals of a cube and an arbitrary collinear magnetic field	63
5.7	A series of simulated spectra for $\text{Co}_{0.98}\text{Fe}_{0.02}\text{S}_2$	65
6.1	Correlation between ^{121}Sb isomer shift and electronic configuration	69
6.2	^{121}Sb Mössbauer spectra of FeSb_2	73

6.3 Diagrammatic representation of the isomer shift results
for the diantimonides

80

6.4 Plot of e^2Qq against ^{121}Sb site distortion for some
diantimonides

83

8.1 The relationship of the symmetry elements of the point
group D_{3h} to a trigonal bipyramid

103

ABSTRACT

Mössbauer spectroscopy has been used to investigate the local environments of both the metals and non-metals in a number of compounds having the pyrite, marcasite or arsenopyrite structures.

The metal environment was investigated in a number of sulphides, selenides and tellurides most of which had the pyrite structure. The Mössbauer effect in ^{57}Fe was used and the range of compounds available for examination was extended by doping the metal site with ^{57}Fe , thus allowing compounds not containing iron to be observed. A correlation was found between isomer shift and metal - non-metal distance indicating that this is basically a size effect, the quadrupole splittings were found to be primarily dependant on the occupancy of the non-bonding metal t_{2g} orbitals.

One of the compounds investigated was $\text{Co}_{0.98}\text{Fe}_{0.02}\text{S}_2$, for which an abnormal low-temperature spectrum was observed. This spectrum was found to result from magnetic ordering and has been analysed in terms of a helical arrangement of the moments on the metal atoms.

The non-metal environment was investigated using ^{121}Sb Mössbauer spectroscopy. The compounds examined were diantimonides amongst which all three structures are found. The results were found to be in agreement with present bonding theories. A distinct difference in isomer shifts was observed between metals and semiconductors, resulting from the s character of the conduction band. The quadrupole effects were found to be

geometric in origin and corresponded to a localised non-metal - non-metal bond and a delocalised non-metal - metal bonding band.

The results for the non-metal sites were supported by an investigation of a number of ternary sulpho-antimonides MSbS and a series of compounds $\text{PtSb}_{2-x}\text{Sn}_x$. In the latter series the Mössbauer effect in ^{119}Sn was also observed allowing a comparison with the antimony results. The exact structure of the sulpho-antimonides is not known with any degree of certainty, it was, however, possible to interpret the quadrupole results for these compounds in terms of Sb-S pairs which are consistent with the most probable structure.

A series of computations have been performed to produce a set of tables from which can be determined the number of distinct isomers that can be derived by monodentate substitution of convex polyhedra. These tables should prove to be very useful in the analysis of Mössbauer spectra of random structures. They also have a potential use in any problem that requires an enumeration of possible isomers for other than the simplest of polyhedra.

LIST OF SYMBOLS

*In addition to the standard mathematical symbols, the following additional symbols have been used.

E	The number of edges on a polyhedron
F	The number of faces on a polyhedron
h, k, l	Miller indices
I	Nuclear principal quantum number
J	The number of electrons per formula unit in excess of the formal bonding requirements.
M	Metal
M_I	Nuclear magnetic quantum number
m_h	Horizontal mirror plane
m_v	Vertical mirror plane
P.G.	Point group
Q	Nuclear quadrupole moment
r	Rotation axis
s	Inversion axis
V	Number of vertices on a polyhedron
X	Non-metal
H	Hamiltonian
$\psi^2(0)$	Electron density at the nucleus

ACKNOWLEDGEMENTS

I would like to thank Professor Osvald Knop for his guidance throughout the course of this research and for the insight he has given me into the ways of structural chemistry.

I would also like to thank Dr. F. W. D. Woodhams for his help in the collection and analysis of the Mössbauer spectra, and the members of the Department of Natural Philosophy at the University of Aberdeen for making my stay there so profitable.

I am very grateful for the assistance I have had from my fellow graduate students, especially Drs. C. Ayasse and C-H. Huang, and from the other members of the Dalhousie Chemistry Department. In particular I should like to thank Dr. J. B. Faught for his help with some of the x-ray work.

Dalhousie University and the National Research Council of Canada have provided financial assistance for this research in the form of Graduate Scholarships which I gratefully acknowledge.

I would like to thank Miss Roberta Fullerton for her help in the preparation of this thesis and for her continued encouragement. A special thanks are also due to my parents for their support in this work.

Chapter 1.

INTRODUCTION

This thesis is primarily concerned with the investigation of local environments in a series of closely related compounds. The compounds investigated fall into three structural types: pyrites, marcasites and distorted marcasites of the $CoSb_2$ type. These structures are related in that they all require octahedral coordination of the cations, tetrahedral coordination of the anions and anion - anion pairs. Thus while the structures vary, the local environments remain similar. This work is a natural continuation of a series of structural studies on similar compounds (1).

The use of diffraction methods for studying structures results in a solution that is in effect an average over a large number of structural units. The result obtained from a structure containing a random distribution of two types of atom would be identical to that from a structure containing one type of atom with a scattering power equal to the mean of the random atoms. In recent years a number of techniques such as NMR, NQR, ESR and Mössbauer spectroscopy have been applied to the study of solids. These techniques are similar in that they give results that are the aggregate of the results from each observed site in the sample. Thus in the example above the random distribution would give rise to a distribution of results, whereas the single type of atom would give rise to a single result. These techniques may therefore be used to obtain information about bonding and local environments that is not available from diffraction

experiments. This work involves the use of Mössbauer spectroscopy to investigate iron and antimony local environments.

The variety of physical properties possessed by compounds with pyrite and marcasite structures is of considerable interest, and has been the subject of several comprehensive reviews, including (2,3). Various authors have proposed bonding schemes for these compounds (4,5,6,7) which account reasonably well for the observed physical properties. Most of these schemes are similar in general approach, however, they vary in detail. The more detailed schemes almost invariably rely on trends in x-ray structural parameters to interpret the bonding. It is notable that in these compounds bond distances, especially those between the non-metals, are extremely sensitive to the structural parameters and tend to have quite large uncertainties associated with them. Thus the trends in distances that bonding schemes often depend upon are frequently uncertain when viewed critically. This uncertainty could be reduced by a careful re-determination of the crystal structures, but for the reduction to be significant an improvement of at least an order of magnitude on present results would be required. An alternative approach would be to use a method of investigation that gives results which are directly related to the bonding details. Such a technique is Mössbauer spectroscopy which gives a measure of electron density at the nucleus and charge asymmetry. Iron compounds of this type have already been well investigated, with some degree of success. However, they are limited in number and the results are also somewhat restrictive in that they concern only the metal sites. To obtain a more complete understanding

of the bonding it would be desirable to investigate the non-metal site as well.

It was proposed to approach the problem in two ways:

- a) A series of compounds with metals other than iron would be doped with ^{57}Fe to increase the range of metal site data. Iron-doped CoS_2 had already been looked at by Gallagher et al. (8), but their spectra were not satisfactorily explained. This composition was included in the investigation and gave rise to some interesting conclusions regarding the magnetic structure of CoS_2 .
- b) As no Mössbauer results from non-metal sites were available, except some ^{125}Te studies of magnetic ordering in MnTe_2 (9), a large selection of antimonides were prepared and ^{121}Sb Mössbauer used to investigate the non-metal site. These antimonides consisted of diantimonides MSb_2 , sulpho-antimonides MSbS and some compounds with tin and antimony in the non-metal site.

The second part of the thesis is concerned with the calculation of coefficients for some combinatorial polynomials. It is now quite clear that an intuitive explanation of complex Mössbauer spectra is not adequate. Such spectra must be analysed in some detail to obtain meaningful results. One of the commonly encountered cases is a Mössbauer atom surrounded by a random arrangement of two or more different types of atom, such as in a disordered alloy. The combinatorial coefficients calculated give the number of possible unique

surroundings for the Mössbauer atom, taking proper account of the⁽¹⁾
symmetries of the pertinent coordination polyhedra, and thus provide
a check that all possible environments have been considered. These
results can also be of use in other areas where an enumeration of
environments is required and can not be readily obtained by inspection.

Chapter 2.

EXPERIMENTAL

1. *Preparation of Samples*

All samples were prepared by direct reaction of the elements under vacuum. The source and purity of the materials used are listed in table 2.1. The metal sponges were freshly reduced with purified hydrogen at about 600°C before use. The chromium shot was etched with acid as was the antimony after crushing into easily handled pieces. In order to reduce handling losses small lumps of sulphur and antimony were used in preference to fine powders. The ^{57}Fe doped Mössbauer samples were prepared using iron powder containing at least 90% ^{57}Fe . This was supplied as metal powder by the Oak Ridge National Laboratory, and was reduced with purified hydrogen before use.

The samples containing 2% ^{57}Fe were prepared using metal sponges which were premixed with the ^{57}Fe in order to achieve maximum dispersion of the ^{57}Fe throughout the sample. This also allowed one large batch of doped metal to be prepared for use in several samples with a consequent increase of weighing accuracy and saving in the amount of ^{57}Fe used. This premixing was achieved by dissolving weighed portions of metal sponge and ^{57}Fe in nitric acid. The resultant solution was evaporated to dryness and the residue strongly heated in air until no more fumes were evolved. The residue was then reduced with purified hydrogen to give a metal powder. The reduction was interrupted periodically and the sample weighed, constant weight being taken as the criterion of complete reduction.

Table 2.1. Sources and purities of materials used in sample preparation.

Element	Supplier	Grade	Analysis
Antimony	JMC ¹	Specpure	Si 1ppm Ca, Cu, Fe, Mg, Ag, Na each < 1ppm
Chromium	Koch Light	5N5	99.9995% Cr
Cobalt	JMC	Specpure	Si 5ppm Fe 2ppm Mg 1ppm Al, Ca, Cu, Ag each < 1ppm
Indium	Indium Corp. of America	-	99.99% In
Iridium	JMC	Sponge	
Iron	JMC	Specpure	Mn 3ppm Si 3ppm Mg 2ppm Si 2ppm Cu and Ag < 1ppm
Nickel	JMC	Specpure	Ag, Si, Fe each 3ppm Mg 2ppm Al, Ca, Cu each < 1ppm
Osmium	JMC	Sponge	
Palladium	JMC	Sponge	
Platinum	JMC	Sponge	

Table 2.1 continued.

Element	Supplier	Grade	Analysis
Rhodium	JMC	Sponge	Al 0.5ppm Na, Zn each 0.2ppm Ba, Ni, each 0.1ppm
Ruthenium	JMC	Sponge	Cu, Ti each 0.05ppm Mg, Mn, Ag each 0.03ppm
Selenium	CCR ²	-	B 0.01ppm Ca, Fe, Si each < 1ppm
Sulphur	JMC	Specpure	Cu 0.4ppm Al 0.3ppm Mg 0.5ppm
Tellurium	CCR	-	
Tin	-	-	

¹ Johnson Matthey Chemicals Ltd.

² Canadian Copper Refiners Ltd.

8

Samples ranging in size from 1 to 10 grams were prepared, depending on the availability of the elements. The components were weighed to a reproducibility of ± 0.2 milligrams and transferred to a quartz ampoule via a length of $\frac{1}{4}$ " diameter quartz tube on the end of which was a quartz taper joint. The ampoule had previously been inspected for leaks and degassed with a relatively cool hydrogen oxygen flame whilst under high vacuum. Great care was taken to minimise any sample loss during transfer. Any dust clinging to the walls of weighing bottles or the entrance tube to the ampoule was dislodged by careful tapping, and in suitable cases using a powerful magnet.

The ampoule was then connected to an all glass vacuum system, evacuated, cautiously at first to prevent any fine powders streaming over, and pumped with a mercury diffusion pump for several hours. Pressures measured with a McLeod gauge whilst using the diffusion pump were typically of the order of 10^{-6} torr. The ampoule was then sealed with a hydrogen-oxygen flame and a looped handle attached to the end of it for ease in handling.

The components were reacted with great care, especially in the case of the sulphides which reacted exothermally and could, if allowed to react too fast, produce a high sulphur vapour pressure causing the ampoule to explode. The usual procedure was to preheat a horizontal furnace to between 600 and 800°C and then slowly to move the ampoule towards the hot zone, thus avoiding any sudden change in temperature. The ampoule was then left in the hot zone for at least 24 hours to ensure as complete a reaction as possible, after which it

was removed from the furnace and allowed to cool to room temperature. The ampoule was opened, the sample ground to about 100 mesh and resealed in a somewhat smaller ampoule. The sample was annealed for about a week, after which the ampoule was again opened and an x-ray photograph taken of the sample. If the x-ray showed incomplete reaction (presence of foreign phases) or inadequate crystallinity (diffuse high angle lines), the annealing process was repeated until a satisfactory photograph was obtained. The annealing temperatures were carefully chosen for each sample with the help of available phase diagrams (10, 11, 12) in an attempt to minimize the number of heat treatments required. Whenever possible a diffractometer chart was taken of the final sample and line shapes checked for any impurity lines close to sample lines, which would not be seen on a photograph.

2. X-ray Diffraction

Powder diffraction photographs were taken of portions of samples ground to pass 325 mesh. The sample was mounted on a thin quartz fibre using a solution of silicon vacuum grease in benzene. The cameras used were of the Straumanis type having a diameter of 114.6 mm. Nickel-filtered copper radiation was used as a matter of course. However, some samples gave high background scattering with copper, necessitating the use of manganese filtered iron radiation. Lattice parameters were obtained using Nelson-Riley extrapolation (13) to $\theta = 90^\circ$ employing lines having $\theta > 60^\circ$. The wavelengths, in \AA , used in this work were:

	$K\alpha_1$	$K\alpha_2$	$K\beta$
Copper	1.54050	1.54434	1.5418
Iron	1.93597	1.93991	1.9373

A Philips PW1050 wide range high and low angle goniometer was used to obtain charts for characterising preparations and for the collection of intensity data. Specimens were mounted in a shallow counterbore, about 0.5 mm deep, in a 1" diameter lucite slug.

Whenever possible specimens were dry-mounted by pressing fine ground (325 mesh) powder into the counterbore with a microscope slide, thus allowing the sample to be recovered. If this method failed a small amount of silicon grease was mixed with the sample. Specimens intended for intensity collection were mounted by mixing 325 mesh powder with a minimum of silicon grease to form a thick paste. This paste was pressed into the counterbore of the slug, making every effort to obtain as smooth a surface as possible. The surface was then sprinkled with fine powdered sample. Two specimens were made from each sample and survey charts were run of both. These charts were checked against each other and against a chart run a day or so later for reproducibility, lack of which could be an indication of preferred orientation.

Intensity data were collected for all accessible reflections, using the diffractometer in a continuous scanning mode. The $K\alpha$ radiation was isolated with a line-focusing lithium fluoride crystal monochromator placed between the sample and the proportional counter. Further filtering of unwanted wavelengths and of spurious counts due to amplifier noise was provided by a single channel pulse height analyser.

Data collection was performed with the diffractometer scanning at a rate of $1/8^\circ$ (2θ) per minute, the angular range scanned for each peak being determined from the survey charts. A scan of $1/2^\circ$ (2θ) was made on either side of each peak from which the background correction for the peak was computed. The consistency of these scans also gave an indication of whether the tail of a peak had been cut off by a too short scanning range. Three complete sets of data were collected for each sample and the results averaged. At low Bragg angles the image of the slit projected onto the sample by the x-rays becomes elongated, and if the wrong slit width is chosen may exceed the sample area causing a systematic reduction in observed intensities in this angular range. This effect was checked for by installing a narrower slit and comparing intensity ratios between the lowest angle line and a line at about 60° (2θ).

3. Mössbauer Spectroscopy

Mössbauer spectra were collected both at Dalhousie and at the University of Aberdeen. The two spectrometers, of similar design, being of the constant acceleration type. The drive systems, which have been described at length (14), were built at the University of Aberdeen, the multichannel analysers and ancillary electronics were of commercial origin. The spectra were output on eight-hole paper tape in a format suitable for reading into a computer via a teletype or a high speed paper tape reader.

Samples were prepared either by pressing the powder into a perspex holder, or by mixing the sample powder with powdered thermoplastic and hot-pressing into a disk. The samples were mounted in a

variety of ways depending upon experimental requirements, however in the case of ^{57}Fe and ^{119}Sn spectra, 1/2" diameter samples were placed at least 3" from the source in order to minimize any solid angle effects. In the case of ^{121}Sb spectra the low source strength necessitated that this distance be drastically reduced to achieve a reasonable counting rate. As a significant solid angle effect was introduced great care had to be taken to maintain a constant geometry, especially when changing sources to calibrate the system. Calibration was effected by taking a spectrum of an iron foil, the six lines being assumed to have positions of ± 5.3285 , ± 3.0835 and ± 0.8385 mm/s. The iron-foil isomer shift was taken as a reference for the iron spectra, while tin and antimony results are quoted relative to barium stannate and indium antimonide respectively.

The three sources required slightly different experimental conditions. The higher energy of the antimony γ -ray required the use of a xenon proportional counter, whereas argon or krypton counters were used for iron and tin. The position of the pulse height analyser window is also of some importance in obtaining the optimum counting conditions. For iron and tin this was set on the Mössbauer γ -ray peak, but for antimony it was set on the escape peak which is somewhat more intense than the γ -ray peak. The tin spectra were taken with a palladium filter between the source and absorber to reduce the intensity of the SnK x-rays which occur close to the γ -ray energy.

The low-temperature iron spectra were taken with the source

at room temperature and the sample mounted in a copper cold finger the other end of which was immersed in liquid nitrogen. The antimony spectra were all taken at 77°K with both the source and absorber cooled. In this case calibration was also performed at low temperature as the coupling between the transducer and the source was affected by cooling. A correction was applied to the calibration as the magnetic field in iron at 77°K is 2.5% higher than at room temperature (15). The temperature for both the iron and the antimony runs was checked by a thermocouple placed in the sample mount.

Programs were written for the ICL 4-50 and the CDC 6400 to create and update libraries of spectra. The paper tapes from the analyser output were used as input for these programs which performed the following functions:

- a) The data was searched for dropped channels.
- b) A constant was added to each channel value; this was required as the analysers only stored six digits, the number of millions being lost.
- c) A plot of the spectrum was produced.
- d) The spectrum was added to the library and an updated table of contents produced.

The above functions were default actions for the programs and could be omitted at will. It was also possible to create a new library, output a copy of a spectrum (normally on cards), and input spectra from a medium other than paper tape. The libraries were stored on the fastest data storage device generally available to programs, magnetic tape on the ICL 4-50 and private disc file on the CDC 6400. As magnetic

tape requires a sequential search the libraries were updated so as to place the most recent spectra at the beginning of the tape, these being the spectra most frequently required for fitting. Isomer shifts, quadrupole splittings and linewidths were extracted from the spectra by fitting to them one or more lorentzians and a parabolic background using the method of least squares to minimise χ^2 . Two programs were available for this purpose (16, 17), both allowed various constraints to be placed on the parameters, the nature of which is discussed in Chapter 3. The programs were adapted for use on the CDC 6400 and a number of modifications were made to allow the searching of library files for spectra and the production of plots of the fitted spectra.

Chapter 3.

MOSSBAUER THEORY

1. Introduction

The Mössbauer effect since its first discovery in 1958 (18, 19) has been the subject of many introductory texts, including (20, 21). These texts generally give a somewhat simplified description of the shape of simple Mössbauer spectra. This is adequate for most iron and tin work, but antimony spectra and composite magnetic-quadrupole interactions require a more detailed explanation. The energy levels in the nucleus that are observed in a Mössbauer experiment are in general modified by the immediate environment of the nucleus. Any change in the charge density at the nucleus will change the energy of the nuclear states and this will be seen as a change in the position of the Mössbauer absorption relative to some standard; this change is called the isomer shift (IS). Each nuclear state is in fact a number of degenerate states represented by the magnetic quantum numbers M_I . If a magnetic field, an electric field gradient (EFG) or some combination of these two is applied to the nucleus, then this degeneracy will be totally or partially lifted, resulting in the splitting of the Mössbauer absorption into several related absorptions. The isomer shift is independent of these effects and may be treated separately, while an EFG and a magnetic field will interact and must be considered together. The purpose of this chapter is to explain the parameters that are pertinent in this work, and to show the reasoning behind the constraints used in the fitting of these parameters to experimental spectra.

2. Isomer Shift

The energy of a Mössbauer transition ΔE is the difference between the excited (e) and ground (g) states of the Mössbauer nucleus. However, the nature of the experiment is to restrict the measurement to the difference between the ΔE of the observed nucleus and that of some standard nucleus. Thus for a non-zero isomer shift to be observed the ground and excited states must be perturbed by different amounts. This occurs in the case of a finite electron charge density at the nucleus, because the radius R of the nucleus changes upon excitation. The change in ΔE due to the electron charge density is given by (20):

$$\delta(\Delta E) = f(Z)[(R_e - R_g)/R]|\psi(0)|^2 \quad 3.1$$

where $f(Z)$ is constant for a given nucleus. If the change in nuclear radius is referred to as δR then the isomer shift is given by:

$$IS = f(Z)(\delta R/R)[|\psi(0)|_A^2 - |\psi(0)|_E^2] \quad 3.2$$

The subscripts A and E stand for absorber and source respectively, however it is general practice to refer isomer shifts to some standard compound, not usually the source, which allows a more accurate comparison of results from different laboratories. In this case $|\psi(0)|_E^2$ would be replaced by that of the standard compound. It can be seen from the expression 3.2 that if the term $f(Z)\delta R/R$ is known isomer shifts of different Mössbauer nuclides can be compared. By using suitable isoelectronic compounds several authors (22, 23, 24) have derived the relationship between tin and antimony spectra, thus allowing comparisons, and enabling antimony-121 results to be interpreted in the light of the better understood effect in tin-119. This will be discussed further in the chapter on antimonides.

3. Magnetic and Quadrupole Effects.

The magnetic and quadrupole effects on the nuclear energy states are best described by examining the experimental Hamiltonian operator (25)

$$H = -g_N \beta_N H \cdot I + [e^2 Qq / (4I(2I - 1))] [\{3M_I^2 - I(I + 1)\} + (\eta/2)\{I_+^2 + I_-^2\}] \quad 3.3$$

H is the magnetic field and eq the electric field gradient at the Mössbauer nucleus, η is determined by the asymmetry of the electric field gradient tensor. There are $2I+1$ nuclear states, represented as $|M_I\rangle$, where $M_I = I, I-1, \dots, -I$, for each nuclear spin state I . The effect of H and eq on each state I has to be determined from the Hamiltonian, and energy level diagram can then be constructed showing the allowed Mössbauer transitions. Several features are obvious from the Hamiltonian, the quadrupole splitting is dependent upon M_I^2 and so will only partially lift the degeneracy of the magnetic states leaving $M_I = -M_I$. Also quadrupole splitting will only occur if $I > 1/2$, and thus will only be observed if the ground state, the excited state, or both fulfill this requirement. The exact solution for the energies of the required nuclear states is only possible for the simplest of cases and numerical methods frequently have to be used. The cases of interest in this work are those of quadrupole splitting with no magnetic field for iron-57 and tin-119 ($I_e = 3/2$, $I_g = 1/2$), the similar case for antimony-121 ($I_e = 7/2$, $I_g = 5/2$), and the more complicated case of iron-57 with quadrupole splitting and a small magnetic field. These cases will be dealt with in turn.

4. Quadrupole Splitting with no Magnetic Field

The electric field gradient (EFG) at the Mössbauer nucleus is defined by a tensor having nine components, V_{ij} , in Cartesian coordinates where

$$V_{ij} = \partial^2 V / \partial q_i \partial q_j \quad (q_i, q_j = x, y, z) \quad 3.4$$

and V is the electrostatic potential at the nucleus due to external charges. As the electric field gradient is due to external charges the Laplace equation requires that

$$V_{xx} + V_{yy} + V_{zz} = 0 \quad 3.5$$

and as $V_{ij} = V_{ji}$ the electric field gradient is a symmetric, traceless tensor. It is conventional to transform the tensor to a set of principal axes X, Y, Z ordered such that

$$|V_{xx}| < |V_{yy}| < |V_{zz}|. \quad 3.6$$

As a consequence of 3.5 there are only two independent components which are usually expressed as the 'field gradient' eq and the asymmetry parameter η , where

$$eq = V_{zz}, \quad \eta = (V_{xx} - V_{yy})/V_{zz}. \quad 3.7$$

Iron and tin spectra are determined by the solutions to the equation

$$e^2 Qq / \{4I(2I-1)\} [\{3M_I^2 - I(I+1)\} + (\eta/2)\{I_+^2 + I_-^2\}] |M_I\rangle = E |M_I\rangle \quad 3.8$$

for $I = 3/2$ and $I = 1/2$, E being the energy of the state due to the quadrupole interaction. For $I = 1/2$ no quadrupole interaction is possible and a single energy level results. As the operators I_+ and I_- are defined such that

$$I_{\pm} |M_I\rangle = \{I(I+1) - M_I(M_I \pm 1)\}^{1/2} |M_I \pm 1\rangle \quad 3.9$$

the equations for the excited $I = 3/2$ state become

$$\begin{aligned} H|+3/2\rangle &= (e^2 Qq/4)|+3/2\rangle + (\sqrt{3}/12)ne^2 Qq|\bar{1}/2\rangle \\ H|+1/2\rangle &= (-e^2 Qq/4)|+1/2\rangle + (\sqrt{3}/12)ne^2 Qq|\bar{3}/2\rangle \end{aligned} \quad 3.10$$

As there is an intermixing of states in 3.10 the energy levels are arrived at by solving the secular equation

$$E^2 - (e^2 Qq/4)^2(1+n^2/3) = 0 \quad 3.11$$

which gives

$$E = \pm(e^2 Qq/4)[1+n^2/3]^{1/2} \quad 3.12$$

This leads to the energy level diagram shown in figure 3.1.

It is also necessary to know the relative intensities of the transitions before a quadrupole split spectrum can be analysed. It has been shown (25) that if the ground and excited states can be characterised by I' , M' and I'' , M'' respectively then the relative intensities of the $M' \rightarrow M''$ transitions are given by

$$|\langle I'T M'm | I'T' I''M'' \rangle|^2 F_T^m(\theta). \quad 3.13$$

Here T is the angular momentum of the radiation (equal to 1 in the case of dipole radiation), $m = M'' - M'$, and the squared quantity is the appropriate Clebsch-Gordan or Wigner coefficient. $F_T^m(\theta)$ is the radiation pattern as the intensity is angularly dependent, θ being the angle between the principal axis of the electric field gradient and the direction of observation. For $T = 1$,

$$F_1^m = 1 + 1/4(3m^2 - 2)(3\cos^2\theta - 1). \quad 3.14$$

As the mean value of $\cos^2\theta$ is $1/3$, $F_1^m(\theta)$ averages to 1 in the case of a powder sample and the relative intensities are given by the squares of the Clebsch-Gordan coefficients, which are listed for iron and tin in table 3.1.

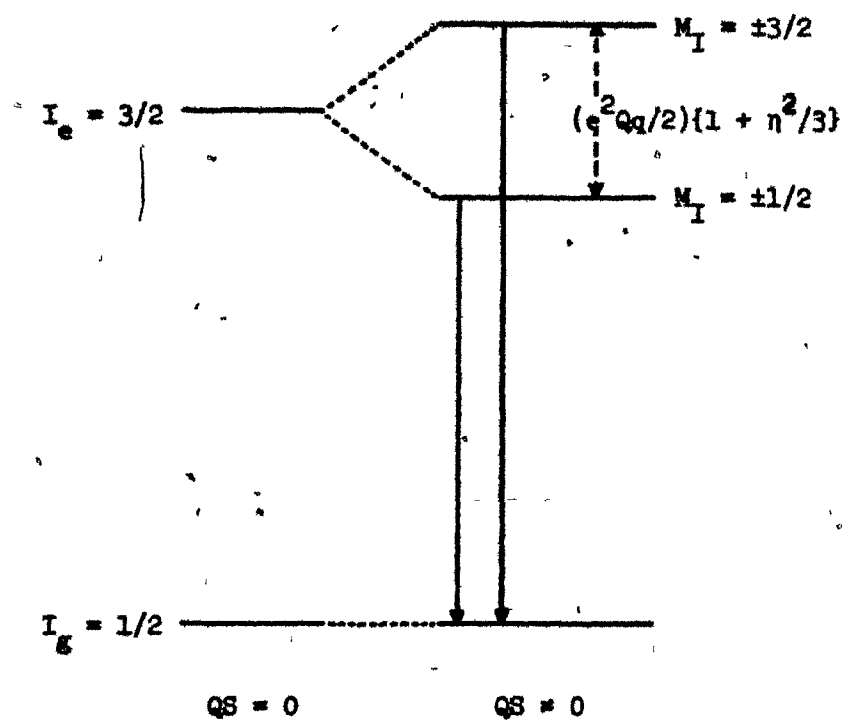


Figure 3.1. Energy level diagram for a quadrupole split ^{57}Fe or ^{119}Sn Mössbauer spectrum.

Table 3.1 Transition Intensities for Iron-57 and Tin-119
Mössbauer Spectra.

Ground State M'	Excited State M''	Relative Intensity
$\pm 1/2$	$\pm 3/2$	1
$\pm 1/2$	$\pm 1/2$	2/3
$\pm 1/2$	$\mp 1/2$	1/3

The transition $|\pm 1/2\rangle_g \rightarrow |\mp 3/2\rangle_e$ is forbidden as the selection rule for dipole radiation is $M_I = 0, \pm 1$. Thus in the case of iron or tin the expected spectrum from a powder sample with a non-zero electric field gradient at the Mössbauer nucleus is two lines with splitting $(e^2Qq/2)(1 + \eta^2/3)^{1/2}$; the two lines having equal intensity. This spectrum will not allow either the sign of the electric field gradient or the relative contribution of η to be determined; this requires an oriented single crystal or the application of a magnetic field.

5. Antimony Quadrupole Spectra

The ^{121}Sb Mössbauer transition is $I_g = 5/2 \rightarrow I_e = 7/2$, and so both ground and excited states will interact with an electric field gradient, the ground state to give three energy levels and the excited state four. The presence of η in equation 3.8 again causes an inter-mixing of states, 3.15 and 3.16 being the secular equations for $I = 5/2$ and $I = 7/2$ respectively:

$$E^3 - 14A(3 - \eta^2)E^2 - 160A^3(1 - \eta^2) = 0, \quad 3.15$$

Table 3.2. Approximate expressions for antimony-121 energy levels.

I	M_I	Energy
5/2	$\pm 1/2$	$-(e^2 Qq/5)\{1 + (4/9)\eta^2 - (172/729)\eta^4 + (15332/59049)\eta^6 - (1717580/4782969)\eta^8\}$
	$\pm 3/2$	$-(e^2 Qq/20)\{1 - (3/2)\eta^2 + (23/24)\eta^4 - (449/432)\eta^6 + (44675/31104)\eta^8\}$
	$\pm 5/2$	$(e^2 Qq/4)\{1 + (1/18)\eta^2 + (17/5832)\eta^4 - (143/944784)\eta^6 - (12587/612220032)\eta^8\}$
7/2	$\pm 1/2$	$-(5e^2 Qq/28)\{1 + (5/6)\eta^2 - (311/216)\eta^4 + (20557/3888)\eta^6 - (762019/31104)\eta^8\}$
	$\pm 3/2$	$-(3e^2 Qq/28)\{1 - (31/30)\eta^2 + (21.967/9)\eta^4 - (397.5973/45)\eta^6 - (734.97/18)\eta^8\}$
	$\pm 5/2$	$(e^2 Qq/28)\{1 + (5/6)\eta^2 + (25/216)\eta^4 - (275/3888)\eta^6 - (25/93312)\eta^8\}$
	$\pm 7/2$	$(7e^2 Qq/28)\{1 + (1/30)\eta^2 + (29/27000)\eta^4 + (1.241/12150)\eta^6 + (2.263/1458000)\eta^8\}$

Table 3.3. Energies of the ^{121}Sb Mössbauer absorptions relative to the isomer shift assuming $\eta = 0$.

No.	Transition	Energy ¹	Relative Intensity
1	$7/2 \rightarrow 5/2$	$(e^2 Qq/4)\{R - 1\}$	21
2	$5/2 \rightarrow 5/2$	$(e^2 Qq/28)\{R - 7\}$	6
3	$5/2 \rightarrow 3/2$	$(e^2 Qq/28)\{R + 7/5\}$	15
4	$3/2 \rightarrow 5/2$	$-(e^2 Qq/28)\{3R + 7\}$	1
5	$3/2 \rightarrow 3/2$	$(e^2 Qq/28)\{(7/5) - 3R\}$	10
6	$3/2 \rightarrow 1/2$	$(e^2 Qq/28)\{(28/5) - 3R\}$	10
7	$1/2 \rightarrow 3/2$	$(e^2 Qq/28)\{(7/5) - 5R\}$	3
8	$1/2 \rightarrow 1/2$	$(e^2 Qq/28)\{(28/5) - 5R\}$	18

¹ Q refers to the ground state nuclear quadrupole moment, R is the ratio of the excited state moment to that of the ground state and has a value of 1.34 ± 0.02 .

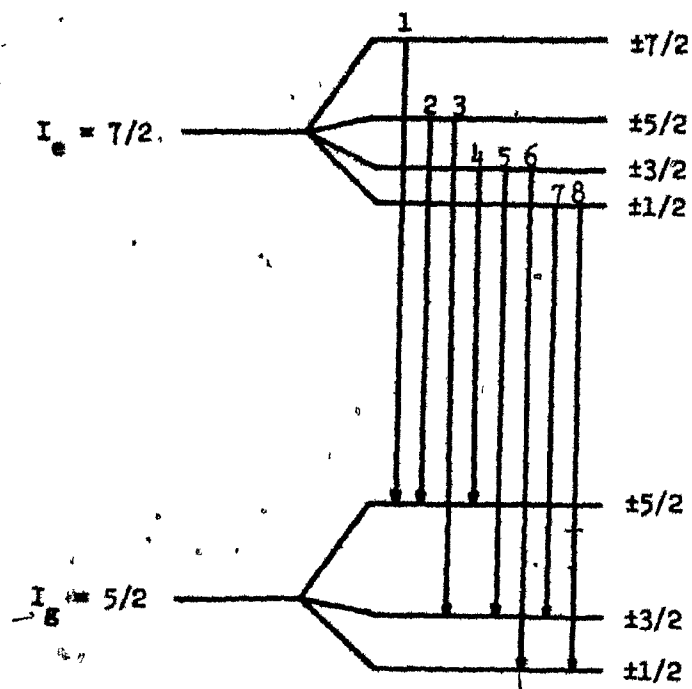


Figure 3.2. Energy level diagram for a quadrupole split

^{121}Sb Mössbauer spectrum.

$$E^4 - 378A^2(1 + \eta^2/3)E^2 - 1728A^3(1 - \eta^2)E + 8505A^4(1 + \eta^2/3)^2 = 0, \quad 3.16$$

where $A = e^2Qq/4I(2I-1)$. These equations can not be solved exactly and numerical methods have to be employed. Such calculations have been performed (26, 27), resulting in the expansion of E_{M_I} in terms of a power series in η . These series are presented in table 3.2, and from these results the energy level diagram, figure 3.2, can be drawn up. As can be seen from the expansions the asymmetry of the electric field gradient enters the energies as at most a second-order term, and it has been shown (28) that if η is less than 0.5 the effect on a spectrum is of very little significance. Thus it is reasonable in most cases to assume that $\eta = 0$, the relative energies and intensities for this assumption being given in table 3.3. The constant R arises because the nuclear quadrupole moment changes with nuclear state, R being defined as Q_e/Q_g .

The details derived above show that antimony spectra as opposed to iron and tin will give values for the sign of the electric field gradient and η from a powder sample. However, the experimental spectrum is very insensitive to η and little significance can be placed on the values obtained. The complex form of the spectrum can lead to some confusion as to what is meant by quadrupole splitting (a term with obvious meaning in the case of iron and tin). In this work quadrupole effects will be referred to in terms of e^2Qq .

6. Quadrupole Splitting in the Presence of a Magnetic Field

In the case of mixed magnetic-quadrupole interactions the Hamiltonian is made up of the sum of the individual components

$$H = H_{\text{mag}} + H_{\text{quad}} \quad 3.17$$

giving the operator 3.3 referred to earlier. It is usual to set up the magnetic part of the operator with respect to the γ -ray direction and the quadrupole part to the principal axis of the electric field gradient. Before any computations are performed a transformation has to be made so that both parts are referred to the same set of axis, in this case those of the electric field gradient. The solutions of the equations

$$H|M_I\rangle = E|M_I\rangle \quad 3.18$$

for the ground and excited states will give the splittings of these states from which the relative positions of the component lines of the spectrum can be calculated. The relative intensities are arrived at using 3.13. If this scheme were followed the resultant spectrum would be that expected from a single-crystal sample with either an internal or external magnetic field. If a powder sample is used the method must be expanded to allow for the random orientation of the sample. This is achieved by summing spectra obtained from all orientations of the crystal coordinate system with respect to the experimental coordinates. If the magnetic field is an internal one it must maintain a fixed orientation with respect to the crystal coordinates throughout the summation, whereas an external field must maintain a fixed orientation with respect to the experimental coordinates. The case of an internal field is a less time consuming computation as the summation can be performed analytically; an external field requires each component spectrum to be simulated and a numerical summation to be performed.

Solutions to the above problem have to be obtained using numerical methods. In this work a program package PL43B written by

Gabriel and Ruby (29, 30, 31) was used to perform the calculations. The codes were converted from the original CDC 3600 FORTRAN to a form suitable for the input to the RUN compiler on the CDC 6400 at Dalhousie. A plotting routine was also written so that output from the program could be directly compared to the experimental spectra.

7. Sources of Isomer Shifts and Electric Field Gradients

The foregoing sections have described the effect on Mössbauer spectra of various interactions arising from the particular local environment of an atom. The source of a magnetic field in a magnetically ordered compound is reasonably straightforward, but the electric charge density at a nucleus and electric field gradients require careful consideration when analysing spectra. As there is nearly always a large uncertainty in some of the fundamental constants required to calculate quantities such as isomer shifts and quadrupole splittings, it is rarely possible to obtain much information from a single spectrum. If, however, a series of compounds can be looked at, the variations in the Mössbauer parameters often give far more information than their absolute values. The purpose of this section is to show how variations in structure and bonding can be expected to affect Mössbauer parameters.

Both the isomer shift and the quadrupole splitting are products of a function of the electronic environment of a nucleus and a nuclear parameter. As the nuclear parameters are constant for a given nuclide, Mössbauer results for that nuclide can be compared in terms of the electronic environment without a detailed knowledge of them. It is however desirable at least to know the signs of these parameters, as these have a direct bearing on the interpretation of variations in

experimental results.

The isomer shift is directly proportional to the electron charge density at the Mössbauer nucleus. It is thus determined by the electronic configuration of the Mössbauer atom, and to a good approximation by the valence shell of that atom, as the inner shells can be considered as an unchanging core. Of the hydrogen-like wave-functions only the s-orbital has a finite electron charge density at the nucleus (though if relativistic effects are taken into consideration the other orbital types make a small contribution), so as a first approximation the isomer shift is a measure of the occupancy of the s valence orbital. This is seen in the much used grouping of isomer shifts into ranges which can be attributed to specific valence states. The effect of the other orbitals, especially p-orbitals, is predominantly one of shielding. Thus if the main difference between two compounds is p-orbital occupancy then the compound with the most p electrons will have the lower electron charge density at the nucleus. Whilst it would be desirable to relate isomer shifts to molecular-orbital calculations this is seldom possible; calculations have been performed (22, 23) using the self-consistent field methods to obtain the electron charge density at the nucleus for free atoms in various valence states. These calculations can then be used if the bonding in certain reference compounds is assumed to make a direct relationship between isomer shift and valence state.

An electric field gradient will in general occur at a nucleus if the charge distribution seen by that nucleus has a symmetry that is lower than cubic. Whilst the field gradient seen by the nucleus is due

to an asymmetrical distribution of the charge density within the atom, this has two possible causes: (a) an asymmetrical charge distribution in the bonding orbitals, and (b) in an ionic crystal, an asymmetric distribution of the surrounding ions. In case (b) the gradient produced is magnified by a factor $(1 - \gamma_{\infty})$, where γ_{∞} is the Sternheimer antishielding constant (25), and in fact the predominant contribution is from the distortion induced in the electrons of the Mössbauer atom. Thus the electric field gradient q can be expressed as the sum

$$q = q_{\text{val}} + q_{\text{lat}}; \quad 3.19$$

in most cases one of these terms predominates and the other can be neglected. In the case of ionic compounds reasonable calculated results can be obtained by the use of a point charge model. This model quite often gives the correct trend for a series of compounds even when they are known to be far from ionic. This can be explained in terms of the dominant variation within the series being a geometric one, which is reflected in the ion positions in the point charge calculations. In the non-ionic case the valence contribution becomes predominant and as wavefunctions are not well known in most cases interpretation becomes more qualitative. It is of interest, however, to examine some of the basic expressions used in calculating electric field gradients. If the nucleus is at a position with C_3 or higher symmetry then the asymmetry parameter will be zero and the axis of the electric field gradient will be the same as the axis of highest symmetry. If the symmetry is close to axial, then although η is no longer zero an approximate direction for the field gradient may be arrived at by assuming higher symmetry. The basic relations for the electric

field gradient assuming the tensor to be diagonalised are

$$V_{zz} = \sum_i q_i (3\cos^2\theta_i - 1)r_i^{-3} \quad 3.20$$

$$\eta = (1/V_{zz}) \sum_i q_i 3\sin^2\theta_i \cos^2\phi_i r_i^{-3} \quad 3.21$$

where r_i , θ_i , and ϕ_i are the spherical coordinates of the charge q_i .

In the case of a bond the quantities of interest are the direction of the bond with respect to the direction of the field gradient which is often known from structural studies, and the value of $\langle r^{-3} \rangle$ for the bond from which information about the bonding may be inferred.

Chapter 4.

STRUCTURE AND BONDING IN COMPOUNDS INVESTIGATED

The compounds investigated in this work are all of the general type MX_2 . They will be divided into two classes in this chapter, pyrites and marcasites. These classes are somewhat loosely defined and include ordered ternary compounds and slightly distorted structures. The final section of the chapter will show the relationships between these two structure types in terms of current theories of their bonding.

1. *Pyrites*

The compound iron pyrite (FeS_2) and its analogues have a cubic structure which may be described in terms of space group $Pa\bar{3}$ (T_h^d). There are four formula units per unit cell with atoms distributed as follows

4 Metals in 4(a): $0,0,0$; $\frac{1}{2},\frac{1}{2},0$; $\frac{1}{2},0,\frac{1}{2}$; $0,\frac{1}{2},\frac{1}{2}$

8 Non-metals in 8(c): $\pm(x,x,x)$; $\frac{1}{2}+x,\frac{1}{2}-x,\bar{x}$; $\bar{x},\frac{1}{2}+x,\frac{1}{2}-x$; $\frac{1}{2}-x,\bar{x},\frac{1}{2}+x$.

The positional parameter x can take on values in the range 0.36 to 0.42.

The pyrite structure is shown in Figure 4.1; it will be noted that the metals are surrounded by six non-metals. These non-metals are equidistant from the metal and are positioned at the vertices of an octahedron of symmetry $\bar{3}$. The non-metals occupy a site of symmetry 3, and are bonded to three metals and one non-metal in a tetrahedral arrangement, the three fold axis lying along the non-metal - non-metal bond.

A number of ternary compounds of the type MXX' have been

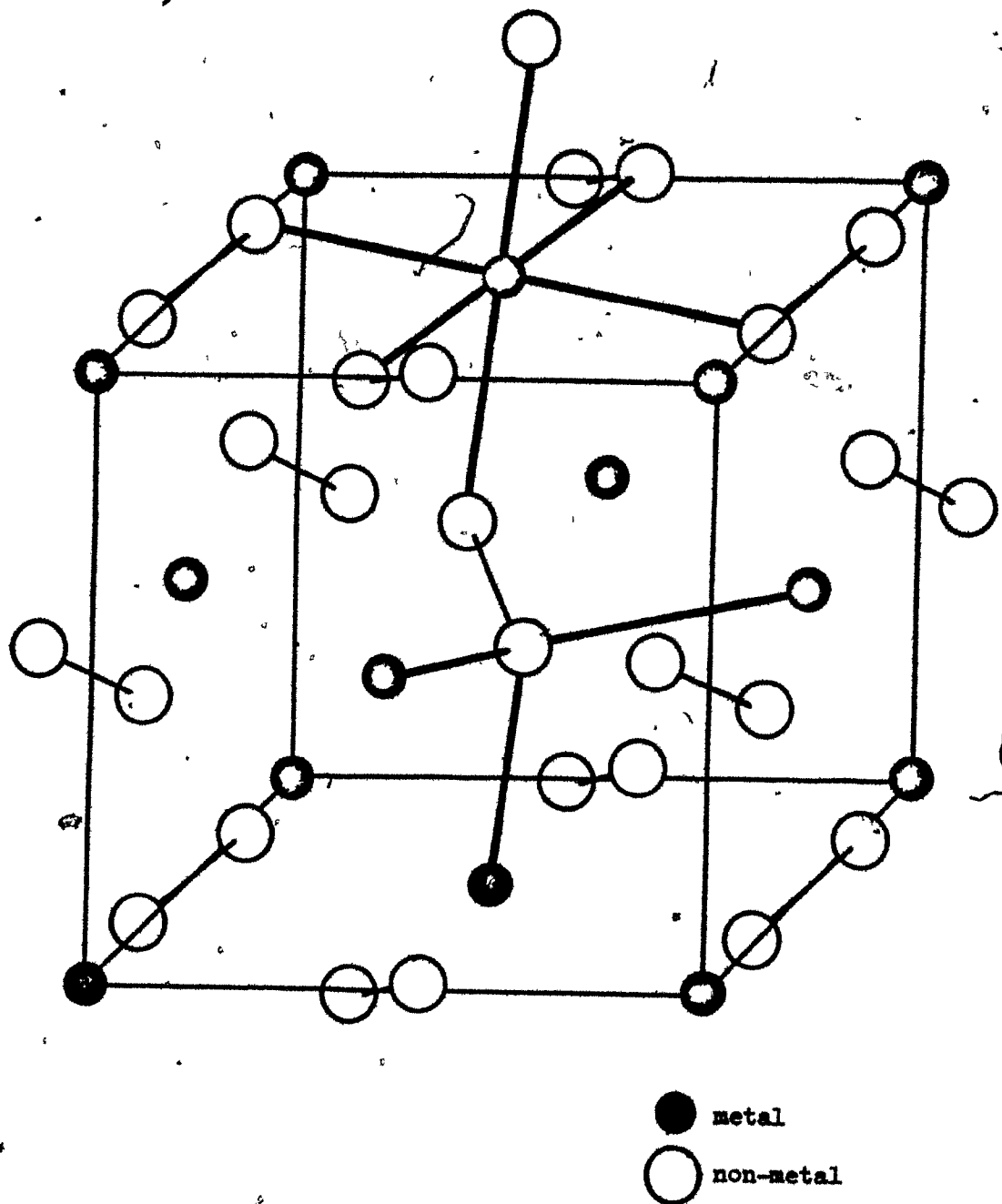


Figure 4.1. The structure of Pyrite

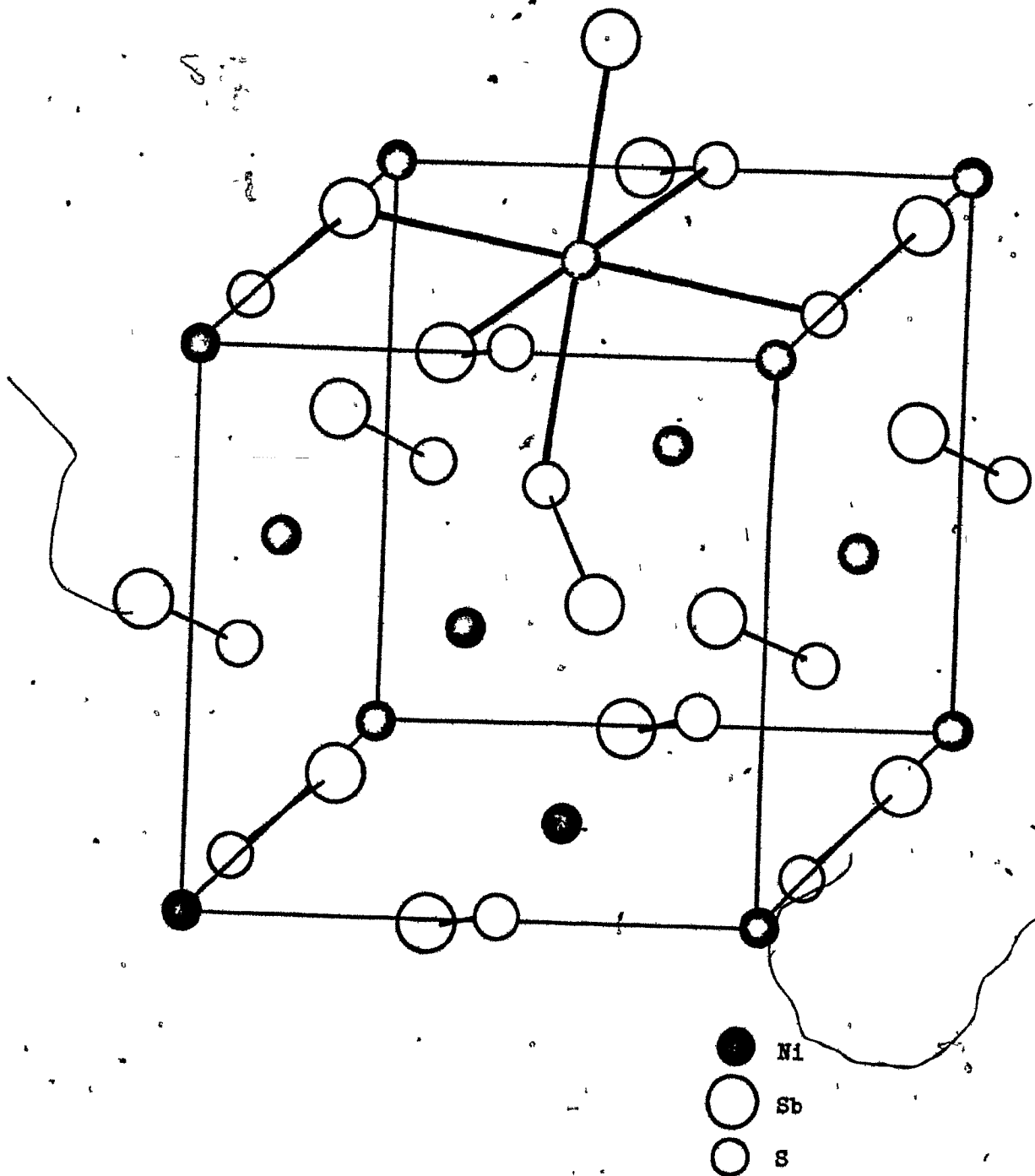


Figure 4.2. The structure of Ullmanite (NiSbS)

reported in the literature (2, 32) to have the pyrite structure, or a similar structure in which there is an ordering of the non-metals X and X'. These compounds are of two general types, those in which X and X' belong to the same group of the periodic table, and those in which they belong to different groups. The first type of compound is usually not a discrete composition, but rather part of a solid solution $MX_2 - MX'_2$ (33). Ordering of X and X' would not be anticipated in such compounds and no evidence of it has been reported. The second type of compound frequently has a limited compositional range (34), implying some special property of X and X' being present in equal numbers. However, the existence of ordering is often not observable, and in many cases X and X' have very similar x-ray scattering powers. An exception is the series of compounds $MSbS$ ($M = Ni, Pd, Pt, Rh, Ir$) in which x-ray reflections not consistent with space group $P4_3$ have been observed, indicating an ordering of Sb and S. The compound $NiSbS$ has been investigated and a structure similar to that of pyrite with ordering in the form of Sb - S pairs (Figure 4.2) was found (35). The remaining compounds in this series have been assumed on the basis of similarity of their x-ray powder patterns to have the same structure (32). It should be noted, however, that there are many possible arrangements for the non-metals and these can not be ruled out entirely without a detailed investigation.

2. Marcasites

The marcasite modification of FeS_2 and a number of similar compounds possess the orthorhombic structure shown in Figure 4.3. When examining natural marcasite Buerger (36) found that the systematic

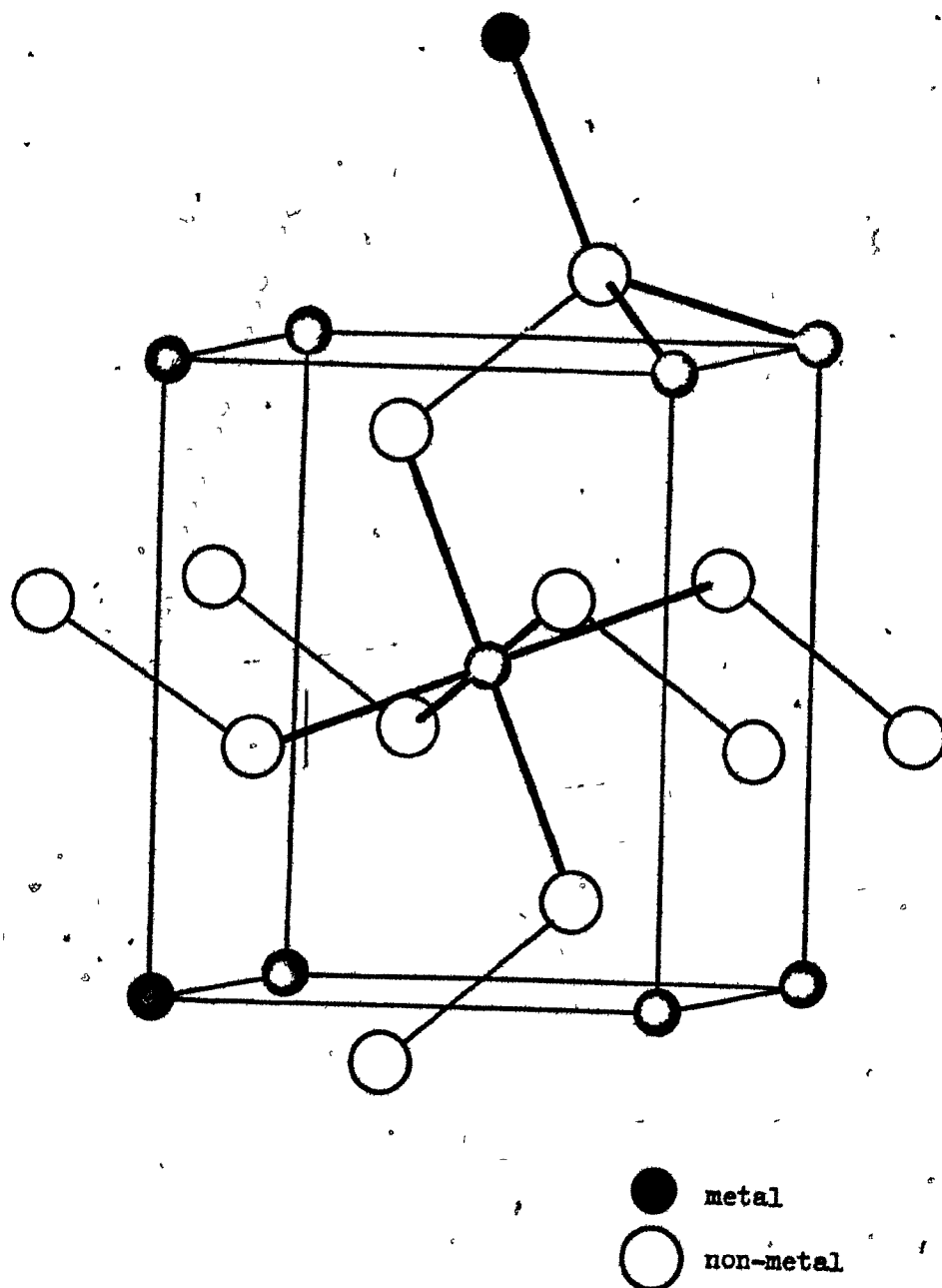


Figure 4.3. The structure of Marcasite.

absences of x-ray reflections were consistent with the space groups $Pn\bar{m}m$ and $Pmn2$. Buerger chose the higher symmetry metal site of $Pn\bar{m}m$ and successfully refined the structure in terms of this space group. A recent investigation of several compounds with the marcasite structure (37) has shown that $Pmn2$ is the more probable space group, however the resulting atomic arrangement is virtually identical with that found by Buerger, the difference being a slight displacement of the atoms from the more symmetric positions of $Pn\bar{m}m$. Whilst a comparison of Figures 4.1 and 4.3 shows the similarity of the local environments of the metals and non-metals in both the pyrite and marcasite structures, these environments do differ. The pyrite structure requires that the six non-metals surrounding each metal are equivalent and equidistant from the metal. This requirement is reflected in the three metals coordinated to each non-metal. The marcasite structure, however, results in three metal - non-metal bonding distances as a consequence of the lower symmetry of the atomic sites. The major difference as far as this work is concerned is the lack of a threefold or higher axis of symmetry at the marcasite atomic sites, whereas the pyrite sites all have at least a threefold axis. This difference allows the assumption of an axially symmetric electric field gradient in the pyrites (thus the Mössbauer asymmetry parameter η will be zero), whereas the axial symmetry is not present in the marcasites and the electric field gradient becomes a more difficult quantity to handle.

Compounds with the marcasite structure fall into two distinct groups which may be categorised by their c/a ratios. These groups are

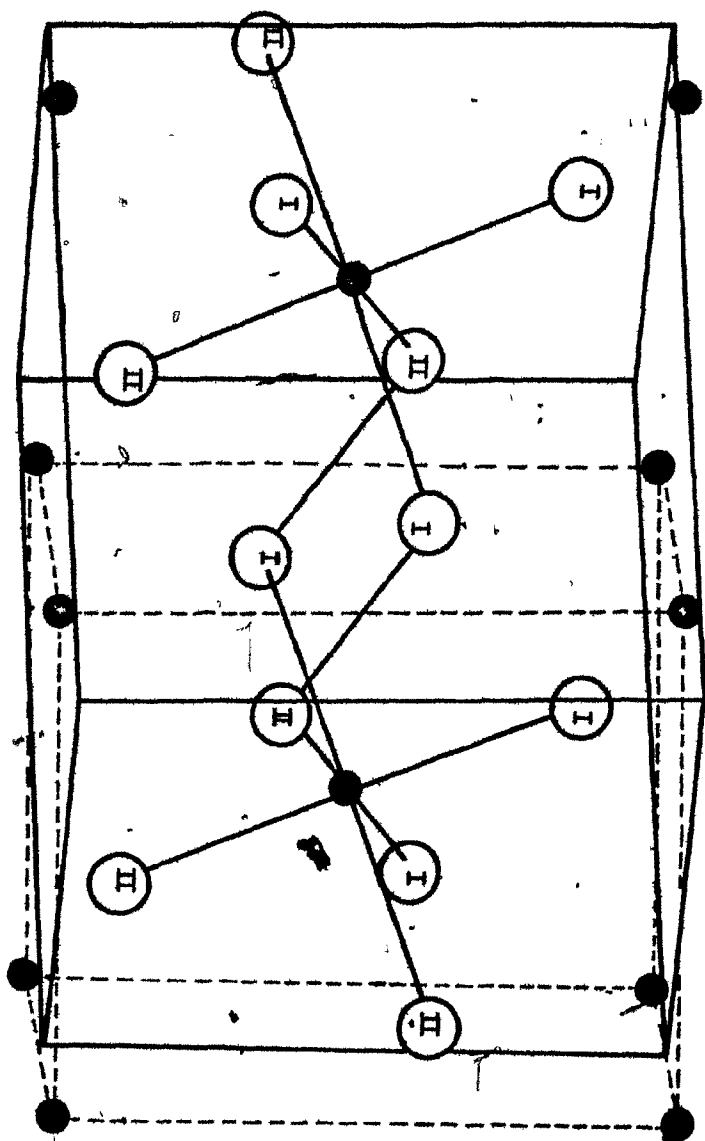



Figure 4.4. The arsenopyrite (CoSb_2) structure.

I and II refer to the two non-metal sites.

commonly referred to as class A ($c/a \sim 0.54$) and class B ($c/a \sim 0.76$) marcasites. The difference in c/a ratios is dependent on the occupation of ' t_{2g} ' d-orbitals on the metals, although the nature of the difference between the two classes is still the subject of much discussion (4, 6). There exists a third class of compounds which have a monoclinic unit cell and belong to space group $P2_1/c$. The atomic arrangement is similar to that of marcasite and the compounds can be indexed on the basis of a pseudo-marcasite unit cell which is only slightly distorted from orthorhombic. If this is done a c/a ratio of ~ 0.64 is found and these compounds are loosely referred to as belonging to class A/B. The main distinction of these compounds is that the non-metals are divided into two sets of equivalent sites. The class A/B structure is shown in figure 4.4 with its relationship to the marcasite unit cell.

3. Bonding Theories

Various authors have explained properties of these compounds in terms of ionic (2, 5, 38), covalent (39) and metallic (40) bonding schemes. However as the majority of the compounds are semiconductors any realistic bonding scheme must be expressed in terms of band theory. Several authors have proposed such schemes which are necessarily quite similar, though they do vary in details, especially concerning the grouping of the marcasites. It is notable that most authors ignore the non-metals except as a source of electrons or σ bonds. The only discussions of the X - X bonds are due to Elliott (5) and Kjekshus and Nicholson (41), both of these depend primarily on the variation of



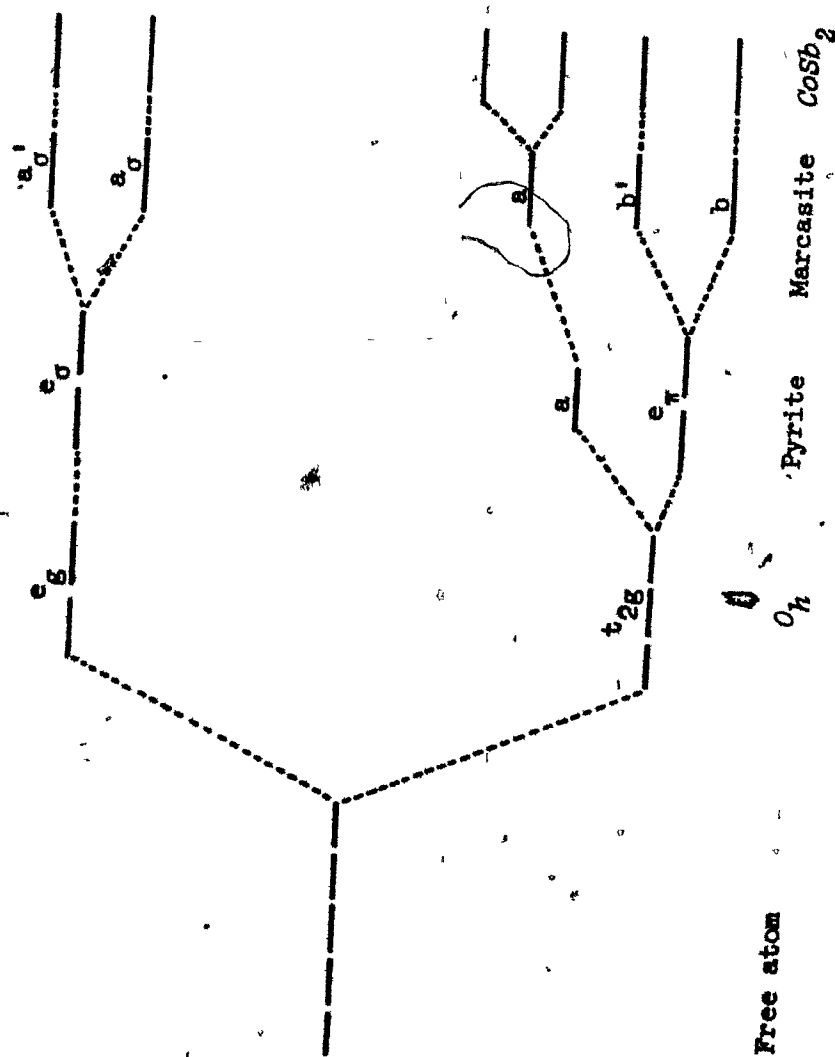


Figure 4.5. Effect of site symmetry on metal d-orbital energies.

4

X - X distances within series of compounds. However, the accuracy to which these distances are known is inherently low. A typical case is the pyrite structure where the bonding X - X distance l is given by

$$l = a_0(1 - 2x)/3,$$

x being the non-metal positional parameter: thus

$$dl/dx = -2a_0/3.$$

If a unit cell edge of about 6\AA is assumed then a typical uncertainty of ± 0.001 in x will lead to $dl = \pm 0.02\text{\AA}$, which is of the same order of magnitude as the variations found in series of compounds.

The valence electron configurations of the metals and non-metals are $(n-1)d^p ns^2$ and $n's^2 n'p^q$ respectively. The d-electron energy levels of the metal are modified by the surrounding non-metals, whilst the energy differences are not easily calculable: the ordering of the orbitals is dependent upon the site symmetry as is shown in Figure 4.5. As the coordination of the metal sites in these compounds is that of a distorted octahedron, the dominant splitting of the d-orbitals will be that due to a symmetry O_h , i.e. into two sets designated e_g and t_{2g} . The distortion of the octahedron will cause further splitting; however, the two sets of d-orbitals will be loosely referred to by these designations. The energy level diagram shown in Figure 4.6 indicates a general bonding scheme for these compounds, the number of electrons per formula unit that can be accommodated in each band being indicated in brackets. As can be seen the $n's$ and $n'p$ orbitals of the non-metals are treated as a whole; the near tetrahedral coordination implies that something similar to sp^3 hybridisation may be expected. One of these orbitals from each non-metal is used in the formation of a σ_{X-X} bond, each atom contributing one electron. The remaining three orbitals are

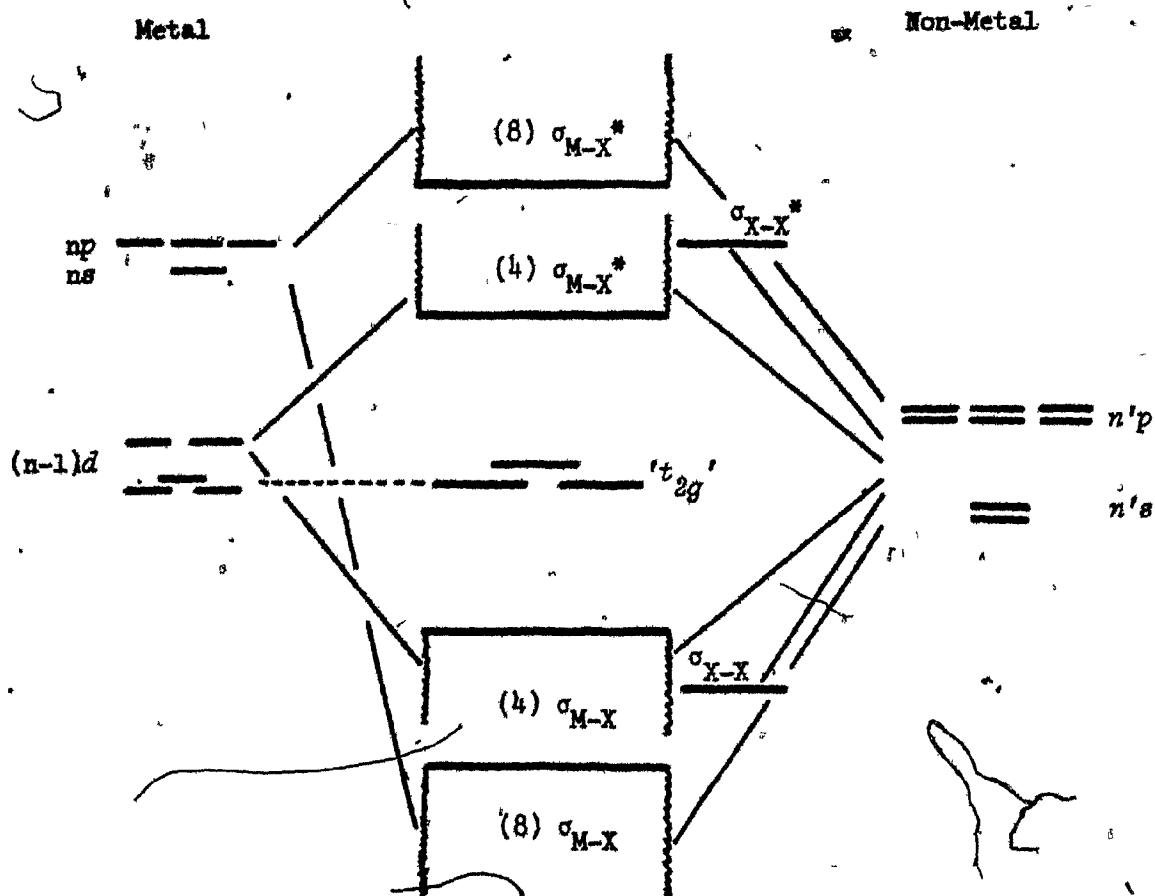


Figure 4.6. Proposed bonding scheme for MX_2 compounds.

used with the $(n-1)s$, ns and np orbitals of the metal to form σ_{M-X} bonds. After forming pairs each non-metal is left with $q+1$ valence electrons, thus the six non-metals contribute $2(q+1)$ electrons to the σ_{M-X} bonds, the remaining $12-2(q+1)$ being contributed by the metal. After this filling of the bonding σ orbitals the remaining $p-2(4-q)$ electrons are located in the metal t_{2g} orbitals, these orbitals being essentially non-bonding, although in the arsenopyrites one of them is involved in the formation of metal-metal bonds. It is the number of electrons in the t_{2g} orbitals that causes the variations of properties in the compounds, the localising of the electrons leading to semiconductors, whereas if $p-2(4-q) > 6$ or the t_{2g} orbitals overlap the σ_{M-X}^* bands a metallic conductor will result.

Elliott (5) has described the bonding of the non-metal pairs in terms of an ionic X_2^{n-} group. He attributes the observed variations in the X-X distance to covalency effects. As the compounds in question can not be considered to be predominately ionic, a preferable approach is to consider an sp^3 hybridised non-metal. The variations of the X-X distance can then be ascribed to electronegativity differences (ionicity effects), deviations from ideal sp^3 geometry, and possibly occupation of the σ_{X-X}^* orbital.

Chapter 5.

METAL ENVIRONMENTS

1. *Introduction*

In principle the Mössbauer spectrum of a single compound should be directly comparable with theory to give chemical information about the compound. Theory is, however, not yet capable of predicting spectral parameters in most cases, and in addition the required nuclear parameters are not known sufficiently accurately. Consequently Mössbauer spectra are most easily analysed in terms of chemical bonding when a series of similar compounds are available and variations between spectra can be semi-quantitatively related to a bonding scheme. In using this approach for the present work several factors had to be considered, not the least being the existence of compounds with the required structures. In the case of the diantimonides considered later the small number of such compounds allowed all the known examples to be examined, however it precluded the examination of a range of compounds with optimum structural characteristics. The examination of the metal site using ^{57}Fe as a probe allowed a much greater choice of compounds as both metal and non-metal could be varied. As variations in Mössbauer spectra are to be correlated with structural and bonding variations it is preferable to choose a structure type with a minimum of variable parameters. Amongst the structures considered in this work the cubic pyrites are the most attractive in this respect. The $\bar{3}$ symmetry of the metal site requires that the octahedral environment of the metal is

distorted in such a way that the six metal - non-metal (M-X) bonds are equivalent. The threefold symmetry axis also ensures that the asymmetry parameter η of the electric field gradient is zero simplifying any interpretation of the quadrupole splitting. As a consequence the majority of compounds investigated using ^{57}Fe were of the pyrite structure.

The Mössbauer spectra of most iron-containing pyrites, marcasites and arsenopyrites have already been examined in varying detail (42, 43, 44, 45, 46), the results which are pertinent to this work are listed in Table 5.1. Gallagher et al. (8) have investigated the series $\text{Co}_{1-x}\text{Fe}_x\text{S}_2$ explaining their results in terms of lattice expansion. Their low-temperature spectra for $x=0.01$ and 0.25 show a pronounced asymmetry which was also observed in the course of this work. This asymmetry is due to ferromagnetic ordering at the cobalt atoms and is analysed in some detail in the final section of this chapter. ^{57}Fe -doped MnS_2 , MnSe_2 and MnTe_2 have also been examined (47) and a pressure dependent transition of the iron atoms from a high-spin to a low-spin state observed. As these are apparently the only cases in which the substituent iron takes on a high-spin state they are not directly comparable with the present work. The structures and physical properties of the compounds discussed have been the subjects of numerous investigations; a summary of the relevant results is given in Table 5.2.

2. Experimental and Results

The compounds discussed in this chapter were all prepared by the techniques described in Chapter 2. In addition to x-ray characterisation of the compounds the Mössbauer spectra were critically examined

Table 5.1 Mössbauer ^{57}Fe Parameters for some Pyrites, Marcasites and Arsenopyrites at Room Temperature.

Compound	Isomer Shift* mm/s	Quadrupole Splitting mm/s	Reference
$\text{FeS}_2(\text{p})$	0.310(4)	0.614(6)	42
	0.30(2)	0.61(1)	45
	0.30	0.615	46
$\text{FeS}_2(\text{m})$	0.273(4)	0.506(7)	42
	0.22(2)	0.495(10)	45
$\text{FeSe}_2(\text{m})$	0.391(6)	0.584(10)	42
	0.39(3)	0.65(4)	45
FeTe_2	0.467(7)	0.502(11)	42
	0.455(20)	0.483(10)	45
FeP_2	0.08(3)	2.10(3)	45
FeAs_2	0.310(9)	1.68(4)	43
	0.27(2)	1.68(2)	45
FeSb_2	0.451(6)	1.281(16)	42
	0.452(6)	1.268(6)	44
	0.49(2)	1.22(1)	45
FePS	0.16(2)	1.52(4)	45
FeAsS	0.23(2)	1.05(2)	45
FeSbS	0.32(4)	1.01(3)	45

* Isomer shifts relative to iron metal

Table 5.2. Structural and physical properties of some pyrites, marcasites and arsenopyrites.

J^+	Compound	a_o	b_o	c_o	$M-X^S$	X-X _o	Magnetic data [#]	Electric data [#]
4	FeP ₂	4.9732	5.6570	2.7235	2.259	2.237		S: 0.4
	FeAs ₂	5.3013	5.9859	2.8822	2.40	2.41	P: t.i.	S: 0.2
	FeSb ₂	5.8328	6.5376	3.1973	2.590	2.887	P: non C.W.	S: 0.17
	FePS							S
5	FeAsS	9.15	5.65	6.42	2.30	2.30		S
	FeSbS	10.04	5.93	6.68				S
	FeS ₂ (p)	5.4179			2.262	2.177	D	S: 0.9
	FeS ₂ (m)	4.4431	5.4245	3.3871	2.247	2.223	D	S
6	FeSe ₂	4.7987	5.7806	3.5827	2.38	2.51	D	S: 0.6
	FeTe ₂	5.2655	6.2679	3.8738	2.567	2.926	P: 2800.6	S: 0.46
	OsSe ₂	5.9449			2.477	2.44	D	S
	OsTe ₂	6.3968			2.647	2.83	D	S: 0.2

Table 5.2. (Continued)

7	CoS ₂	5.5356	2.323	2.119	F:P:2S ₀₁	M
	CoSe ₂	5.5893	2.438	2.45	P:2S ₀₁	M
	CoTe ₂	5.3294	6.3223	3.9080	P	M
	RhSe ₂	6.002	2.597	2.914		
	RhTe ₂	6.441	2.50	2.50		
			2.65	3.07		
8	NiS ₂	5.6873	2.401	2.06	P:2S ₀₂	S:0.32
	NiSe ₂	5.9629	2.488	2.42	P: non C.W.	M

† No. of electrons not required for bonding, see text

‡ Lattice parameters in Å, if the structure is pyrite only a₀ is given

§ Marcasites have two non-equivalent M-X bonds, a weighted mean is given

P paramagnetic, D diamagnetic, F ferromagnetic

* M metal, S semiconductor ΔE in eV.

Table 5.3. Results of ^{57}Fe Mössbauer Experiments

Compound [†]	Temperature °K	Isomer Shift [‡] mm/s	Quadrupole Splitting mm/s	χ^2 §
$\text{FeS}_2(\text{p})$	298	0.305(3)	0.613(4)	171/194
$\text{FeS}_2(\text{m})$	298	0.271(4)	0.508(5)	263/251
CoS_2	298	0.370(3)	0.307(2)	198/194
	91	0.460	0.33(3) [#]	-
NiS_2	298	0.442(5)	0.283(4)	176/194
	77	0.533(4)	0.265(10)	184/194
CoSe_2	298	0.468(2)	0.369(3)	245/251
	91	0.529(4)	0.386(4)	246/251
NiSe_2	298	0.494(6)	0.103(10)	198/194
	77	0.59(4)	0.135(14)	167/194
RhSe_2	298	0.553(4)	0.395(5)	234/251
RhTe_2	298	0.575(3)	0.452(5)	270/251
OsSe_2	298	0.500(4)	0.886(4)	277/251
OsTe_2	298	0.546(4)	0.877(4)	242/251
FeSb_2	298	0.446(3)	1.264(10)	273/251

[†] Compounds shown as containing no iron were $\text{M}_{0.98}^{57}\text{Fe}_{0.02}\text{X}_2$

[‡] Isomer shifts relative to metallic iron

[§] χ^2 values given in the form $\chi^2/\text{number of degrees of freedom}$

[#] See text

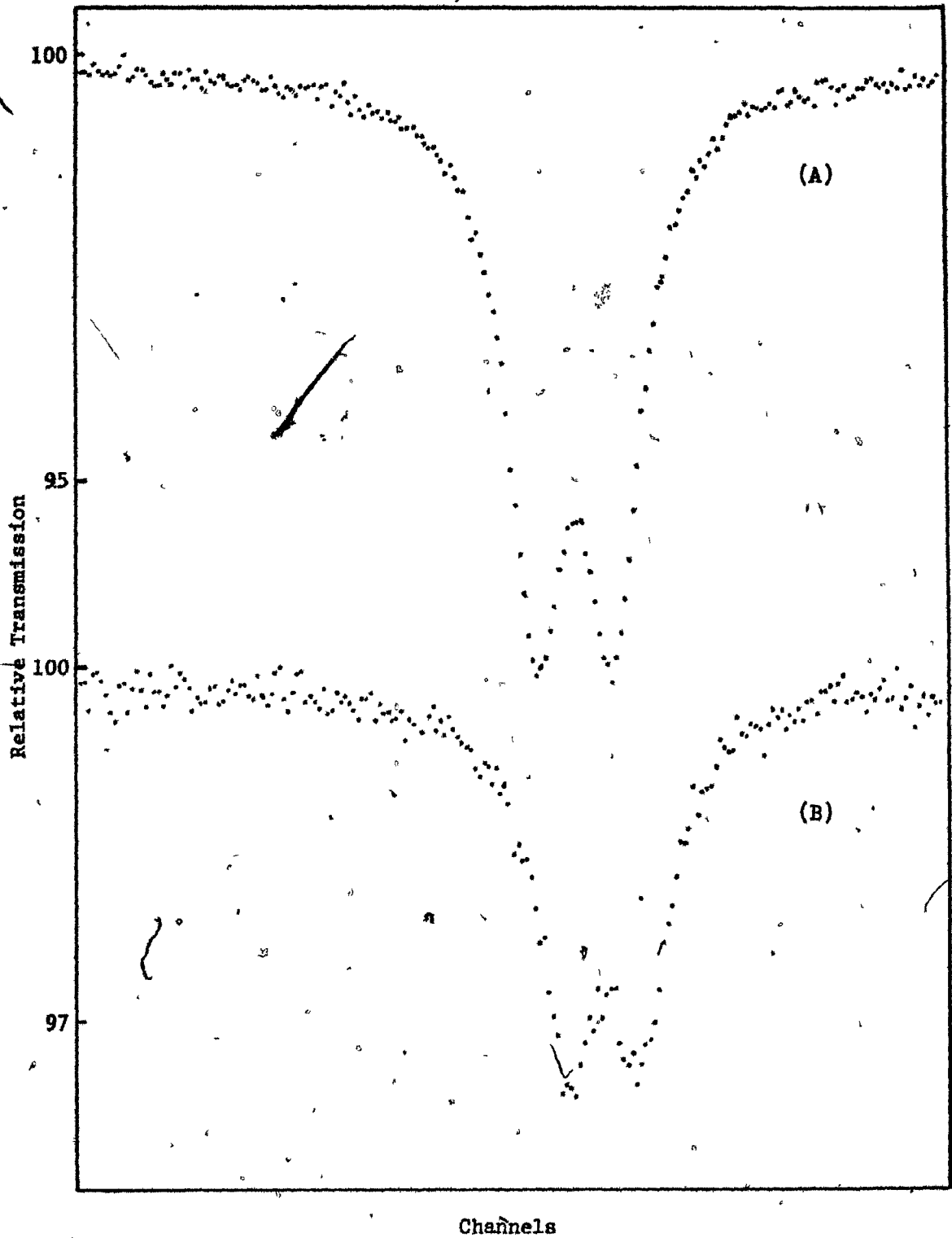


Figure 5.1. Mössbauer spectra of ^{57}Fe doped NiS_2 at
(A) Room temperature, (B) 77°K .

for indications of foreign iron-containing phases. As in the doped compounds the iron constituted somewhat less than 2% of the total sample; this was probably a more sensitive test than x-ray diffraction of the inclusion of all the iron.

Mössbauer spectra were taken of all the compounds at room temperature and of selected samples at liquid nitrogen temperatures. With the exception of $\text{Co}_{0.98}\text{Fe}_{0.02}\text{S}_2$ little change was observed in the spectra upon lowering the temperature. The spectra all consisted of quadrupole doublets, similar to those shown in Figure 5.1, and in all cases (except CoS_2) a good fit was obtained with lines of equal intensity and linewidth. The parameters obtained from these fits are listed in Table 5.3; the low-temperature parameters for CoS_2 were obtained from the analysis described later. The results obtained from FeSb_2 and both modifications of FeS_2 were in good agreement with results previously reported (42, 44, 45). The FeS_2 marcasite sample was a natural one from Folkestone, Kent. The room temperature parameters for $\text{Co}_{0.98}\text{Fe}_{0.02}\text{S}_2$ agreed well with those reported by Gallagher et al. (8) for the similar $\text{Co}_{0.99}\text{Fe}_{0.01}\text{S}_2$.


3. Discussion

The majority of the compounds examined in this chapter contained iron only as a probe substituting for a small percentage of the host metal, and this must be considered when interpreting the results. Ideally a probe will replace the atom being investigated but cause no perturbation of the structure or bonding; this situation is virtually never possible. While the size and shape of the iron occupied sites will

not be identical to that of other metal sites, it is reasonable to assume that they will be closely related. Thus effects such as bond polarisation and variations of electric field gradient measured at the iron sites will be indicative of changes in the host structures.

Another assumption in the use of a probe is that the probe atoms are so distributed in the host structure that they are far enough apart to have negligible effect on each other. In the case of 2% substitution considered here this is not a valid assumption, as nearly a quarter of the iron atoms may have one or more iron atoms as nearest metal neighbours. The effect of these adjacent sites on the Mössbauer spectra is a spread of isomer shifts and quadrupole splittings. As in the present case good fits are obtained with symmetrical doublets and reasonable linewidths it appears that these effects can be neglected.

The compounds under investigation are semiconductors and metals. It is thus reasonable to assume that the Mössbauer parameters are primarily dependent on the local environment of the ^{57}Fe atoms, and variations in these parameters should be relatable to changes in the immediate geometry and bonding of these atoms. If the Mössbauer isomer shifts are plotted against the M-X bond lengths (Figure 5.2), a correlation is observed for compounds containing non-metals belonging to the same group of the periodic table. That isomer shifts for compounds containing different non-metals should fall on the same line seems at first peculiar, but it may be explained as follows. Kjekshus and Nicholson (41) have shown a linear relationship between M-X and X-X for compounds in which M remains the same and X always belongs to the same group; this relationship may be expressed as



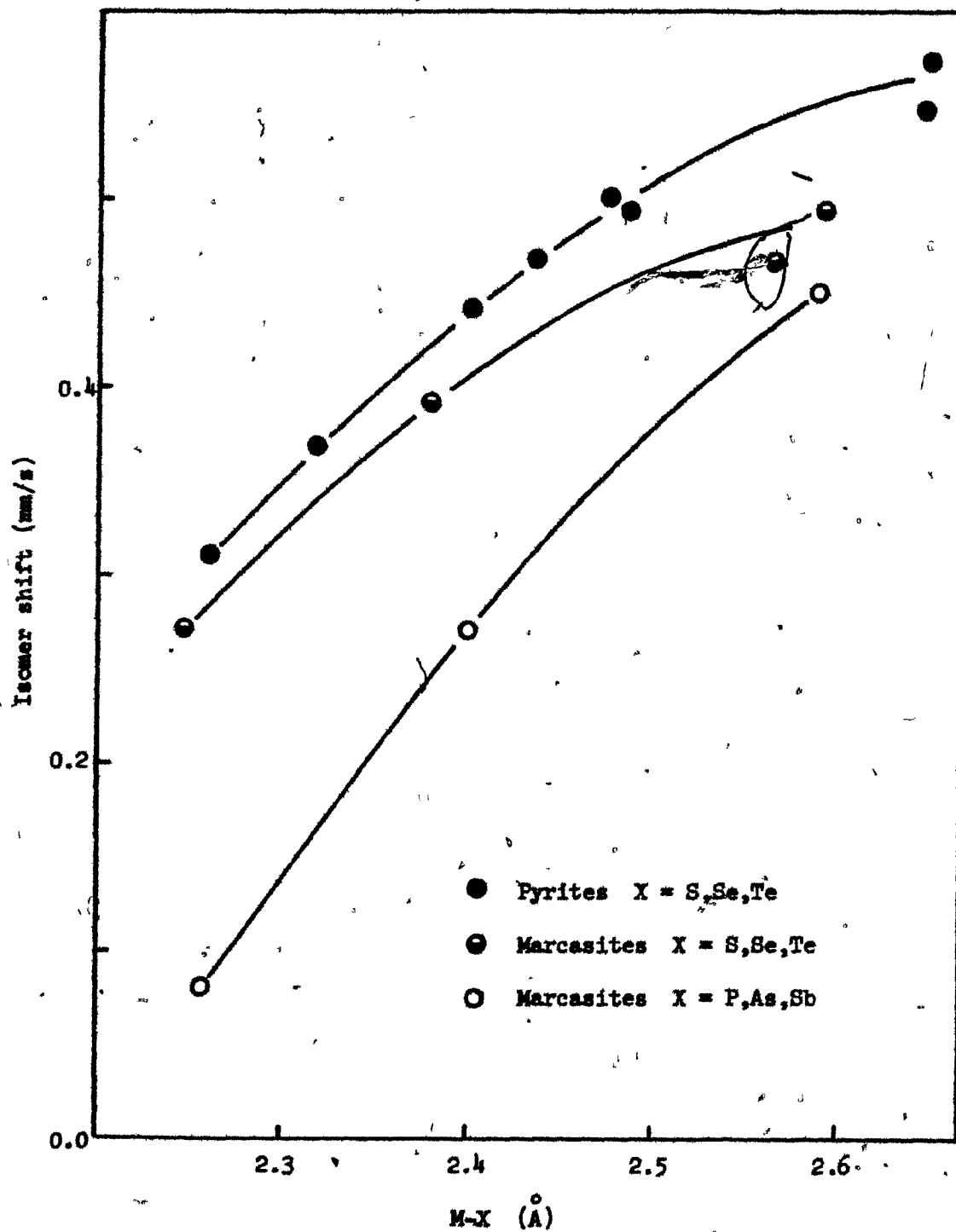


Figure 5.2. Plot of ^{57}Fe isomer shift against metal - non-metal bond length.

$$MX = kXX + c. \quad 5.1$$

It was also found that the lines defined by 5.1 all had the same slope, and the effect of varying the metal was to change c . Thus k is a constant independent of metal and non-metal, whereas c depends only upon the metal. Within the context of the structure types under discussion a metal radius r_M may be defined,

$$r_M = MX - XX/2. \quad 5.2$$

Using the empirical relationship 5.1,

$$r_M = MX(1 - 2/k) + 2c/k. \quad 5.3$$

MX can now be expressed as

$$MX = k'(r_M - 2c/k), \quad 5.4$$

indicating that it is determined by the metal radius plus a quantity that is dependent solely upon the metal. The failure of pyrites and marcasites to fall on the same line is not surprising in that the above argument is probably very structure-dependent. Furthermore, the values for $M-X$ in the marcasites are in fact mean values and the components of the isomer shifts from different bonds can not be expected to combine in the same fashion. The reason for the pnictides having isomer shifts somewhat lower than the chalcogenides lies in the variation of j , the number of electrons per formula unit in excess of the formal bonding requirements. The pnictides have $j = 4$ and the chalcogenides $j > 6$, as these electrons are accommodated in the metal ' t_{2g} ' orbitals the decrease in d -electron shielding accounts for the lower isomer shifts. As the ' t_{2g} ' orbitals will only accommodate six electrons, compounds with $j > 6$ have electrons in the σ^* band. The fact that all the pyrites with $j > 6$ lie on the same line in Figure 5.2 implies that this band does not contribute significantly to the

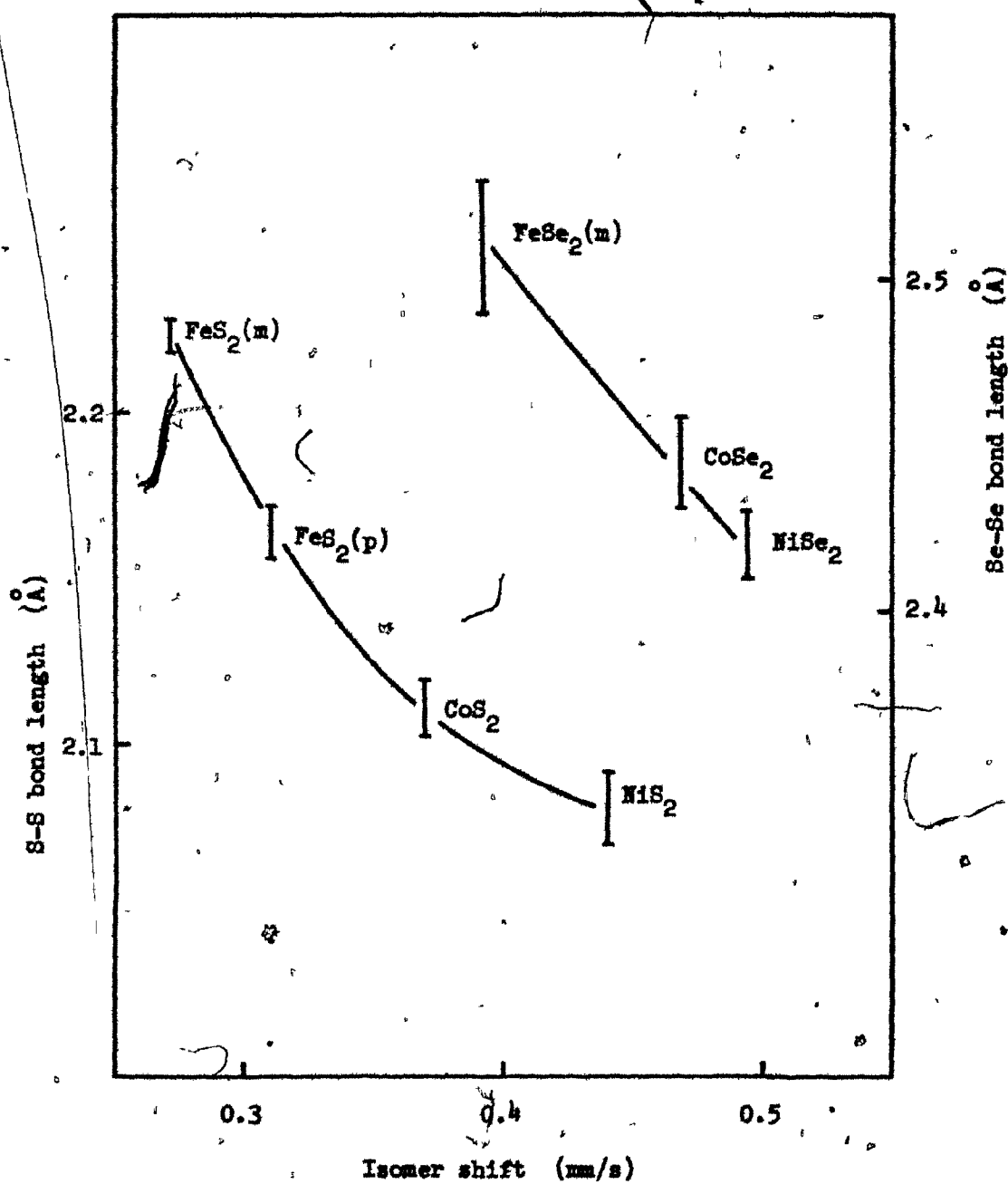


Figure 5.3. Plot of ^{57}Fe isomer shift against X-X bond length for some disulphides and diselenides.

shielding of the metal atoms. This lack of shielding, however, may well be an artefact of the use of iron as a probe in that the iron chalcogenides have a $j = 6$ configuration which could lead to a localised depopulation of the σ^* band in the doped compounds. The trend of the isomer shift to increase with increasing M-X shown in Figure 5.2 is consistent with an increase in r_M with a subsequent decrease in $|\psi(0)|^2$. That the doped samples follow a trend similar to the FeX_2 samples indicates that the changes in r_M with M are the cause of similar changes at the ^{57}Fe sites. A similar trend of isomer shift with volume has been observed in pyrite under pressure by Vaughan and Drickamer (46).

The variation of S-S bond length in the pyrites was noted by Elliott (5) and attributed to covalency effects in what was basically an ionic bonding scheme. If Elliott's basic explanation is carried over to the more reasonable covalent bonding scheme, it takes the form of a polarisation of the M-X bonds which may be varied by changing M. The greater this polarisation the greater will be the like charges on adjacent non-metals which will force an increase in the X-X bond length. As polarisation will also cause a depletion of the electrons about the metal atoms, with a consequent reduction in $|\psi(0)|^2$, a correlation between isomer shift at the metal site and X-X bond length is to be expected. Figure 5.3 shows a plot of isomer shift against X-X for some sulphides and selenides, in which it will be noted that the isomer shift increases with decreasing bond length, i.e. the opposite effect to that predicted above. It should be noted however that the decrease in X-X is accompanied by both an increase in M-X and

a filling of the σ^*_{M-X} band, both of which would cause the observed variation of isomer shifts.

Quadrupole splittings are usually somewhat more difficult to interpret than isomer shifts because there are often several competing contributions to the electric field gradient. In the case of pyrites and marcasites, which are semiconductors with narrow band gaps or metals, it is unlikely that a major contribution can be expected from ionic sources. The predominant sources of the electric field gradients can be expected to be the non-cubic distribution of M-X bonds, and the partially filled d-orbitals on the Mössbauer atoms. Figure 5.4 shows the dependence of the quadrupole splitting on j , the occupancy of non-bonding and antibonding orbitals. Values of $j < 6$ correspond to vacancies in the metal t_{2g} orbitals which give rise to quite large quadrupole splittings. A detailed study of the ^{57}Fe quadrupole splitting in FeSb_2 has been made by Steger and Kostiner (44), showing that the temperature variation is consistent with a splitting of the t_{2g} orbitals into an a and two lower energy b orbitals. The low-temperature quadrupole effect corresponds to an empty a orbital, whereas at room temperature thermal energy causes population of this orbital and a significant reduction in the splitting. For values of $j > 6$ the t_{2g} orbitals are filled and can no longer be expected to make a major contribution to the quadrupole splitting. The splitting will now be governed by the asymmetry of the charge distribution in the M-X bonds, which in itself is governed by both geometrical and polarisation effects. It is noticeable that the quadrupole splitting for $j > 6$ is significantly less than that for $j = 6$. This corresponds to a population of the σ^* conduction band which will tend to reduce any

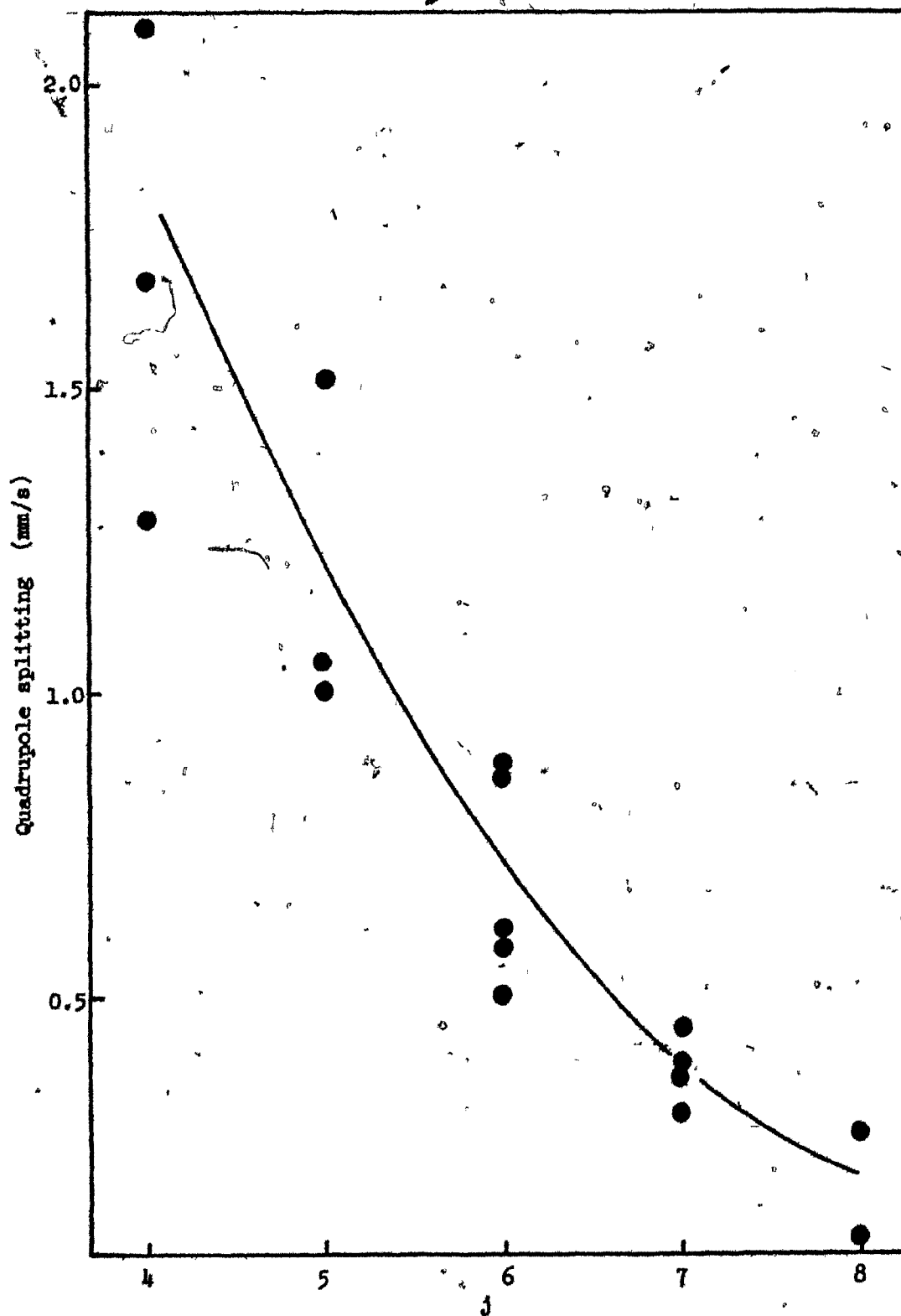


Figure 5.4. Plot of ^{57}Fe quadrupole splitting against j .

disparity in charges between atoms. As the values for $j > 6$ come from ^{57}Fe used as a probe it is possible that the d^* band is somewhat depleted in the vicinity of the Mössbauer atoms. However, the effect described would certainly be transmitted through the non-metals.

4. Transferred Hyperfine Field at ^{57}Fe in $\text{Co}_{0.98}\text{Fe}_{0.02}\text{S}_2$

The compound CoS_2 is unique amongst the pyrites in that it orders ferromagnetically. The Curie temperature has been reported variously as 110(7,48,49), 116(50), 118(7), 122(51,52), 124(53) and 130°K (54). Above the Curie temperature the susceptibility exhibits a Curie-Weiss behaviour with an effective magnetic moment of 1.80-1.85 μ_B (48,49,54); a value of 2.17 μ_B has also been reported (50). This moment corresponds to one unpaired electron per Co atom, i.e. a $t_{2g}^6 e_g^1$ configuration. Below the Curie temperature the saturation magnetisation has a value of 0.84 μ_B per Co atom (53), which is slightly smaller than the theoretical value of 1 μ_B that would be expected for a completely spin-polarised localised-electron model. Jarrett *et al.* (55) have suggested that the reduced moment observed is consistent either with a canted arrangement of the Co spins, or, more likely, with an itinerant electron model in which the splitting between the spin-up and spin-down bands is smaller than the bandwidth. As well as magnetic investigations CoS_2 has also been the subject of a powder neutron diffraction study at temperatures down to 4.2°K (56). This study confirmed the ferromagnetic order, but the high space group symmetry precluded any further inferences being made about the magnetic structure. It having been shown that

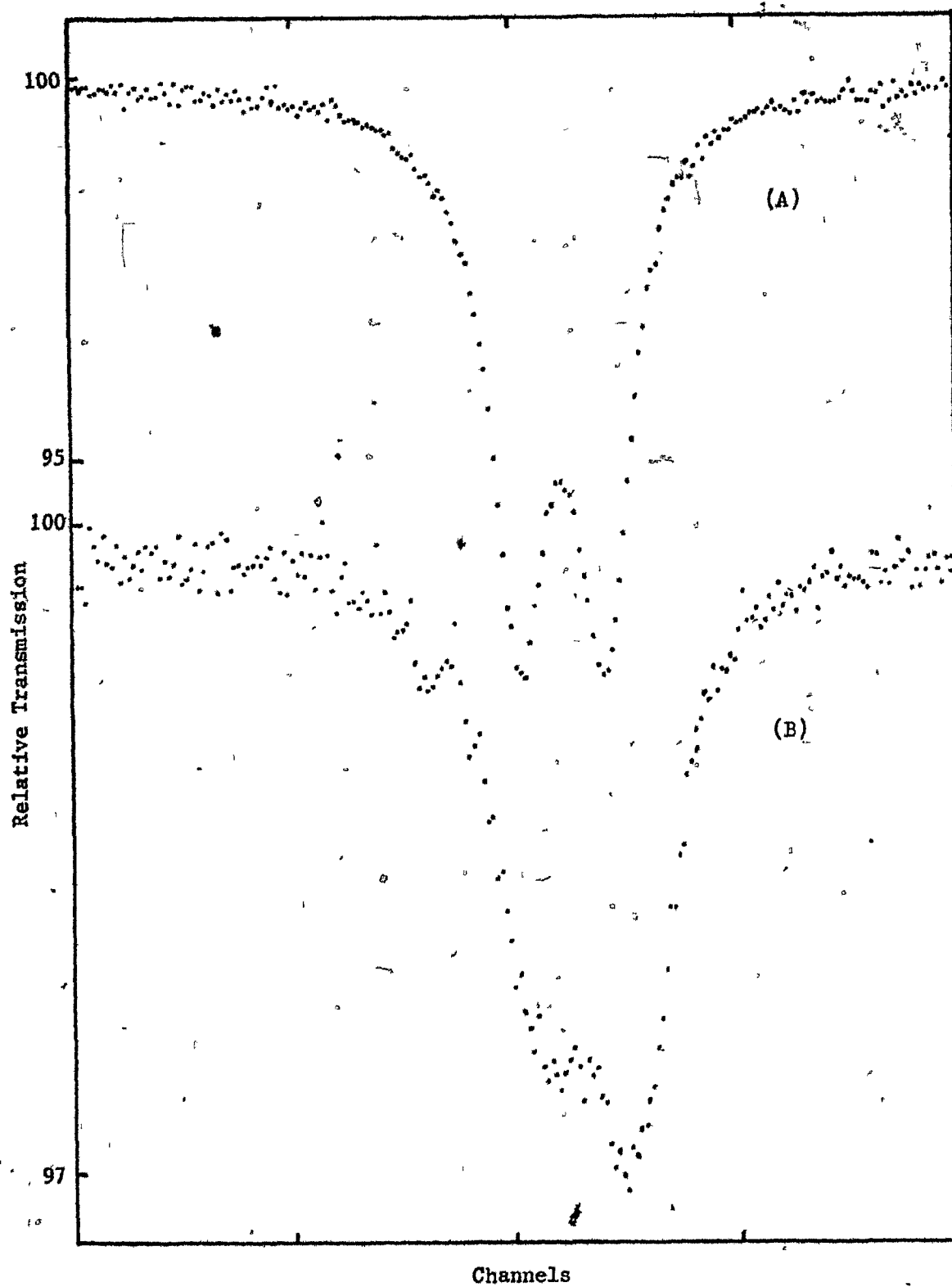


Figure 5.5. Mössbauer spectra of ^{57}Fe doped CoS_2 at (A) room temperature and (B) 77°K .

the determination of the magnetic structure of a cubic (or pseudo-cubic) compound by neutron diffraction requires the use of a single crystal comprising of a single domain (57). Thus the magnetic structure of CoS_2 remains undetermined.

Mössbauer spectra of a series of solid solutions $\text{Co}_{1-x}\text{Fe}_x\text{S}_2$ ($x = 0.01, 0.25, 0.5, 0.75$) at temperatures well below the respective Curie temperatures have been reported by Gallagher *et al.* (8). These spectra are presented as single quadrupole doublets; they contain no evidence of any six line spectra that would be expected for Fe atoms with $S > 0$, thus giving assurance that the Fe atoms remain in a t_{2g}^6 configuration. However for $x = 0.01$ and 0.25 the spectra at 100°K shown in Figure 3 of reference 8 appear asymmetric with the possibility of some line broadening, although no values were quoted for linewidths. In the course of the present work the compound $\text{Co}_{0.98}\text{Fe}_{0.02}\text{S}_2$ was prepared and Mössbauer spectra taken at room temperature and 91°K (Figure 5.5). The 91°K spectrum is very similar to that reported by Gallagher *et al.* for $x = 0.01$ at 100°K indicating that the asymmetry is a real effect and not due to some instrumental error. This asymmetry is unlikely to arise from Gol'danskii-Karyagin, relaxation, or preferred orientation effects since a two line fit with no constraints gave an unacceptable χ^2 value of 688; the acceptable range of χ^2 values for this fit being 198 to 302. An asymmetric spectrum of this type is, however, expected if in addition to the electric field gradient at the ^{57}Fe nucleus there is also a small static magnetic field. The spectrum has been analysed in terms of this model, and it has been found possible

to propose a magnetic structure for CoS_2 as a result of this analysis.

5. *Simulation of Spectra*

The pyrite structure has the symmetry of space group $\text{Pa}\bar{3} (T_h^6)$ with metal sites at the equipoint $4(a)$. If a magnetic transition causes all the spins of the metal atoms to align collinearly along some general direction, the cubic symmetry of the unit-cell is destroyed and the four metal sites become non-equivalent. As the Mössbauer spectrum is determined by the relative orientation of the magnetic field and the electric field gradient, the spectrum obtained in the case of collinear ordering will be a composite one containing four components that are in general not equivalent. As this type of ordering is the most obvious a series of spectra were simulated, using the programs described in Chapter 3, covering the whole range of possible collinear arrangements. These included the special cases of the magnetic field along; *i*) a unit-cell edge, *ii*) a face diagonal and *iii*) a body diagonal. In order to perform these simulations it was necessary to know the relationship between the various variables. Although in general there are four different component spectra, once the orientation between the magnetic field and the electric field gradient at one metal site is established the other three orientations are fixed by the crystal structure. Thus the composite spectrum resulting from a collinear arrangement is characterised by the magnetic field, the electric field gradient and two directional parameters. The electric field gradients at the four metal sites of the pyrite structure lie along the four body

diagonals of the unit-cell and as the site symmetry is $\bar{3}$ the asymmetry parameter η of the electric field gradient is zero. Lines drawn through the metal sites with the same sense as the electric field gradients would intersect at the centre of the unit-cell. If one of these lines is arbitrarily chosen as a major axis, the other three lines will lie equispaced on the surface of a cone with the chosen line as its axis (Figure 5.6). The magnetic vector H can now be drawn passing through the intersection of the four lines, and the geometric parameters required to determine the Mössbauer spectrum are the angles between each of the four lines and H . As only directions are of interest the calculation can be simplified by assuming all lines to have unit length. The four electric field gradient directions are numbered (Figure 5.6), and the direction of the magnetic field is determined initially by θ_1 and ϕ . As there is no obvious position for $\phi = 0$ this is taken such that line 2 is at that position. A set of cartesian coordinates is set up such that:

$$\begin{aligned} x &= \sin\theta \cos\phi \\ y &= \sin\theta \sin\phi \\ z &= \cos\theta \end{aligned} \quad 5.5$$

where θ is the angle between any vector and line 1. The angle ω between any two vectors (x_1, y_1, z_1) and (x_2, y_2, z_2) is given by the relation

$$\sin(\omega/2) = 2/[(x_1 - x_2)^2 + (y_1 - y_2)^2 + (z_1 - z_2)^2]^{1/2}. \quad 5.6$$

The values of θ_1 required for the simulation can then be determined if (x_1, y_1, z_1) is taken as the direction of H and (x_2, y_2, z_2) as one of the four lines. The values of θ and ϕ for lines 2, 3 and 4 are:

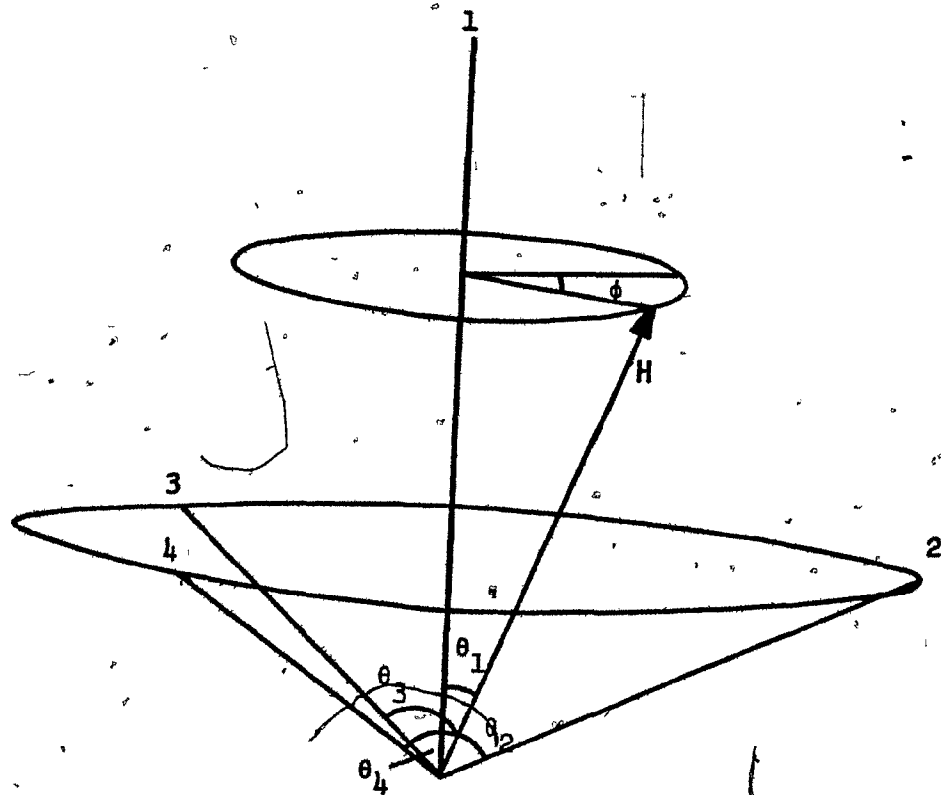


Figure 5.6. Relative orientations of the four body diagonals of a cube and an arbitrary collinear magnetic field.

$$\theta = 2\sin^{-1}(1/\sqrt{3}) = 70^\circ 44'$$

5.7

$$\phi = 0, 2\pi/3, 4\pi/3.$$

As an electric field gradient tensor has sense but not direction the interaction between it and a magnetic field is identical at relative orientations of θ and $\pi - \theta$, so it is only necessary to vary θ_1 between 0° and 90° . Because of the $\bar{3}$ symmetry of the metal site ϕ has only to be varied from 0° to 60° .

Using the above relationships composite spectra were simulated for the whole unique range of θ and ϕ in steps of 15° . All of these simulations produced envelopes that at first sight appeared to be symmetrical doublets, and hence did not agree with the asymmetric profile of the low temperature experimental spectrum. This apparent symmetry could not be removed by varying either the field or the electric field gradient. Thus the simplest magnetic structure, in which the moments on all the metal atoms align collinearly can be discounted, and a different explanation must be sought.

The other possible explanation which was postulated by Jarrett *et al.* (55) is a canted spin arrangement of moments, which would not destroy the equivalence of the metal sites. Thus the simulated spectra for this model contain only one component. A series of spectra were simulated, varying the angle between the magnetic field and the electric field gradient from 0° to 90° and also varying the magnitudes of H and e^2Qq . Figure 5.7 shows a series of simulated spectra for $H = 7$ kOe and $e^2Qq/2 = 0.33$ mm/s, the spectra at 0° and 90° are asymmetric although a reversal of this asymmetry occurs at $54^\circ 44'$ (equivalent to case *i*

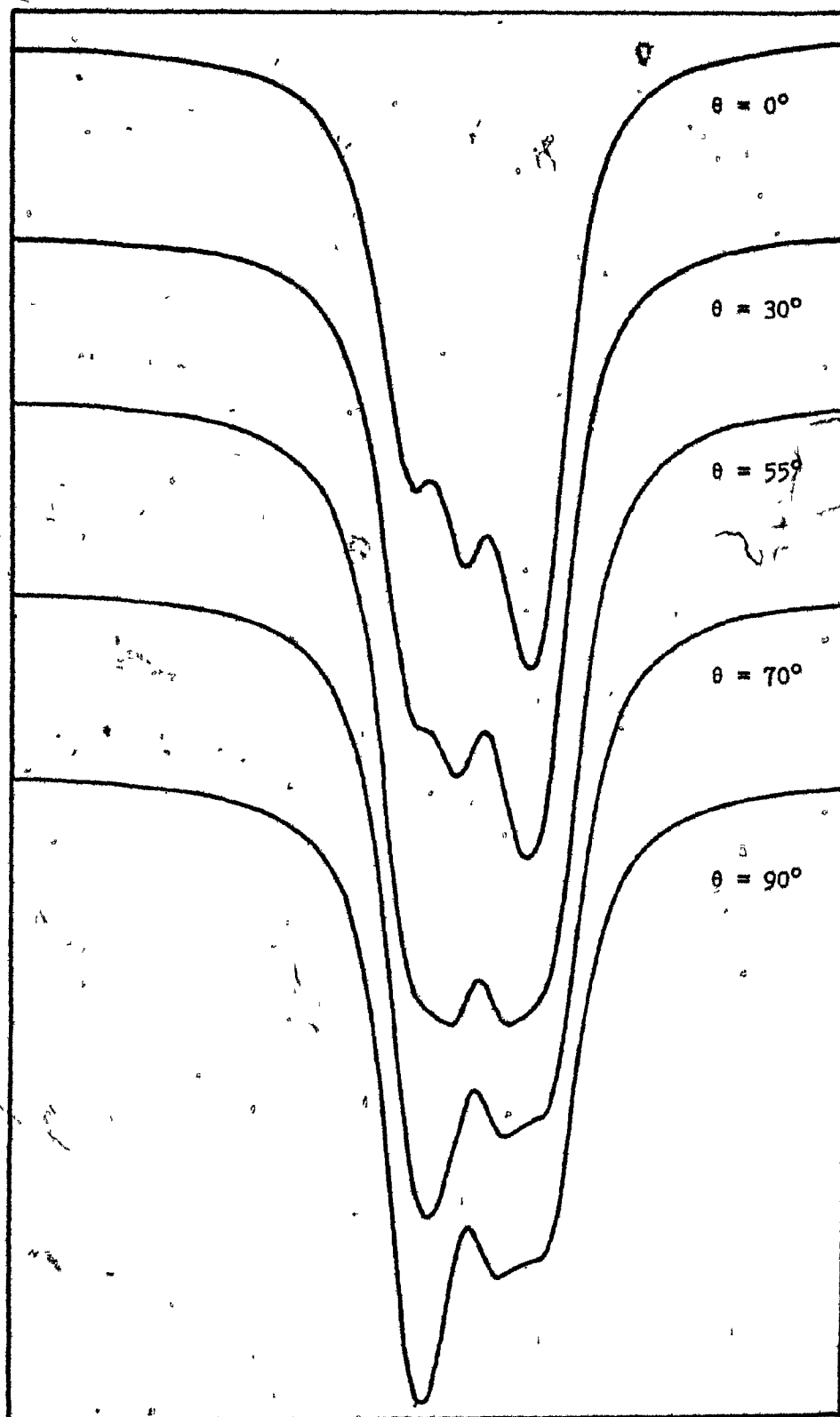


Figure 5.7. A series of simulated spectra for $\text{Co}_{0.98}\text{Fe}_{0.02}\text{S}_2$.
 $H = 7 \text{ kOe}$, $e^2Qq/2 = 0.33 \text{ mm/s}$.

above). If a negative value of e^2Qq is used the same spectrum results, only it is reversed to form a mirror image of that obtained for the positive value of e^2Qq . Because of this mirroring effect it can be seen that two of the simulated spectra in Figure 5.7 are similar to the experimental spectrum. Visual comparison gave parameters of either (A) $H = 7 \pm 1 \text{ kOe}$, $e^2Qq/2 = +0.33 \pm .03 \text{ mm/s}$, $\theta = 75 \pm 15^\circ$, or (B) $H = 6 \pm 1 \text{ kOe}$, $e^2Qq/2 = -0.34 \pm .03 \text{ mm/s}$, $\theta = 30 \pm 15^\circ$. The linewidth was taken as 0.24 mm/s , that of the room temperature spectrum, variations smaller than the quoted uncertainties did not produce any visual changes in the simulated spectra. It is not possible to choose between the two results unless the sign of e^2Qq is known.

These results imply that the magnetic structure of CoS_2 is one in which the spins on the metal atoms are aligned on a helix forming a constant angle with the electric field gradient at the metal site. Such a canted arrangement would account well for the reduced saturation magnetisation mentioned by Jarrett *et al.* (55). It is interesting to note that a similar spin arrangement has been inferred in the antiferromagnetically ordered MnTe_2 from a ^{125}Te Mössbauer study (9).

Chapter 6.

NON-METAL ENVIRONMENTS

1. *Introduction*

Although pyrites and marcasites have been the subject of many investigations very little information about the non-metal sites is available. The Mössbauer effect provides an ideal method for rectifying this situation. There are two non-metals which have Mössbauer isotopes and form a number of compounds with pyrite and marcasite structures; these are antimony and tellurium. Antimony-121 was chosen for the present work as it has been the subject of more investigations which may be expected to provide a good basis upon which to interpret results. In addition tellurium-125 has the disadvantages of a short precursor half-life (60 days) and a very small range of isomer shifts.

A number of transition metal diantimonides MSb_2 have pyrite, marcasite or $CoSb_2$ structures and these provide a basis for investigating the non-metal sites in these structures. As antimony has a full $4d$ shell this is not expected to obscure effects due to varying geometry and bonding parameters as was the case at the metal sites. The non-metal site coordination consists of three metals and a non-metal at the vertices of a distorted tetrahedron. While the diantimonides provide a means of observing the effect of varying the metals, it is also desirable to know what effect the fourth, non-metal, neighbour has on the results

obtained. A series of sulpho-antimonides, $MSbS$ ($M = Ni, Rh, Ir, Pt, Pd$) are reported to have the ullmanite structure (32,35) in which the non-metals are ordered such that Sb-S pairs are formed. These compounds form an ideal series to compare with the disantimonides to observe the effect of varying the non-metal in the coordination polyhedron. In addition a series of compounds $PtSb_{2-x}Sn_x$ exists (58) allowing the comparison of ^{121}Sb and ^{119}Sn results.

2. Interpretation of ^{121}Sb Spectra

^{121}Sb Mössbauer spectra have two distinct features, a large range of isomer shifts and a complicated quadrupole-split spectrum due to the $7/2 \rightarrow 5/2$ transition, which although it is rarely well resolved makes readily available the sign of e^2Qq . It is proposed in this section to outline the ways in which these features may be used in the interpretation of ^{121}Sb spectra.

The isomer shift in ^{121}Sb is almost entirely dependent upon the occupation of the $5s$ and $5p$ atomic orbitals as the filled $4d$ orbitals will be little affected by the bonding. Ruby *et al.* (22) have calculated values of $\psi^2(0)/a_0^3$ for antimony in various electronic configurations using Hartree-Fock self-consistent-field atomic wave functions. Their results are given in Figure 6.1 along with a scale of isomer shifts. It is the matching of the isomer shift scale with that of the electron density at the nucleus that is required before use of such a diagram can be made in interpreting spectra. The main failing of the diagram is that atomic wave functions were used in the computation of $\psi^2(0)/a_0^3$ whereas

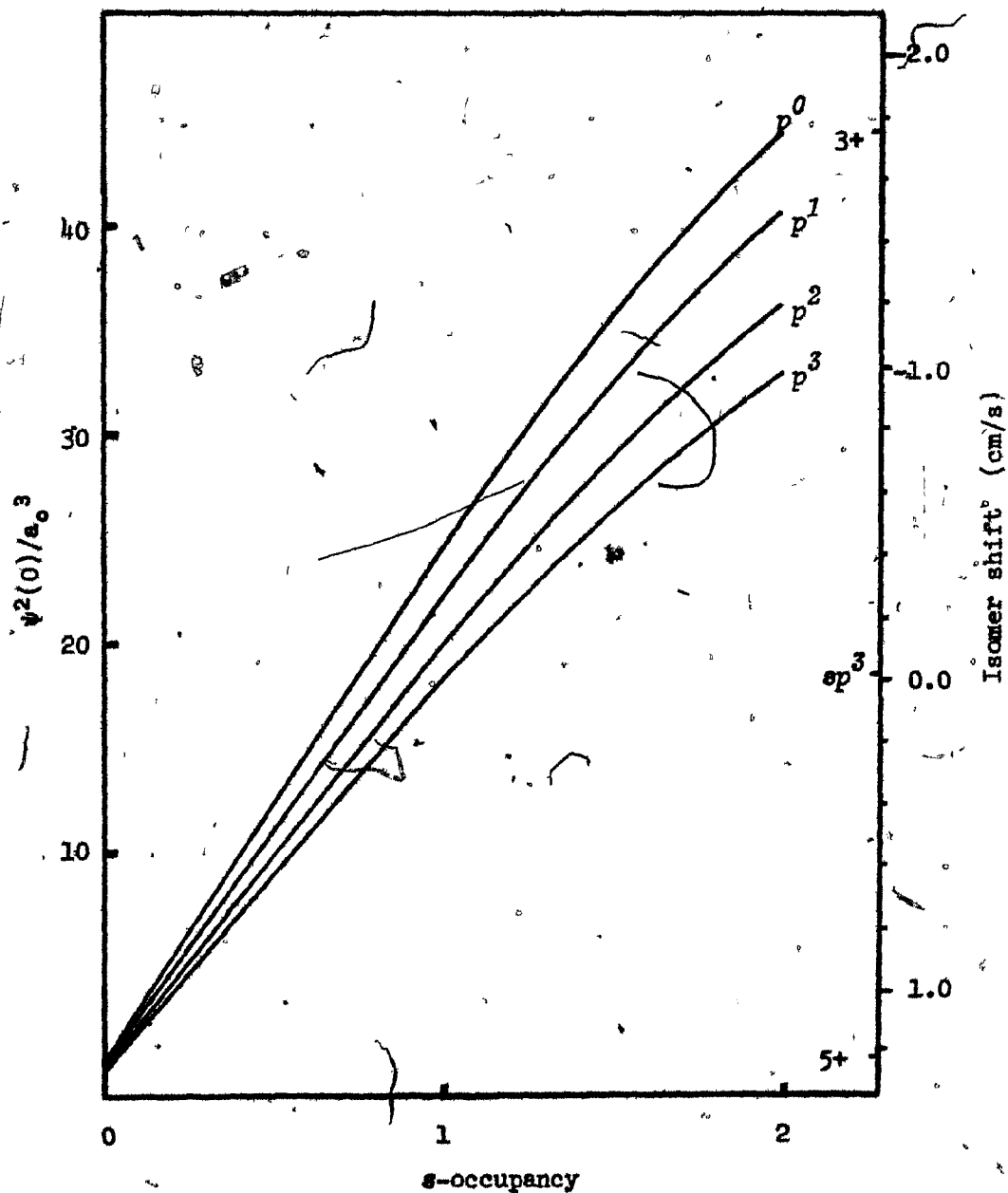


Figure 6.1. Correlation between ^{121}Sb isomer shift and electronic configuration.

the Mössbauer effect results are always concerned with the antimony atom in a *bonding* situation. Such computations are, however, extremely useful in predicting trends to be expected from various bonding models. In order to match the computations to isomer shifts at least two reference points are required at which both an isomer shift value and a value for $\psi^2(0)/a_0^3$ are well established. There are three idealised reference points for antimony; Sb^{3+} , Sb^{5+} and covalent Sb ($5s^1 5p^3$). If these points are to be used either compounds must be found in which antimony is in these states, or some other way must be found to assign isomer shifts to them.

The compound InSb is usually assumed to have Sb in an sp^3 hybridised state as a consequence of its tetrahedral structure. Kjekshus has recently questioned this assumption (59) on the basis that the In-Sb bonds will have some ionic character. He suggests the use of an isomer shift value obtained by extrapolating the shifts of the isostructural series AlSb, GaSb, InSb to zero band gap. This procedure gives an isomer shift of -0.2 ± 0.1 mm/s for a hypothetical compound in which no bond polarisation occurs. The other required reference point was taken by Ruby *et al.* (22) as Sb^{5+} ($5s^0 5p^0$), the isomer shift being derived by comparison with a scale for ^{119}Sn due to Lees and Flinn (60). This isomer shift value of 12.3 mm/s relative to InSb is the same as that of KSbF_6 (22) which has the highest isomer shift yet reported for an antimony compound. It is doubtful, however, that KSbF_6 contains antimony in a $5s^0 5p^0$ state as this would imply no quadrupole effect from the bonding orbitals, whereas a significant quadrupole effect has been observed for

KSbF_6 ($e^2Qq = 8.0 \text{ mm/s}$ (22) and 3.1 mm/s (61)) which would not be expected from ionic effects. This leads to the conclusion that the antimony is in a $5s^0 5p^n$ state which gives rise to the quadrupole effects, although, as may be seen from Figure 6.1, the addition of p electrons would have little effect on the isomer shift. The use of these two reference points and the $\psi^2(0)/a_0^3$ scale gives an isomer shift value of $\sim -18.1 \text{ mm/s}$ for Sb^{3+} , whereas the lowest reported value so far is -11.7 mm/s for both $\text{Co}(\text{NH}_3)_6\text{SbCl}_6$ and $\text{Co}(\text{NH}_3)_6\text{SbBr}_6$ (62). Again it is almost certain that occupancy of the p orbitals is occurring and as may be seen this can cause a significant increase in isomer shift in this case. Thus by the use of Figure 6.1 isomer shifts can be interpreted in terms of a range of possible electronic configurations and the significance of isomer shift variations is more easily assessed.

In view of the ease of determination of the sign of e^2Qq for antimony spectra it is worthwhile considering the implications of this information, especially for the case of a ^{121}Sb atom at a site of symmetry C_{3v} tetrahedrally coordinated by three metals and a non-metal. When the EFG tensor is diagonalised V_{zz} will lie along the major (C_3) axis of symmetry, as this is a threefold axis $V_{xx} = V_{yy}$ and the asymmetry parameter η will be zero. The value of V_{zz} is given by the sum over all the bonding electrons

$$V_{zz} = -|e|\sum (3\cos^2\theta_i - 1)\langle r_i^{-3} \rangle \quad 6.1$$

as it is characteristic of both ^{121}Sb and the nature of the investigated compounds that the lattice makes very little contribution to the quadrupole splitting. If the antimony were at a site of symmetry T_d such

as occurs in InSb then all four bonds, and hence $\langle r_1^{-3} \rangle$'s, would be equivalent and the sum of the geometric terms $(3\cos^2\theta_1 - 1)$ would be zero. In the case of C_{3v} symmetry found in the pyrites, only three of the bonds are equivalent, and as tetrahedral angles are not required by the structure a contribution due to the variation from tetrahedral geometry occurs. The situation is further complicated in the marcasites where the site symmetry is even lower.

As the geometric term is negative for $54^\circ 40' < \theta < 125^\circ 20'$ it can be seen from 6.1 that a negative field gradient corresponds to a concentration of charge along the major axis, and as Q for ^{121}Sb is negative, this will be observed as a positive $e^2 Qq$.

3. *Experimental and Results*

The compounds investigated were all prepared and characterised as described in Chapter 2, x-ray patterns being compared with those previously reported (63,64,65,66,67). The ^{121}Sb Mössbauer spectra were all run at the University of Aberdeen using a cryostat in which both the source and absorber were at 77°K . The source was connected via a vertical stainless steel shaft to the transducer. The cooling of the source was necessary as the recoil free fraction of ^{121}Sb γ -rays is too low at room temperature to obtain reasonable spectra. Experiments were run for about three days, in which period 60,000 to 80,000 counts per channel were recorded. The low counting rate was a result of the relatively weak, 0.5 millicurie, ^{121}Sb source used. This is a typical strength for ^{121}Sb sources and the low counting rate is one of the major drawbacks of this

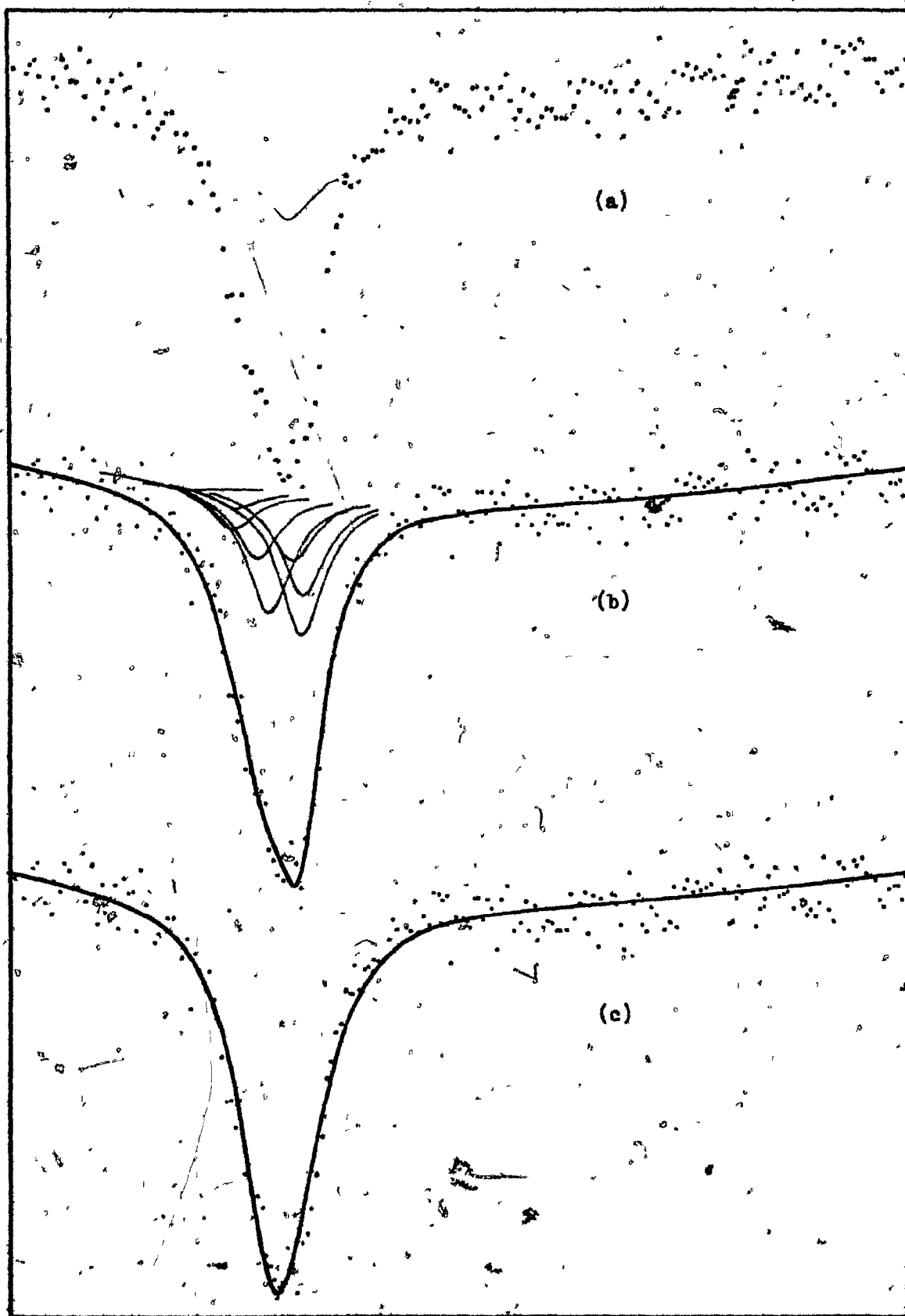


Figure 6.2: ^{121}Sb Mössbauer spectrum of FeSb_2 showing (a) raw spectrum, (b) fit with e^2Qq positive and (c) fit with e^2Qq negative.

Mössbauer isotope. The spectra obtained from these experiments gave an absorption of about 10%, the samples containing about 10 mg of natural antimony per square centimeter. Figure 6.2(a) shows a typical spectrum. The spectra were all fitted to an eight line quadrupole model using both negative and positive starting approximations for e^2Qq . Although, the fitting program converged in both cases, a comparison of χ^2 values allowed an allocation of sign for most samples, as did a visual comparison of fits such as those shown in Figure 6.2(b) and (c). The parameters obtained from these fits are listed in Table 6.1[†]. The linewidths obtained from all the spectra except CrSb_2 compared well with that obtained from a single line fit of InSb , in which the antimony is in a site of cubic symmetry and hence zero EFG. CrSb_2 orders antiferromagnetically at 273°K (68) so a small magnetic field can be expected at the antimony site which will give rise to a line broadening effect. Analogy with antiferromagnetic MnTe_2 indicates that the magnitude of the field will be ≤ 50 kOe (9). As the magnetic spectrum from the $7/2 \rightarrow 5/2$ ^{121}Sb

[†]A preliminary communication of these results was included in a paper presented to a meeting of the Chemical Society Mössbauer Discussion Group at Exeter in March 1972. At this time it was discovered that Donaldson, Kjekshus, Nicholson and Tricker had also investigated these compounds, and they kindly supplied a preprint of a paper they had submitted for publication (69). A list of their results, mostly at 4.2°K, is included in Table 6.2.

Table 6.1: ^{121}Sb Mössbauer results (source and absorber at 77°K).

Compound	Structure [†]	Isomer Shift [‡] (mm/s)	e^2Qq (mm/s)	Linewidth (mm/s)	χ^2 §
CrSb_2	m	-0.75(5)	12.4(9)	6.0(2)	213/194
$\text{Cr}_{0.5}\text{Fe}_{0.5}\text{Sb}_2$	m	-1.24(8)	13.8(9)	3.1(2)	199/194
FeSb_2	m	-1.09(5)	11.6(8)	3.0(2)	187/194
RuSb_2	m	-0.57(4)	12.9(6)	3.0(2)	204/194
OsSb_2	m	-0.12(3)	12.6(4)	3.2(3)	211/194
CoSb_2	a	-0.99(4)	8.6(8)	3.3(2)	195/194
RhSb_2	a	-0.79(4)	8.4(9)	3.1(2)	208/194
IrSb_2	a	-0.18(3)	8.4(8)	3.2(2)	208/194
NiSb_2	m	-1.43(4)	4.9(1.5) [#]	3.2(2)	175/194
PdSb_2	p	-1.45(2)	-	3.1(1)	188/195
PtSb_2	p	-0.44(2)	-	3.3(2)	227/195
AuSb_2	p	-2.65(4)	-	3.0(1)	228/195
$\text{NiSbS}(\text{natural})^*$	u	-2.58(6)	-15.5(6)	3.2(2)	218/194
$\text{NiSbS}(\text{synthetic})$	u	-2.67(6)	-15.6(6)	2.9(2)	199/194
RhSbS	u	-0.45(10)	-19.8(1.2)	3.2(3)	231/194
IrSbS	u	0.48	-20.4(5)	3.6(2)	202/194
PtSbTe	p/u [‡]	-1.20(6)	7.0(1.5)	3.2(3)	175/194

[†] m marcasite, a arsenopyrite (CoSb_2), p pyrite, u ullmanite.

[‡] Relative to InSb . [§] Quoted as $\chi^2/\text{number of degrees of freedom}$.

[#] Single line fit was equally good but gave an abnormally large linewidth.

* Sample E1912 from Sarrabus, Sardinia. [‡] Ordering cannot be detected by x-rays.

Table 6.2. ^{121}Sb Mössbauer results of Donaldson *et al.* (69).

Compound	Structure [†]	T(°K)	Isomer shift [‡] (mm/s)	e^2Qq [§] (mm/s)
CrSb ₂	m	4.2	-	-
CrSb ₂	m	78	-0.9	11.3
FeSb ₂	m	4.2	-1.5	14.8
FeSb ₂	m	78	-1.5	12.7
CoSb ₂	a	4.2	-1.3	9.3
CoSb ₂	a	78	-0.9	8.5
NiSb ₂	m	4.2	-1.5	5.0
NiSb ₂	m	78	-1.7	8.4
RuSb ₂	m	4.2	-0.8	12.4
RhSb ₂	a	4.2	-0.6	10.2
PdSb ₂ [*]	p	78	-1.7	4.3
OsSb ₂	m	4.2	-0.4	13.1
IrSb ₂	a	4.2	0.0	7.6
PtSb ₂	p	4.2	-0.8	2.7
AuSb ₂	p	4.2	-2.6	3.0

[†] m marcasite, a arsenopyrite, p pyrite.

[‡] Isomer shift relative to InSb at 78°K, probable error ± 0.1 mm/s.

[§] Probable error ± 1 mm/s.

^{*} Quoted from Montgomery and Ruby (75).

Table 6.3. Mössbauer results for the series $\text{PtSb}_{2-x}\text{Sn}_x$

Compound	Structure [†]	Antimony-121 Isomer Shift (mm/s)	χ^2 S	Tin-119 Isomer Shift (mm/s)*	e^2Qq (mm/s)	χ^2
PtSn_2	f	-	-	2.110(12)	-	253/251
$\text{PtSb}_{0.7}\text{Sn}_{1.3}$	m	-0.77(6)	199/195	2.146(6)	1.049(10)	250/250
PtSbSn	m	-0.69(4)	230/195	2.139(7)	1.034(10)	248/250
$\text{PtSb}_{1.3}\text{Sn}_{0.7}$	m	-0.58(5)	224/195	2.116(7)	0.909(12)	274/250
PtSb_2	-p	-0.44(2)	227/195	-	-	-

[†] f flourite, m marcasite, p pyrite.

* Relative to InSb , source and absorber at 77°K.

* Quoted as χ^2 /number of degrees of freedom.

* Relative to BaSnO_3 , source and absorber at room temperature.

transition is somewhat complicated no attempt was made to analyse the CrSb_2 spectrum in detail. No indication of magnetic ordering was observed for the mixed compound $\text{Cr}_{0.5}\text{Fe}_{0.5}\text{Sb}_2$, linewidths obtained being 3.1(2) mm/s compared to 2.8(2) mm/s for InSb and 6.0(2) mm/s for the ordered CrSb_2 .

^{119}Sn spectra were also taken of the compounds in the series $\text{PtSb}_{2-x}\text{Sn}_x$. These spectra were fitted to the two line quadrupole model expected from tin spectra and the results are listed in Table 6.3.

4. Discussion

The compounds investigated in this work were all either metallic conductors or semiconductors with quite small band gap energies. The tetrahedral coordination of the antimony indicates an electronic configuration similar to that of an sp^3 hybrid and such a model agrees well with the observed isomer shifts which are all close to the -0.2 mm/s that would be expected from sp^3 hybridised ^{121}Sb . Figure 6.1 shows that the isomer shift results are consistent with an s occupancy of close to 1, but the p occupancy is virtually undetermined. The relationship of the isomer shift to structural properties is somewhat of a problem with these compounds. It would be expected that the bonding variations at the non-metal site would be reflected in the Sb-Sb distances, but these distances all lie in the range 2.79 - 2.89 Å. In view of the accuracy to which this distance can be determined (see Chapter 4), it is not possible to consider variations within this range as being meaningful. If M-Sb distances are considered the contribution of the metal to this distance

must be evaluated when metals from different periods are used. Donaldson *et al.* (69) correlate structural parameters with isomer shifts using only the compounds CrSb_4 , FeSb_2 and NiSb_2 on the grounds that, although they are restricting themselves to three compounds these all have the same structure and contain metals from the same period. Their conclusions are however suspect for two reasons; firstly, CrSb_2 is ordered anti-ferromagnetically and although an 'acceptable' fit is obtained from a pure quadrupole model the parameters are undoubtedly modified by magnetic effects. Secondly, NiSb_2 is a metallic conductor and as will be seen below, the isomer shift is very sensitive to occupation of the conduction band. An alternative approach is to consider the results as a whole to see if any meaningful trends can be observed. Figure 6.3 shows the isomer shift results for the diantimonides in a diagrammatic form. As can be seen it is possible to split the results into two groups on the basis of conductivity. If the bonding scheme outlined in Chapter 4 is considered, where j is the number of electrons per formula unit in excess of the σ bonding requirements, the criterion for metallic conduction is either $j > 6$, or that the conduction band energy overlaps that of the metal t_{2g} bands. As the conduction band is formed from the ' sp^3 ' antimony orbitals occupation of it has a direct effect on $\psi^2(0)/a_0^3$, causing a decrease in the isomer shift ($\delta R/R$ being negative). Of the $j = 6$ compounds this effect is most pronounced in PdSb_2 which might be expected to have an isomer shift of about -0.6 mm/s if it were a semiconductor. The low value of isomer shift for PtSb_2 relative to IrSb_2 and OsSb_2 is probably due to its small band gap energy, 0.07 eV, giving

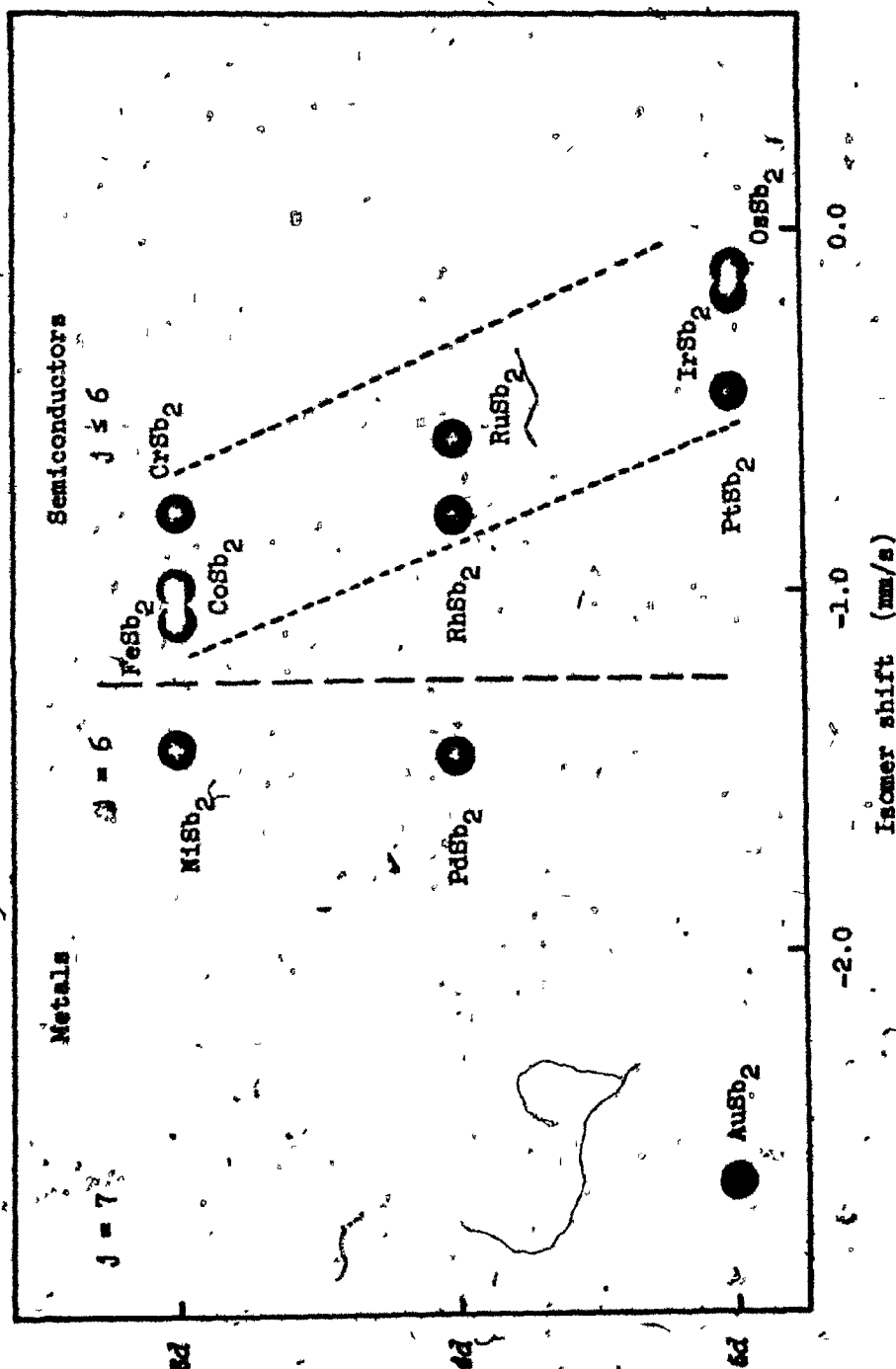


Figure 6.3. Diagrammatic representation of the isomer shift results for the diantimonides.

rise to thermal population of the conduction band. The effect of population of the conduction band is most apparent in compounds such as AuSb_2 where $j > 6$. In this case $j = 7$, corresponding to a population of one electron per formula unit, and an isomer shift of -2.65 mm/s is observed. The ternary compound NiSbS also has $j = 7$, although the extra electron in this case comes from the non-metal pair, resulting in an isomer shift of -2.6 mm/s . There is a trend within the semiconducting compounds for the isomer shifts to increase as the principal quantum number of the metal increases, the shifts for the $5d$ compounds being close to the value expected for sp^3 antimony. This trend is not unusual for antimonides as antimony belongs to the same period as the $5d$ transition metals.

It will be noted from Table 6.1 that the range of e^2Qq values observed in this work is large. It is reasonable to assume that the electric field gradient at the ^{121}Sb nucleus is entirely due to the local bonding environment. The causes of the EFG can be considered as twofold: i) the geometric distribution of the bonds and ii) the electron distribution within the bonds. At this point two assumptions made in the following argument should be mentioned, they are:

i) Only in pyrite and ullmanite does the EFG have an asymmetry parameter η of zero, whereas η has been neglected in the fitting of all the spectra. The results obtained are, however, considered valid as η is not expected to be large and except in extreme cases the inclusion of η as a parameter in the fitting program would have no significant effect on the values of e^2Qq and isomer shift obtained.

ii) The CoSb_2 structure type has two crystallographically non-equivalent Sb sites and hence two Mössbauer absorptions are expected from compounds with this structure. The experimental spectra show no evidence of this and when fitted to a single quadrupole model linewidths comparable to those from the pyrites and marcasites are obtained. It is thus concluded that the structural difference in the sites is such that it is not observable by Mössbauer spectroscopy and in the rest of this chapter the spectrum is considered, with due care, to be that of a site which is an average of the two non-equivalent sites.

The values of e^2Qq for the diantimonides are all positive so, assuming that V_{zz} lies along the Sb-Sb bond, and using equation 6.1

$$|2\langle r_{\text{Sb-Sb}}^{-3} \rangle| < |\Sigma(3\cos^2\theta_1 - 1)\langle r_{\text{Sb-M}}^{-3} \rangle|. \quad 6.3$$

If the series of compounds CrSb_2 , FeSb_2 , CoSb_2 and NiSb_2 are considered, for which reasonably accurate structural parameters are available (66, 67, 68), a correlation between e^2Qq and the geometric term $\Sigma(\cos^2\theta_1 - 1)$ for the Sb-M bonds exists, as is shown in Figure 6.4. The implications of such a correlation are that it is reasonable to treat the Sb-M bonds in the marcasites and arsenopyrites as being equivalent, as it would otherwise be impossible to separate the geometric term from the $\langle r^{-3} \rangle$ term. The mean value of $\langle r_{\text{Sb-M}}^{-3} \rangle$ must be less than $\langle r_{\text{Sb-Sb}}^{-3} \rangle$ by at least a factor of 1.4, else the observed e^2Qq would be negative. This variation of $\langle r^{-3} \rangle$ can be attributed to two causes; firstly, the character of the Sb-Sb bond could be higher than the Sb-M bonds; and secondly, the Sb-Sb bond is probably highly localized, whereas the Sb-M bond is part of the σ bonding band which would indicate a high degree

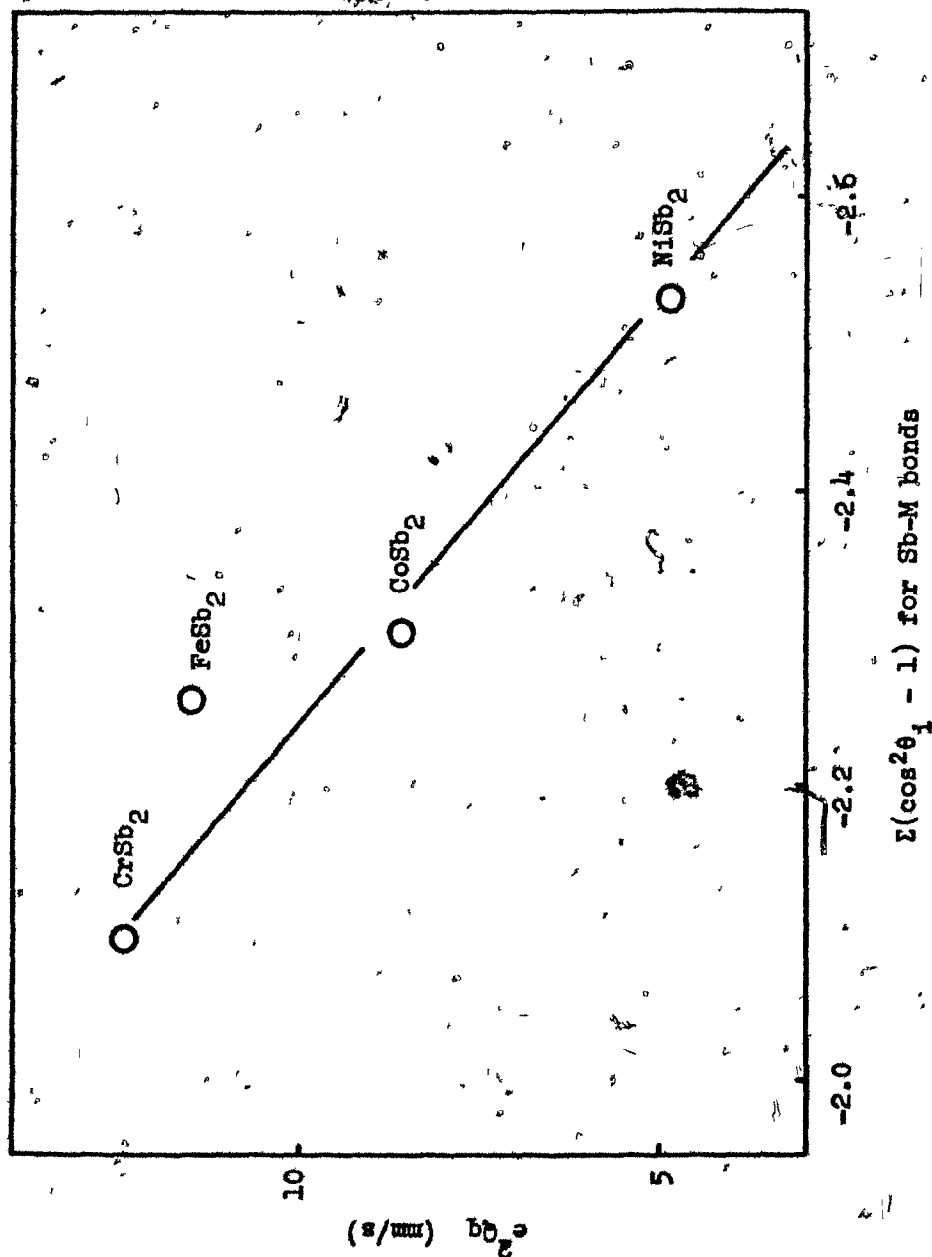


Figure 6.4. Plot of e^2Qq against $\sum(\cos^2\theta_i - 1)$ for Sb-M bonds in the diantimonides.

of delocalisation and hence a low value of $\langle r^{-3} \rangle$.

The ternary compounds that were investigated fall into two categories, the sulpho-antimonides and the tin-antimonides. The compound PtSbTe forms a bridge between these categories in that it is a natural extension of the series $\text{PtSn}_2 \rightarrow \text{PtSb}_2$ as well as being the tellurium analogue of PtSbS . The sulpho-antimonides agree well with the isomer shift scheme proposed for the diantimonides MSbS ($j = 7$) having a similar shift to AuSb_2 and RhSbS and IrSbS ($j = 6$) having shifts corresponding to those expected from semiconductors. The positive isomer shift obtained for IrSbS indicates a possible polarisation of the Sb-S bond resulting in a depopulation of the $\text{Sb } s$ orbital. This not unexpected effect is confirmed by the large negative values of e^2Qq found for these compounds, which, if the Sb-M bonds are similar to those in the diantimonides corresponds to $\langle r_{\text{Sb-S}}^{-3} \rangle$ being much smaller than $\langle r_{\text{Sb-Sb}}^{-3} \rangle$. The structures of IrSbS and RhSbS have not been as well established as that of ullmanite. The large negative value of e^2Qq that arises from these compounds strongly points to the existence of Sb-S pairs which are consistent with, but not necessarily proof of, the ullmanite structure. A further discussion of this point is given in the appendix. A polarisation effect also explains why PtSbTe does not have the large negative e^2Qq which might have been expected from an examination of the sulpho-antimonides, the electronegativity of tellurium being close to that of its neighbour antimony.

The series of compounds $\text{PtSb}_{2-x}\text{Sn}_x$ occurs with the marcasite structure in the range $0.7 \leq x \leq 1.3$ (58). Such a homogeneity range

could indicate a random arrangement of tin and antimony; however, no evidence is available either from x-ray or Mössbauer experiments to support this supposition. The isomer shift trend within this series is in general that as one increases the number of electrons in the compound the value of $\psi^2(0)/a_0^3$ decreases. This indicates that the electrons are going into the metal t_{2g} orbitals, as would be expected, and that population of these orbitals affects the M-Sb bonds in such a way as to cause a small decrease in $\psi^2(0)/a_0^3$ at the antimony and tin sites. The isomer shift of the ^{119}Sn spectrum for PtSn_2 does not agree with the general trend, but this is not unexpected as this compound has the fluorite structure in which non-metal pairs do not exist. As antimony and tin sites can be expected to be similar it is interesting to note that, whereas a well resolvable splitting is obtained from the tin spectra, no significant effect is obtained from the antimony.

The low ^{121}Sb isomer shift value obtained for PtSbTe is an expected result as this compound is a metallic conductor. The shift is perhaps not quite as low as might be predicted from an examination of other metallic compounds.

Chapter 7.

CONCLUSIONS

It is now possible to re-examine the bonding scheme outlined in Chapter 4 in the light of the results described in Chapters 5 and 6. As the scheme is quite a general one this examination should be approached with two questions in mind; firstly, are the results of this work consistent with the scheme as outlined and secondly, what details can be added to the scheme.

The detailed interpretations of the results given in Chapters 5 and 6 indicate that the results obtained in this work can be interpreted within the scheme. In some cases, however, it is noticeable that the energy scale in Figure 4.6 is arbitrary and overlap of the ' t_{2g} ' orbitals and the conduction band can occur such as in NiSb_2 and PdSb_2 . This scheme has its origins based on the interpretation of a number of physical properties which have been measured in some detail for these compounds. As such it is to some extent a formalised scheme the details of which have either been neglected or established by somewhat intuitive arguments. The Mössbauer effect yields results in the form of isomer shifts and quadrupole splittings which are directly related to the electron distribution within the compound being investigated. It would therefore be reasonable to expect these results to reflect at first hand details of the bonding.

Perhaps the most interesting feature of the proposed scheme is the allocation of the bonding electrons from both the metals and the non-metals first to the σ_{M-X} and σ_{X-X} orbitals and then the j excess electrons to the metal t_{2g} orbitals and the σ_{M-X}^* conduction band. As in general the energy of the t_{2g} orbitals is less than that of the conduction band the effect of varying j (for $j \leq 6$) is to vary the surroundings of the metal and leave the non-metal unchanged. This is the effect regardless of whether the variation of j is brought about by a change of metal or non-metal. This feature is confirmed by the present results in two ways; firstly, the variation of j for $j \leq 6$ gives rise to isomer shift changes at the metal site typical of d orbital shielding, and quadrupole splitting changes can be traced to variations in t_{2g} occupancy. Thus variation of j is established to cause a variation in the metal electronic configuration. Secondly, the minimal variation of isomer shifts of both ^{121}Sb and ^{119}Sn at the non-metal sites in the series $\text{PtSb}_{2-x}\text{Sn}_x$ indicates that the variation of j by changing the Sb:Sn ratio has little effect on the bonding at the non-metal site. That the metal t_{2g} orbitals are in fact non-bonding also follows from the above results and this is in agreement with the conclusions reached by Kjekshus and Nicholson (41) on the basis of structural parameters. The narrow band or localised nature of these orbitals is already well established as partial filling does not lead to metallic conduction.

The change in ^{121}Sb isomer shift between metallic conductors and semiconductors is evidence that the conduction band is in fact the σ_{M-X}^* band which is formed from the metal bonding orbitals and s and p

non-metal orbitals. The range of isomer shifts encountered in this work is indicative of an electronic configuration close to sp^3 hybridisation, which is also suggested by the tetrahedral coordination of the non-metals. The quadrupole parameters for the diantimonides give a further insight into the bonding in that for the correlation between e^2Qq and crystal structure to be considered reasonable $\langle r_{Sb-M}^{-3} \rangle$ must be significantly less than $\langle r_{Sb-Sb}^{-3} \rangle$. It is immediately apparent that this effect is the opposite to that which would be expected if some degree of ionic bonding were introduced, and Mallick and Emtage (70) when discussing NMR measurements on $PtSb_2$ reach the conclusion that $Pt^{2-}(Sb^+)_2$ is more probable than $Pt^{4+}(Sb^{2-})_2$. A more realistic way of formulating this is that the Sb-M bonds forming a band are probably quite delocalised with a consequent low value of $\langle r_{Sb-M}^{-3} \rangle$ compared to the Sb-Sb bond which is a localised one. A case of bond polarisation was observed in this work when Sb-S pairs were found to result in large negative values for e^2Qq . A similar effect has been observed in a series of organo-antimony compounds (71), sp^3 antimony in Ph_3Sb has an e^2Qq of $+17.5(1)$ mm/s, a lone pair being aligned in the same direction as V_{zz} . The trigonal bipyramidal Ph_3SbX_2 ($X = F, Cl, Br, I$) compounds have V_{zz} along the X-Sb-X direction and the high electronegativity of X causes a polarisation of the Sb-X bonds and a large negative value for e^2Qq of about -20 mm/s.

In view of the overlap of this work and that of Donaldson *et al.* (69) it is of interest to compare the two sets of conclusions. There are two major differences in interpretation concerning the isomer shifts

of metallic conductors and the correlation of e^2Qq with structural properties. To a large extent the present interpretation is a result of the comparison of results for both binary and ternary compounds whereas Donaldson *et al.* confined their investigations to the binary MSb₂ compounds. The difference in interpretation of isomer shifts has been discussed at some length in Chapter 6, while the effect of populating the conduction band is confirmed by the results for NiSbS and PtSbTe it is not immediately clear why Donaldson *et al.* do not discuss the low isomer shift value of AuSb₂. Donaldson *et al.* do not choose to pursue the analysis of the quadrupole effects in these compounds, concluding only that the $5p_x$ population relative to that of the $5p_x$ and $5p_y$ orbitals is more localised on the antimony. It has been found in the present work that a correlation between structure and e^2Qq exists and this conclusion can be expanded in terms of the delocalised nature of the σ_{Sb-M} band. As a result of looking at the ternary compounds to examine the effect of the fourth non-metal nearest neighbour it has been found possible to confirm the existence of Sb-S pairs in IrSbS and RhSbS and to provide direct experimental evidence that the metal t_{2g} orbitals are not involved in π -back-bonding.

In addition to providing details of the bonding in pyrites, marcasites and arsenopyrites the present work has shed further light on the magnetic structure of CoS₂. Within the group of structures investigated CoS₂ is the only binary compound to order ferromagnetically. The low value of saturation magnetisation and difficulty in determining the magnetic structure as a consequence of the high space group symmetry

has lead to much speculation on this topic. Whilst it must be admitted that the circumstances were to some degree fortuitous, it was found possible by performing simulations of the Mössbauer spectra for various possible magnetic structures to rule out entirely the possibility of a collinear alignment of atomic moments. The simulations gave good agreement with the experimental spectra for a helical arrangement of moments, a structure which agrees well with other experimental evidence and which is similar to the antiferromagnetic ordering found in the isostructural MnTe_2 .

In the preceding chapters it has been shown that the application of the Mössbauer effect has allowed information to be obtained which is not available from the usual crystallographic techniques. It should be emphasised, however, that the analysis of Mössbauer spectra generally requires an intimate knowledge of the structural properties of the compound in question. In most cases Mössbauer spectroscopy should be considered as a method of augmenting rather than replacing an x-ray investigation of a compound.

Chapter 8.

COMPUTATION OF THE NUMBER OF DISTINCT ISOMERS OBTAINABLE BY
MONODENTATE SUBSTITUTION OF POLYHEDRA1. *Introduction*

It is fast becoming apparent that in order to obtain the maximum amount of information from Mössbauer spectra a rigorous analysis of the available data must be made. Many experiments involve alloys and compounds where a disordered situation obtains and in order to understand the spectra each possible environment of the Mössbauer atom must be considered. The purpose of this chapter is to describe the computation of a set of tables which may be used to find out the number of possible environments such a Mössbauer atom may have. Such a Mössbauer problem can be approached in two ways, an exact enumeration of all the possible sites or a computer simulation using Monte Carlo methods. The tables computed as part of this work will be of use as a check in the exact approach. They will also be of use in evaluating which approach to take, as simulation is not always the quickest method if it requires a large amount of programming or computer time.

The computations described in this chapter enabled the production of a set of tables for determining the number of distinct positional isomers that may be obtained by monodentate substitution of convex polyhedra. In the case of the Mössbauer problem outlined above the polyhedron in question is the coordination polyhedron of the

Mössbauer atom. The numbers of configurations are of course well known for small polyhedra of high symmetry, however, the cases of a large number of vertices and more than two substituents have not until now been treated. A knowledge of the number of distinct configurations is in these cases a prerequisite for the enumeration of possible isomers.

The primary concern of this work was the computation of the tables which due to bulk and the exact nature of the results required the use of some unconventional programming techniques. As it is intended to submit the rather extensive tables for publication only an example of them will be reproduced in this chapter.

2. Polyhedra

A listing of the polyhedra for which tables have been compiled is given in Table 8.1. This list has been made as extensive as possible but as the number of vertices V increases such a task becomes unwieldy. The polyhedra included for the higher values of V have been selected for their chemical interest, and include polyhedra common in first, second and even third nearest neighbours. Just as the number of polyhedra increases with V so does the number of partitions or possible compositions. It has been necessary for practical reasons of space and time to restrict the tabulations; it is also dubious whether an unrestricted tabulation of all the partitions for large values of V would be of potential use. Tabulation has been unrestricted for $V \leq 8$, partitions up to five substituents have been tabulated for $V = 9$, four substituents for $10 \leq V \leq 12$, three for $13 \leq V \leq 16$ and for $V \geq 17$ only binary partitions

Table 8.1. List of polyhedra

No. ¹	F	E	Polyhedron	P.G. ²	Type ³
3-1	2	3	Triangle	D_{3h}	Po
4-1	2	4	Square	D_{4h}	Po
4-2	4	6	Tetrahedron	T_d	PL, Δ
4-2(C_{3v})	4	6	Trigonal pyramid	C_{3v}	Py
4-2(D_{2d})	4	6	Bisphenoid	D_{2d}	Apr
5-1	2	5	Pentagon	D_{5h}	Po
5-2	5	8	Square pyramid	C_{4v}	Py
5-3	6	9	Trigonal bipyramid	D_{3h}	Bpy, Δ
5-3(C_{3v})	6	9	Tetrahedron + 1	C_{3v}	
6-1	2	6	Hexagon	D_{6h}	Po
6-2	5	9	Trigonal prism	D_{3h}	Pr
6-3	6	10	Pentagonal pyramid	C_{5v}	Py
6-4	8	12	Octahedron	O_h	PL, Δ
6-4(D_{3d})	8	12	Trigonal antiprism	D_{3d}	Apr
6-4(D_{4h})	8	12	Tetragonal bipyramid	D_{4h}	Bpy
6-4(D_{2d})	8	12	Tetragonal scalenohedron	D_{2d}	
7-1	2	7	Heptagon	D_{7h}	Po
7-2	7	12	Hexagonal pyramid	C_{6v}	Py
7-2(C_{3v})	7	12	Singly-capped trigonal prism	C_{3v}	

Table 8.1. (Continued)

7-2(C_{3v})	10	15	Tetrahedron + 3 = octahedron + 1 = singly-capped trigonal antiprism	C_{3v}	
7-2(C_{2v})	8	13	Trigonal prism + 1	C_{2v}	
7-3	10	15	Pentagonal bipyramid	D_{5h}	Bpy, Δ
8-1	2	8	Octagon	D_{8h}	Po
8-1(D_{4d})	10	16	Square antiprism	D_{4d}	Apr
8-1(C_{2v})	11	17	Trigonal prism + 2	C_{2v}	
8-2	6	12	Cube	O_h	Pl
8-2(T_d)	12	18	Tristetrahedron	T_d	Ca
8-2(D_{3d})	6	12	Rhombohedral=trigonal streptohedron	D_{3d}	Ca
8-2(D_{4h})	6	12	Tetragonal prism	D_{4h}	Pr
8-2(D_{2d})	12	18	Dodecadeltahedron	D_{2d}	Δ
8-2(D_{2h})	8	14		D_{2h}	
8-3	8	14	Heptagonal pyramid	C_{7v}	Py
8-4	8	14		D_{2d}	
8-5	9	15	Bicapped trigonal prism	D_{3h}	
8-5(C_s)	10	16	Singly-capped trigonal prism + 1	C_s	
8-6	12	18	Hexagonal bipyramid	D_{6h}	Bpy
8-6(D_{3d})	12	18	Hexagonal(ditrigonal) scalenohedron	D_{3d}	
9-1	2	9	Nonagon	D_{9h}	Po
9-2	9	16	Octagonal pyramid	C_{8v}	Py

Table 8.1: (Continued)

9-2(C_{4v})	13	20	Singly-capped square antiprism	C_{4v}	
9-3	9	16	Singly capped cube	C_{4v}	
9-4	12	19	Bicapped trigonal prism + 1	C_{2v}	
9-5	14	21	Tetrakaidecadeltahedron	D_{3h}	Δ
9-5(D_{3h})	8	15		D_{3h}	
9-5(D_{3h})	11	18		D_{3h}	
9-5(D_{3h})	14	21	Trigonal prism + 3 (faces not all equilateral)	D_{3h}	
9-5(C_{3v})	14	21	Octahedron + 3 (sym.)	C_{3v}	
9-5(C_3)	13	20	Singly-capped trigonal prism + 2	C_3	
9-6	14	21	Heptagonal bipyramid	D_{7h}	Bpy
10-1	2	10	Decagon	D_{10h}	Po
10-2	7	15	Pentagonal prism	D_{5h}	Pr
10-3	10	18	Nonagonal pyramid	C_{9v}	Py
10-4	12	20	Pentagonal antiprism	D_{5d}	Apr
10-5	12	20	Bicapped cube	D_{4h}	
10-6	15	23	Bicapped trigonal prism + 2	C_{2v}	
10-7	16	24	Octagonal bipyramid	D_{8h}	Bpy
10-7(D_{4d})	8	16	"Tetragonal" streptohedron	D_{4d}	Ca
10-8	16	24	Singly-capped trigonal prism + 3	C_{3v}	
10-9	16	24	Hexakaidecadeltahedron	D_{4d}	Δ
10-10	16	24	Bicapped square antiprism (faces not all equilateral)	D_{4d}	

Table 8.1. (Continued)

11-1	2	11	Hendecagon	D_{11h}	Po
11-2	11	20	Decagonal pyramid	C_{10v}	Py
11-2(C_{5v})	16	25	Icosahedron - 1 = singly-capped pentagonal antiprism	C_{5v}	
11-3	15	24	Cube + 3 (equat.)	C_{2v}	
11-4	18	27	Nonagonal bipyramid	D_{9h}	Bpy
11-5	18	27	Bicapped tetrakaidecadeltahedron	D_{3h}	
11-5(C_{3v})	15	24	Cube + 3 (vicinal)	C_{3v}	
11-5(C_{2v})	18	27	" $B_9C_2H_{11}$ " skeleton	C_{2v}	
11-6	12	21		C_{2v}	
12-1	2	12	Dodecagon	D_{12h}	Po
12-2	8	18	Truncated tetrahedron	T_d	Ar
12-3	8	18	Hexagonal prism	D_{6h}	Pr
12-4	12	22	Hendecagonal pyramid	C_{11v}	Py
12-5	14	24	Cuboctahedron	O_h	Ar
12-6	14	24	Hexagonal antiprism	D_{6d}	Apr
12-7	18	28	Cube + 4 (equatorial)	D_{4h}	
12-8	18	28	Cube + 4 (vicinal)	C_{2v}	
12-9	20	30	Icosahedron	I_h	PL, Δ
12-9(D_{5d})			Bicapped pentagonal antiprism	D_{5d}	
12-10	20	30	Decagonal bipyramid	D_{10h}	Bpy
12-11	8	18	Basally truncated rhombohedron	D_{3d}	
12-12	10	20	Basally truncated tetragonal bipyramid	D_{4h}	

Table 8.1. (Continued)

12-13	12	22		D_{2d}	
12-14	12	22		D_{2h}	
12-15	15	25	Bicapped pentagonal prism	D_{5h}	
12-16	16	26		D_{2d}	
13-1	2	13	Tridecagon	D_{13h}	Po
13-2	13	24	Dodecagonal pyramid	C_{12v}	Py
13-3	13	24	Singly-capped hexagonal prism	C_{6v}	
13-4	21	32	Cube + 5	C_{4v}	
13-5	22	33	Hendecagonal bipyramid	D_{11h}	Bpy
14-1	2	14	Tetradecagon	D_{14h}	Po
14-2	9	21	Heptagonal prism	D_{7h}	Pr
14-3	24	36	Tetrahexahedron	O_h	Ca
14-3(T_d)	24	36	Hextetrahedron	T_d	
14-3'	24	36	Trisoctahedron	O_h	Ca
14-3''	12	24	Rhombic dodecahedron	O_h	Ca
14-3'''(T_d)	12	24	Deltahedron	T_d	
14-4	14	26	Tridecagonal pyramid	C_{13v}	Py
14-5	18	30	Bicapped hexagonal prism	D_{6h}	
14-6	24	36	Dodecagonal bipyramid	D_{12h}	Bpy
14-7	24	36	Bicapped hexagonal antiprism	D_{6h}	Ka
14-8	24	36	Bicapped icosahedron	D_{3d}	
14-9	18	30	Heptagonal antiprism	D_{7d}	Apr

Table 8.1. (Continued)

14-10	9	21		D_{3h}	
15-1	2	15	Pentadecagon	D_{15h}	Po
15-2	12	25	Basally truncated pentagonal bipyramid	D_{5h}	
15-3	17	30	Hexagonal prism + 3	D_{3h}	
15-4	26	39	Tridecagonal bipyramid	D_{13h}	Bpy
15-5	26	39	Kasper-15	D_{3h}	Ka
16-1	2	16	Hexadecagon	D_{16h}	Po
16-2	10	24	Octagonal prism	D_{8h}	Er
16-2(D_{4d})	10	24		D_{4d}	
16-3	16	30	Tristetrahedron truncated on all faces	T_d	
16-4	18	32		D_{4d}	
16-5	18	32	Octagonal antiprism	D_{8d}	
16-6	28	42	Kasper-16	C_{3v}	Ka
17-1	2	17	Heptadecagon	D_{17h}	Po
18-1	2	18	Octadecagon	D_{18h}	Po
18-2	11	27	Basally truncated bicapped trigonal prism	D_{3h}	
19-1	2	19	Nonadecagon	D_{19h}	Po

Table 8.1: (Continued)

20-1	12	30	Pentagonal dodecahedron	I_h	Pl
20-1(T_h)	12	30	(Cubic) pentagonal dodecahedron	T_h	
20-1(T)	12	30	Tetartoid	T	
20-1'(T_h)	24	42	Cube + 6x2	T_h	
20-2	12	30	Decagonal prism	D_{10h}	Pr
24-1	14	36	Truncated octahedron	O_h	Ar
24-1(O)	38	60	Snub cube	O	Ar
24-2	14	36	Truncated cube	O_h	Ar
24-3	14	36	Dodecagonal prism	D_{12h}	Pr
24-2'	26	48	Rhombicuboctahedron	O_h	Ar
24-4	26	48	Antirhombicuboctahedron	D_{4d}	
26-1	24	48	(Deltoid) trapezohedron (Trapezoidal icositetrahedron)	O_h	Ca
26-1(T_h)	24	48	Diploid	T_h	
26-1'	48	72	Hexoctahedron	O_h	Ca
30-1	32	60	Icosidodecahedron	I_h	Ar
32-1	30	60	Rhombic triacontahedron	I_h	Ca
32-2	60	90	Trisicosahedron	I_h	Ca
32-3	60	90	Pentakisdodecahedron	I_h	Ca
38-1	24	60	Gyroid (Pentagonal icositetrahedron)	O	Ca
48-1	26	72	Truncated cuboctahedron	O_h	Ar

Table 8.1. (Continued)

60-1	32	90	Truncated dodecahedron	I_h	Ar
60-1(I)	92	150	Snub dodecahedron	I	Ar
60-2	32	90	Truncated icosahedron	I_h	Ar
60-3	62	120	Rhombicosidodecahedron	I_h	Ar
62-1	60	120	(Trapezoidal) hexecontahedron	I_h	Ca
62-2	120	180	Hecatonicosahedron (hexakisicosahedron)	I_h	Ca
92-1	60	150	Pentagonal (pentagonoidal) hexecontahedron	I	Ca
120-1	62	180	Truncated icosidodecahedron	I_h	Ar

¹ Number of the polyhedron, first part is V . $V-2(C_{3v})$ is a polyhedron obtained from, or related to, the polyhedron $V-2$ by lowering the symmetry to C_{3v} .

² Point Group

³ Type of polyhedron: Ar Archimedian polyhedron, Bpy bipyramid, Apr anti-prism, Ca Catalan polyhedron, Po regular polygon, Pl platonic, Pr prism, Py pyramid, Ka Kasper polyhedron.

have been tabulated.

3. Formulation of the Problem

The object of these computations was to derive the numbers of distinct configurations that can be produced by monodentate substitution on convex polyhedra or their isomorphs. This is sometimes referred to as univalent substitution, but this term will not be used as it could lead to ambiguity in a chemical context. The problem is a combinatorial one taking into account reduction by symmetry and may be solved directly by application of Pólya's inventory theorem (72). Stated in a simplified form this is (73): Let S be a finite collection of objects and G a finite group of symmetries for these objects with n operations g_1, g_2, \dots, g_n (one of which must be the identity operator). Let $C(g)$ denote the number of objects in the collection S left fixed by the symmetry g of G . Then the number N of objects in S distinguishable relative to the symmetries of G is given by

$$N = (1/n)\{C(g_1) + C(g_2) + \dots + C(g_n)\}. \quad 8.1$$

To apply this theorem to the present problem one has to consider a particular polyhedron and a particular point group. It is then possible using a simple set of rules to write down the *cycle index* of the configuration group. Once this is done a finite counting series can be substituted into the cycle index and a generating function for N is arrived at. As this generating function is a polynomial it may be expanded as the sum of a series of partitions. Each partition corresponds to a particular combination of monodentate substituents or 'chemical

composition' and the corresponding coefficient is the number of unique arrangements for that partition. It is this breakdown of the results into different compositions that makes these tables chemically useful.

To arrive at the cycle index in a given case it is first necessary to enumerate the individual symmetry elements of the point group being considered and relate these to the polyhedron. An example, a trigonal bipyramid of point group D_{3h} , will be given as the method is explained. The symmetry elements of D_{3h} are as follows:

- I - identity operation (one)
- r_3 - 3-fold rotation axis (one)
- r_2 - 2-fold rotation axis (three)
- s_3 - 3-fold inversion axis (one)
- m_h - horizontal mirror plane (one)
- m_v - vertical mirror plane (three)

The relation of these elements to the trigonal bipyramid is shown in Figure 8.11. The required cycle index is;

$$CI = (1/12)(r_1^5 + 2r_1^2 r_3^1 + 3r_1^1 r_2^2 + 1m_1^3 m_2^1 + 3m_1^3 m_2^1 + 2s_2^1 s_3^1) \quad 8.2$$

The factor 1/12 is the maximum multiplicity of the point group; the individual terms are arrived at by considering each symmetry element of D_{3h} according to the following rules:

- (1) The first term corresponds to the identity operation which is equivalent to a 1-fold rotation axis, r_1 . The exponent 5 refers to the number of vertices that have to be specified before the symmetry operation will generate all the vertices not on the symmetry element.

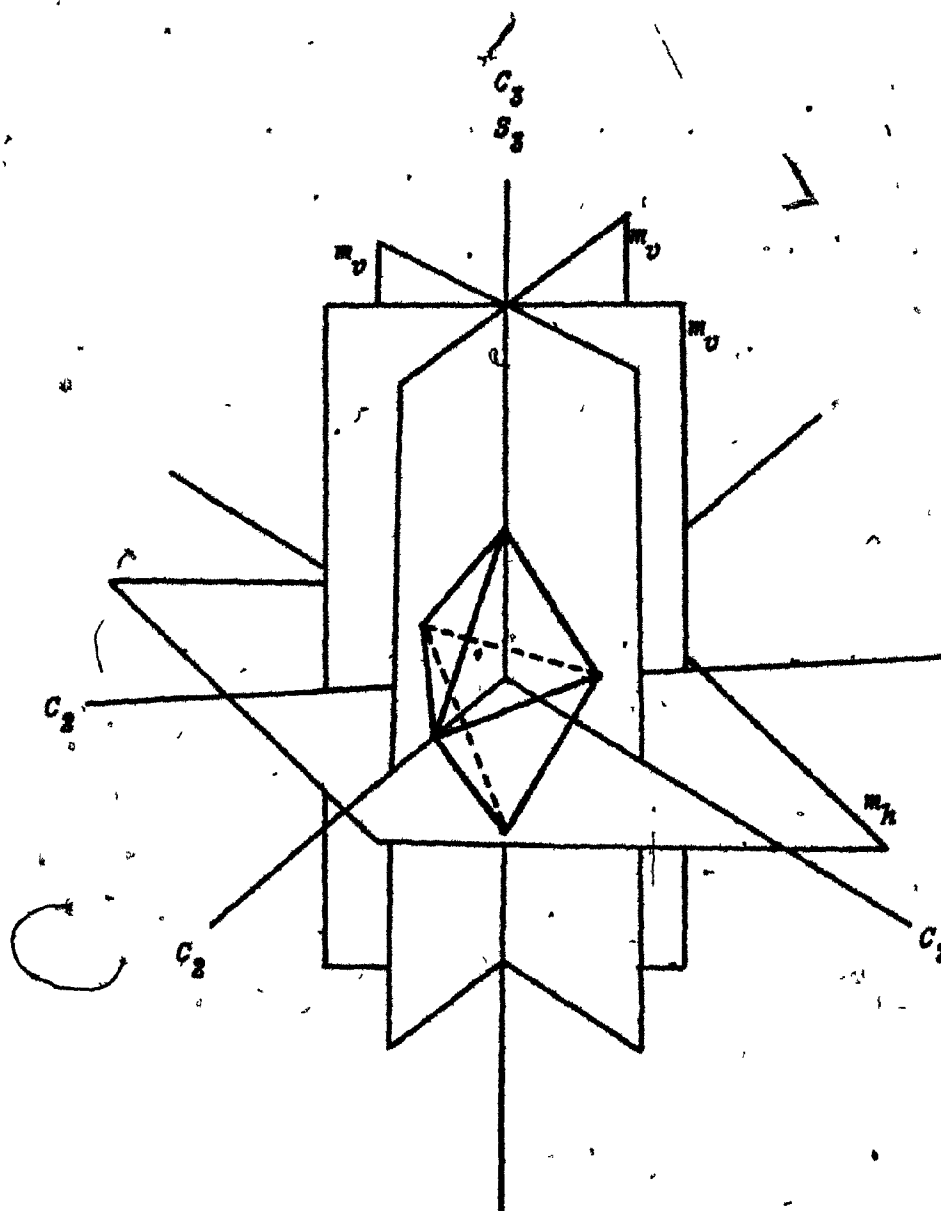


Figure 8.1. The relationship of the symmetry elements of the point group D_{3h} to a trigonal bipyramid.

ii) The remaining terms are compound ones as a result of the symmetry elements passing through one or more vertices. For example the second term corresponds to the 3-fold axis, r_3 , which having one vertex specified will generate the other two not on the axis, hence r_3^1 . The other two vertices each correspond to an identity operation giving $r_3^2 r_3^1$.

iii) The multiplying factor, 2 in the case of the second term, occurs from two considerations. Firstly there is 1 r_3 axis and secondly that axis can generate the vertices in two ways, operating as r_3 or $(r_3)^2 \equiv r_3^{-1}$. The factor 2 is in fact 1 * 2.

iv) The mirror planes are symmetry elements of order two.

v) The 3-fold inversion axis compounds with a 2-fold inversion axis operating on a single vertex.

The figure-counting series is now substituted into the cycle index in the following manner, the specific nature of the symmetry operation is disregarded and a function $(a^1 + b^1 + \dots)^j$ is inserted in place of each element S_i^j . The number of letters, L , in the series corresponds to the number of possible substituents and is therefore equal to or less than V . For the sake of brevity $(L^1)^j$ will be used to denote this function. Following this procedure the generating function for a trigonal bipyramid of symmetry D_{3h} is

$$(1/12)\{(s^1)^5 + 2(s^1)^2(s^3)^1 + 3(s^1)^1(s^2)^2 + 4(s^1)^3(s^2)^1 + 2(s^2)^1(s^3)^1\}. \quad 8.3$$

It is the expansion of generating functions such as these that is the main topic of this chapter.

4. Computational Considerations

The task of expanding a set of generating functions such as 8.3 for each of the polyhedra in Table 8.1 was a major one. Whilst many duplications arose it must be remembered that not only was the full point group of the polyhedron treated but every subgroup of that point group. As a result the computations had to be organised in such a way as to minimise the number of arithmetic operations. This need is immediately apparent if computation times are considered, the multiplication of two elements such as $(g^1)^2(g^2)^3$ where L and V are only eight took as long as three or four minutes on the IBM 360/50 used for the bulk of the calculations.

Another problem associated with the number of polyhedra considered is one of human error. Almost certainly some errors will and did occur in the formulation of the large number of generating functions and the copying of these functions into a machine usable form. Many checks were made, although no perfect way of checking was found, the most effective one being based on the probability of a mistake giving rise to a valid generating function. For the purposes of the check this was construed to mean a function that when expanded gave integer coefficients for all the partitions.

The two largest considerations from a computational aspect were the identification of partitions within the programs in an easily manipulated form, which will be treated in a later section, and the sheer numerical magnitude of the numbers encountered. The necessity for exact results involved the use of fixed point arithmetic for all operations on

the generating functions, in this case it is the size of the number that is determined by machine characteristics as opposed to the exponent in floating point arithmetic. The largest integer that can be stored in the 32 bit word of the IBM 360/50 is 2^{31} (i.e. 2,187,985,248) which is of the same order of magnitude as 12!. As a straight-forward evaluation of terms for V vertices involves the use of $V!$ the expansion of generating functions for polyhedra with more than 12 vertices had to be performed in such a way as to avoid an integer overflow.

Whilst it is possible to program a computer as a black box the efficient use of such a machine requires that the available hardware and software be considered when approaching a problem of any size.

Even the high-level languages such as FORTRAN and PL/1 have restraints imposed on their implementation by the machine configuration. Such a restraint is the maximum available integer size referred to above. This series of computations was performed on two machines, the major portion of the tables was produced using an IBM 360/50 which was replaced by a CDC 6400. As a consequence an auxiliary set of routines was implemented on the CDC 6400 in order to finish off the project.

The IBM system consisted of a central processor and 128K bytes of central memory (IBM measures memory in 8 bit bytes), this being 32K words each 32 bits in length. There were four on-line disc packs. However, as three of these were reserved for the operating system and scratch space, and space on the fourth was at a premium, only program modules were stored on disc. The intermediate data for the computations was stored on magnetic tape and as 360-OS allows allocation of specific

peripheral units this facility was used to minimise operator intervention between programs. The CDC 6400 made available more central memory in the form of 49K words of 60 bit length, and at the time that this work was in progress the available disc space made storage of data on tape unnecessary. The main disadvantage was the lack of a PL/I compiler as all the 360 programs were written in this language.

5. Computational Method

The expansion of functions such as 8.3 can be divided into three steps:

- i) The expansion of single terms of the type $(L^i)^j$.
- ii) The multiplication of two (or occasionally three) such terms.
- iii) Summation of the individual terms of the function with the appropriate factors and dividing through by n .

The approach taken was to perform each of these steps in a different program. In this way use was made of the fact that the generating functions were made up of varied combinations of a limited number of terms and these terms had only to be expanded once. This duplication of terms within the table for a given polyhedron is a consequence of all the possible symmetry groups for the polyhedron being subgroups of the highest symmetry group. Thus only those symmetry elements which occur in the highest point group can appear in the lower groups. The duplication between polyhedra with the same number of vertices is because each element must be a polynomial of order V and the number of ways of forming such polynomials is limited. Steps i) and ii) were used to compile a library

of expanded elements, step *iii*) then selected the appropriate elements, multiplied them by the correct factors and performed a summation. After division by n the results were printed out. A further saving in time and space was made by the observation that many of the terms in the expansions were redundant, e.g. in the expansion of $(a + b + c)^3$ the coefficient of a^2b is the same as those of a^2c , b^2c , b^2a , c^2a and c^2b . In order to make use of this relationship only partitions in which when the letters were arranged alphabetically the powers were in order of magnitude were kept throughout the calculations. For example a^3b^2c would be kept whereas a^3bc^2 and $a^3c^2d (= a^3b^0c^2d)$ would be deleted. As the multiplication process required that all partitions be used as input and the redundant terms be deleted after the product was taken, two versions of step *i*) were used, one as a feeder for step *ii*) and the second to produce expansions of single term elements for the library tape.

The representation of partitions was a major problem and together with the need for good file-management capabilities was the reason for choosing PL/1 as the programming language. The partitions were described within the programs in the form of a collection of storage locations referred to as a *structure* (76) which could be accessed either as a whole or by individual element. The *structures* used consisted of an integer number equated to the coefficient of the partition, a character string which identified the partition, e.g. a^3b^2c would become A03B02C01, and any other variables required by the programs to handle the partitions. The use of *structures* also allowed the expanded terms to be transferred between programs with great ease, as PL/1 allows *structures* to be written

on and read from magnetic tape as a whole.

The problem of number size was overcome by use of the excellent character facilities provided by PL/1. As polyhedra with more than eight vertices were only tabulated for a limited number of substituents coefficients $\geq 12!$ did not occur in the final results; however, their occurrence in intermediate steps had to be allowed for. An example is the expansion of $(a + b)^{24}$, where the coefficient of $a^{12}b^{12}$ is given by $24!/(12! \times 12!)$. The most obvious way of evaluating such an expression is to evaluate $24!$ and $12!$ and perform the appropriate division, but if attempted on a computer this would lead to a fixed point overflow. A possible modification to the method would be to introduce the fact that $24!/12!$ may be written as $24.23.22.....13$ which although reducing the magnitude of the numerator would still lead to an overflow. The solution adopted for these programs was basically the approach one would take if performing the calculation by hand. The numerator and denominator were written out into character strings as

24.23.22.21.20.19.18.17.16.15.14.13

12.11.10.9.8.7.6.5.4.3.2.1

8.4

Then starting at the left-hand side the first number in the denominator was divided into each of the numbers comprising the numerator until an integer quotient was obtained. At this point the appropriate component of the numerator was replaced by the quotient and the denominator component was replaced by 1; should no integer quotient be found no change was made. This process was repeated for each component of the denominator after which the expression was evaluated by dividing the product of the

numerator components by the product of the denominator components. An internal check was made for an integer quotient, the MOD function being a good method of making such a check.

The process of expanding a generating function is probably best described by giving a brief outline of the programs involved.

i) All the single polynomials of the type $(L^1)^j$ are expanded using the appropriate multinomial relationships, e.g. for $(4^2)^5$ the partition $a^4 b^4 c^2$ has a coefficient given by $5! / \{(4/2)! \times (4/2)! \times (2/2)!\}$. Two versions of this program are used. Those single terms which occur in the generating functions as such have only the unique partitions evaluated and each is stored in a sequentially numbered file on a library tape. Those terms which are required for forming products are expanded completely and stored as files on a scratch tape.

ii) Products are formed in a straight-forward manner, the two required files are located and each element of one term is multiplied in turn by each element of the other. This multiplication requires an operation on both the coefficient and the partition identifier parts of the *structure*. The results are checked to see whether the resulting partition is required or not, and if it is, it is stored either in central memory or on disc. The terms of the product are then sorted by adding together the coefficients of like partitions and the resulting expansion is stored on the library tape.

iii) At this point a library tape is available with all the possible component elements of the generating function, each identified by a sequence number. The generating function is specified by giving the file

number of each element, a multiplier for each element and n . The first element specified must be that corresponding to the identity operation, which contains all the possible partitions. This is located and read into central memory. The subsequent files are then located, the coefficient of each partition is multiplied by the specified factor and added to the accumulating total for that partition. After all the files have been processed the total coefficient of each partition is divided by n , a check being performed for an integer result, and the results printed out.

The replacement of the IBM 360/50 by the CDC 6400 occurred after the bulk of the calculations had been performed. The remaining calculations consisted of generating functions that had been missed in the original enumeration. As a result of this and the relatively higher speed of the CDC machine a single program was written in FORTRAN embodying most of the above three programs, but not allowing for the intermediate storage of results. In this program each term of the generating function is expanded as required and used only once.

6. *Uses of the Tables*

The use of these tables is not restricted to the analysis of Mössbauer spectra. They have a potential use in any situation in which an enumeration of distinct isomers is required for a non-trivial polyhedron. Such problems are very real in both organic and inorganic chemistry, one example being the detailed analysis of NMR spectra resulting from boranes. Another example is the calculation of the number of enantiomorphic pairs

Table 8.2. Expansions of the generating functions for a trigonal bipyramid.

Partition	D_{3h}	C_{3h}	D_3	C_{3v}	C_3	C_{2v}	C_2	$C_s(m_2)$
1.1.1.1.1	10	20	20	20	40	30	60	60
2.1.1.1	7	11	10	13	20	18	13	33
2.2.1	5	6	6	8	10	11	16	18
3.1.1	4	5	4	7	8	8	10	13
3.2	3	3	3	4	4	5	6	7
4.1	2	2	2	3	3	3	3	4
5	1	1	1	1	1	1	1	1


that may be expected from a given chemical composition. Table 8.2 is an example of the tables produced in this work, it gives the results obtained for the trigonal bipyramid considered earlier. If one were to consider a molecule that has such a shape, e.g. Ph_3SbCl_2 in which the antimony is surrounded by five ligands at the corners of a trigonal bipyramid, one may well desire to know how many optical isomers one could obtain. The number of distinct isomers for a given composition can be obtained from Table 8.2, if one looks under point group D_{3h} ; however, the existence of mirror planes and a centre of symmetry preclude the distinction between enantiomorphic pairs. This distinction is, however, made if one goes to point group D_3 which is the highest point group without these symmetry elements. Thus as enantiomorphic pairs are counted as one isomer each under D_{3h} and two under D_3 the difference in the number of isomers is the number of such pairs. One finds in this case that Ph_3SbCl_2 has no enantiomorphic pairs, however $\text{SbA}_2\text{B}_2\text{C}$ would have one, SbA_2BCD would have three, and SbABCDE would have ten pairs.

REFERENCES

- 1 K. I. G. Reid Ph.D. Thesis Dalhousie University 1968
- 2 F. Hulliger Structure and Bonding 4 83 (1968)
- 3 J. A. Wilson and A. D. Yoffe Advances in Physics 18 193 (1969)
- 4 G. Brostigen and A. Kjekshus Acta Chem. Scand. 24 2993 (1970)
- 5 N. Elliott J. Chem. Phys. 33 903 (1960)
- 6 J. B. Goodenough J. Solid State Chem. 5 144 (1972)
- 7 T. A. Bither, R. J. Bouchard, W. H. Cloud, P. C. Donohue and
W. J. Siemons Inorg. Chem. 7 2208 (1968)
- 8 P. K. Gallagher, J. B. MacChesney and R. C. Sherwood J. Chem.
Phys. 50 4417 (1969)
- 9 M. Pasternak and A. L. Spijkervet Phys. Rev. 181 574 (1969)
- 10 M. Hansen Constitution of Binary Alloys (McGraw Hill 1958)
- 11 R. P. Elliott Constitution of Binary Alloys, First Supplement
(McGraw Hill 1965)
- 12 F. A. Shunk Constitution of Binary Alloys, Second Supplement
(McGraw Hill 1969)
- 13 J. B. Nelson and D. P. Riley Proc. Phys. Soc. (London) 57
160 (1945)
- 14 P. E. Clark, A. W. Nichol and J. S. Carlow J. Sci. Instrum.
44 1001 (1967)
- 15 R. S. Preston, S. S. Hanna and J. Heberle Phys. Rev. 128
2207 (1962)

- 16 J. S. Carlow Ph. D. Thesis Exeter University 1971
- 17 F. W. D. Woodhams Private communication
- 18 R. L. Mössbauer Z. Physik 151 124 (1958)
- 19 R. L. Mössbauer Naturwiss. 45 538 (1958)
- 20 G. K. Wertheim Mössbauer Effect: Principles and Applications
(Academic Press 1964)
- 21 H. Frauenfelder The Mössbauer Effect (W. A. Benjamin 1962)
- 22 S. L. Ruby, G. M. Klavins, G. B. Beard and R. E. Snyder
Phys. Rev. 159 239 (1967)
- 23 S. L. Ruby and G. E. Shency Phys. Rev. 186 326 (1969)
- 24 L. M. Dautov and V. V. Nemoshkalenko. Proceedings of the
Conference on the Application of the Mössbauer Effect
(Tihany 1969) pp52-60
- 25 R. M. Golding Applied Wave Mechanics (Van Nostrand 1969)
- 26 R. Bersohn J. Chem. Phys. 20 1505 (1952)
- 27 T. C. Wang Phys. Rev. 92 566 (1955)
- 28 J. G. Stevens Ph.D. Thesis North Carolina State University 1969
- 29 J. R. Gabriel Mössbauer Effect Methodology 1 121 (Plenum 1965)
- 30 J. R. Gabriel and S. L. Ruby Nucl. Instr. and Meth. 36 23 (1965)
- 31 J. R. Gabriel and D. Olson Nucl. Instr. and Meth. 70 209 (1969)
- 32 F. Hulliger Nature 198 382 (1963)
- 33 S. Furuseth, K. Selte and A. Kjekshus Acta Chem. Scand. 21
527 (1967)
- 34 P. Bayliss Am. Min. 54 426 (1969)
- 35 Y. Takeuchi Min. J. 2 90 (1997)

- 36 M. J. Buerger Am. Min. 16 361 (1931)
- 37 G. Bronstigen and A. Kjekshus Acta Chem. Scand. 24 1925 (1970)
- 38 F. Hulliger and E. Mooser Prog. Solid State Chem. 2 330 (1965)
- 39 L. Pauling and M. L. Huggins Z. Krist. 87 205 (1934)
- 40 K. Schubert Z. Krist. 108 276 (1956)
- 41 A. Kjekshus and D. G. Nicholson Acta Chem. Scand. 25 866 (1971)
- 42 A. A. Temperly and H. W. Lefevre J. Phys. Chem. Solids 27
85 (1966)
- 43 P. Imbert, A. Gérard and M. Winterberger Comptes Rend. 256
4391 (1963)
- 44 J. Steger and E. Kostiner J. Solid State Chem. 5 131 (1972)
- 45 A. Gérard Colloques Internationaux C. N. R. S. No. 57 55 (1967)
- 46 R. W. Vaughan and H. G. Drickamer J. Chem. Phys. 44 4223 (1967)
- 47 C. B. Barger, M. Avnir and H. G. Drickamer Inorg. Chem.
10 1338 (1971)
- 48 L. Néel and R. Benoit C. R. Acad. Sci. 237 444 (1953)
- 49 R. Benoit J. Chim. Phys. 52 119 (1955)
- 50 R. F. Heidelberg, A. H. Luxem, S. Talhouk and J. J. Banewicz
Inorg. Chem. 5 194 (1966)
- 51 B. Morris, V. Johnson and A. Wold J. Phys. Chem. Solids 28
1564 (1967)
- 52 V. Johnson and A. Wold J. Solid State Chem. 2 209 (1970)
- 53 K. Adachi, K. Sato and M. Takeda J. Phys. Soc. Japan 26 631 (1969)
- 54 S. Miyahara and T. Teranishi J. Appl. Phys. 39 896 (1968)

- 55 H. S. Jarrett, W. H. Cloud, R. J. Bouchard, S. R. Butler
C. G. Frederick and J. L. Gibson Phys. Rev. Lett. 21
617 (1968)
- 56 A. F. Andresen, S. Furuseth and A. Kjekshus Acta Chem. Scand.
21 833 (1967)
- 57 G. Shirane Acta Cryst. 12 282 (1959)
- 58 S. Bhan, T. Gödecke and K. Schubert J. Less Common Metals 19
121 (1969)
- 59 A. Kjekshus and D. G. Nicholson Acta Chem. Scand. 25 3895 (1971)
- 60 J. Lees and P. A. Flinn Phys. Lett. 19 186 (1965)
- 61 T. Birchall and B. DellaValle Can. J. Chem. 49 2808 (1971)
- 62 J. D. Donaldson, M. J. Tricker and B. W. Dale J. C. S. Dalton
893 (1972)
- 63 G. S. Zhdanov and R. N. Kuz'min Soviet Phys.- Crystallography
6 704 (1962)
- 64 S. Furuseth, K. Selte and A. Kjekshus Acta. Chem. Scand. 19
735 (1965)
- 65 T. Rosenqvist Acta Met. 1 761 (1953)
- 66 H. Holseth and A. Kjekshus Acta Chem. Scand. 22 3273 (1968)
- 67 A. Kjekshus Acta Chem. Scand. 25 411 (1971)
- 68 H. Holseth, A. Kjekshus and A. F. Andresen Acta Chem. Scand.
24 3309 (1970)
- 69 J. D. Donaldson, A. Kjekshus, D. G. Nicholson and M. J. Tricker
Acta Chem. Scand. In Press
- 70 G. T. Mallick and P. R. Emtage Phys. Rev. B2 1251 (1970)
- 

- 71 G. G. Long, J. G. Stevens, R. J. Tullbane and L. H. Bowen
J. Amer. Chem. Soc. 92 4230 (1970)
- 72 P. Niggli Grundlagen der Stereochemie (Birkhäuser 1945)
- 73 S. W. Golomb Polycarmines (Schreibner 1965)
- 74 H. Holseth and A. Kjekshus Acta Chem. Scand. 22 3284 (1968)
- 75 H. Montgomery and S. L. Ruby Phys. Rev. B1 4529 (1970)
- 76 S. V. Pollack and T. D. Sterling A Guide to PL/1
(Holt, Rinehart and Winston 1969)

Appendix

STRUCTURE OF THE SULPHO-ANTIMONIDES MSbS (M = Ni, Rh, Ir)

The sulpho-antimonides MSbS all give x-ray powder patterns and have lattice parameters similar to those that would be expected from the pyrite structure. The only difference is the appearance of a couple of x-ray diffraction peaks that could not occur if the space group was that of pyrite ($Pn\bar{3}$). The pyrite structure would for these compounds require that the non-metals be randomly distributed on the 8(c) equipoints. If this does not occur and an ordered distribution of the non-metals exists, a lowering in space group symmetry will result and the diffraction conditions for $Pn\bar{3}$ will no longer apply. Even if the condition is met that the unit-cell remain the same size as the pyrite cell, it is immediately apparent that there are many ways of ordering the non-metals. Each possible structure, however, must belong to a space group that is a subgroup of $Pn\bar{3}$. In view of this it is worth noting that there is only one subgroup of $Pn\bar{3}$ that retains cubic symmetry, $P2_1\bar{3}$, and only one of the possible structures belongs to this group.

The structure of NiSbS has been established (35) by a single crystal x-ray investigation as that shown in Chapter 4 for ullmanite. The structure is the one that retains the cubic symmetry of $P2_1\bar{3}$. A characteristic of this structure is the arrangement of the non-metals in Sb-S pairs which reflects the polar nature of the space group. The structures of the rhodium and iridium compounds have been assumed to be

the same as that of NiSbS on the basis of similarity of x-ray powder diffraction patterns. Whilst the cubic nature of these patterns makes ullmanite seem the most likely structure, it is not impossible that the compounds are only pseudo-cubic and the non-metals are ordered in some other way.

There is a second problem associated with determining the type of ordering, that of the degree of ordering. In order to characterise the sulpho-antimonides used in these Mössbauer investigations it became desirable to know whether the samples were completely ordered and whether RhSbS and IrSbS do in fact have the same structure as NiSbS. An attempt was made to solve these problems crystallographically by collecting x-ray intensity data for the powder samples. The compounds were all reacted at 800°C after which they were ground to pass 100 mesh and annealed for a week at 550°C then slow cooled to room temperature. The main indication of ordering in the x-ray pattern is the presence of the 110 reflection, so if partial ordering is encountered the relative intensity of this reflection should be indicative of the degree of order. If the samples used in this work were only partially ordered it is probable that the degree of disorder would increase with temperature. To investigate this a number of samples were quenched from 600°C, however, no difference in the relative intensity of the 110 reflection could be detected. The observed intensities for NiSbS agreed well with a set of calculated intensities obtained using the atomic positions quoted by Takeuchi (35). Comparison with intensities calculated on the assumption that some degree of disorder existed in the sample lead to the conclusion that ordering

was in fact complete. A comparison of the RhSbS and IrSbS results with intensities calculated using atomic positions similar to those found in NiSbS also gave reasonable agreement, but attempts to refine the structures of all three compounds failed. This failure is certainly a reflection of the number of parameters required to describe these compounds adequately.

Compounds with one positional parameter generally give good results when the structure is refined from powder data (see for example ref. 1).

When Holseth and Kjekshus refined a series of marcasites using two positional parameters and powder data (74) some difficulty was encountered with false minima. It is therefore quite possible that the ullmanite structure, which requires three positional parameters to be refined, is not sufficiently over determined when powder data are used. Added to this is the problem of a polar space group in which the possibility of anomalous dispersion arises. As quite high values for $\Delta f''$ occurred in all three compounds intensities for the reflections hkl and $\bar{h}\bar{k}\bar{l}$ had to be computed independently using complex structure factors and added to give the final intensity. A further complication in this structure which may have contributed to the failure of the refinements is the real possibility of the spherical temperatures being a bad approximation. An examination of the metal site, for example, in Figure 4.2 will show how the grouping of the non-metals makes a near spherical electron distribution unlikely.

In view of the problems outlined above other somewhat more circumstantial evidence must be invoked to characterise the compounds RhSbS and IrSbS. Of all the ternary compounds with an 'ordered pyrite' structure the sulpho-antimonides should probably deviate most from pseudo-

cubic cell parameters if they do not have the ullmanite structure. It is therefore important to note that no splitting or broadening of the high angle x-ray diffraction peaks could be found on careful examination of diffractometer charts. In addition to this the Mössbauer spectra gave e^2Qq values that indicated a structure containing Sb-S pairs.

It is thus not unlikely that RhSbS and IrSbS have the ullmanite structure.

The question of complete order is a somewhat more difficult one as the Mössbauer effect in ^{121}Sb would probably be quite insensitive to a small amount of disorder. If a significant amount of disorder occurred it would manifest itself as Sb-Sb pairs which would be expected to give rise to a second absorption with a somewhat more negative isomer shift and a vastly different quadrupole effect. This would undoubtedly cause a bad fit and possibly show as a shoulder on the Mössbauer peak, neither of these effects was observed.